

# PRG

## Photogrammetrie Fernerkundung Geoinformation

Journal for Photogrammetry, Remote Sensing  
and Geoinformation Science

Organ der Deutschen Gesellschaft für Photogrammetrie,  
Fernerkundung und Geoinformation (DGPF) e. V.

Jahrgang 2015, Heft 2

Hauptschriftleiter:  
Prof. Dr.-Ing. Wolfgang Kresse

Schriftleiter:  
Prof. Dr.-Ing. Stefan Hinz, Prof. Dr. techn. Franz Rottensteiner,  
Prof. Dr. rer.nat. Lars Bernard und Dr.-Ing. Eckhardt Seyfert

**Redaktionsbeirat** (Editorial Board): Clement Atzberger, Andrew Frank,  
Christian Heipke, Joachim Hill, Patrick Hostert, Hans-Gerd Maas, Wolfgang  
Reinhardt, Camillo Ressel, Jochen Schiewe



E. Schweizerbart'sche Verlagsbuchhandlung  
(Nägele u. Obermiller) Stuttgart 2015



Deutsche Gesellschaft für Photogrammetrie, Fernerkundung  
und Geoinformation (DGPF) e.V.  
Gegründet 1909

---

Die *Deutsche Gesellschaft für Photogrammetrie, Fernerkundung und Geoinformation* (DGPF) e.V. unterstützt als Mitglieds- bzw. Trägergesellschaft die folgenden Dachverbände:



International Society  
for Photogrammetry  
and Remote Sensing

**DAGM**

Deutsche Arbeits-  
gemeinschaft für  
Mustererkennung e.V.



---

Herausgeber:

© 2015 Deutsche Gesellschaft für Photogrammetrie, Fernerkundung und Geoinformation (DGPF) e.V.  
Präsident: Prof. Dr. Thomas Kolbe, Technische Universität München, Institut für Geodäsie, GIS und Landmanagement, Lehrstuhl für Geoinformatik, Arcisstraße 21, 80333 München, Germany, Tel. +49-89-289-23888  
Geschäftsstelle: Tanja Nyc, c/o Technische Universität München, Institut für Geodäsie, GIS und Landmanagement, Lehrstuhl für Geoinformatik, Arcisstraße 21, 80333 München, Germany, Tel.: +49-89-289-22578, e-mail: [geschaeftsstelle@dgpf.de](mailto:geschaeftsstelle@dgpf.de)

Published by: E. Schweizerbart'sche Verlagsbuchhandlung (Nägele u. Obermiller), Johannesstraße 3A, 70176 Stuttgart, Germany, Tel.: +49-711 351456-0, Fax: +49-711 351456-99, e-mail: [mail@schweizerbart.de](mailto:mail@schweizerbart.de)  
Internet: <http://www.schweizerbart.de>

⊗ Gedruckt auf alterungsbeständigem Papier nach ISO 9706-1994

All rights reserved including translation into foreign languages. This journal or parts thereof may not be reproduced in any form without permission from the publishers.

Die Wiedergabe von Gebrauchsnamen, Handelsnamen, Warenbezeichnungen usw. in dieser Zeitschrift berechtigt auch ohne besondere Kennzeichnung nicht zu der Annahme, dass solche Namen im Sinne der Warenzeichen- und Markenschutz-Gesetzgebung als frei zu betrachten wären und daher von jedermann benutzt werden dürften.

Verantwortlich für den Inhalt der Beiträge sind die Autoren.

ISSN 1432-8364 / e-ISSN 2363-7145

Science Citation Index Expanded (also known as SciSearch<sup>®</sup>) Journal Citation Reports/Science Edition  
Hauptschriftleiter: Prof. Dr.-Ing. Wolfgang Kresse, Hochschule Neubrandenburg, Fachbereich Landschaftswissenschaften und Geomatik, Brodaer Straße 2, 17033 Neubrandenburg, Germany, e-mail: [kresse@hs-nb.de](mailto:kresse@hs-nb.de)  
Schriftleiter: Prof. Dr.-Ing. Stefan Hinz, Karlsruher Institut für Technologie – KIT, Institut für Photogrammetrie und Fernerkundung, Englerstraße 7, 76131 Karlsruhe, Germany, e-mail: [stefan.hinz@ipf.uni-karlsruhe.de](mailto:stefan.hinz@ipf.uni-karlsruhe.de), Prof. Dr. techn. Franz Rottensteiner, Leibniz Universität Hannover, Institut für Photogrammetrie und GeoInformation, Nienburger Straße 1, 30167 Hannover, Germany, e-mail: [rottensteiner@ipi.uni-hannover.de](mailto:rottensteiner@ipi.uni-hannover.de), Prof. Dr. rer. nat. Lars Bernard, Technische Universität Dresden, Fachrichtung Geowissenschaften, Helmholtzstraße 10, 01062 Dresden, Germany, e-mail: [lars.bernard@tu-dresden.de](mailto:lars.bernard@tu-dresden.de), und Dr.-Ing. Eckhardt Seyfert, Landesvermessung und Geobasisinformation Brandenburg, Heinrich-Mann-Allee 103, 14473 Potsdam, Germany, e-mail: [eckhardt.seyfert@geobasis-bb.de](mailto:eckhardt.seyfert@geobasis-bb.de)

Erscheinungsweise: 6 Hefte pro Jahrgang.

Bezugspreis im Abonnement: € 249,- pro Jahrgang. Mitglieder der DGPF erhalten die Zeitschrift kostenlos. Der Online-Zugang ist im regulären Subskriptionspreis enthalten.

Anzeigenverwaltung: E. Schweizerbart'sche Verlagsbuchhandlung (Nägele u. Obermiller), Johannesstraße 3A, 70176 Stuttgart, Germany, Tel.: +49-711 351456-0; Fax: +49-711 351456-99.

e-mail: [mail@schweizerbart.de](mailto:mail@schweizerbart.de), Internet: <http://www.schweizerbart.de>

Bernhard Harzer Verlag GmbH, Westmarkstraße 59/59a, 76227 Karlsruhe, Germany, Tel.: +49-721 944020, Fax: +49-721 9440230, e-mail: [Info@harzer.de](mailto:Info@harzer.de), Internet: [www.harzer.de](http://www.harzer.de)

Printed in Germany by Tutte Druckerei & Verlagsservice GmbH, 94121 Salzweg, Germany.

## PFG – Jahrgang 2015, Heft 2 Inhaltsverzeichnis

---

### Originalbeiträge

ELSTE, S., GLÄSSER, C., WALTHER, I. & GÖTZE, C.: Multi-temporal Analysis of RapidEye Data to Detect Natural Vegetation Phenology During Two Growing Seasons in the Northern Negev, Israel. . . . .	117
THONFELD, F., HECHELTJEN, A. & MENZ, G.: Bi-temporal Change Detection, Change Trajectories and Time Series Analysis for Forest Monitoring . . . . .	129

---

### Beiträge aus Wissenschaft und Praxis

BAKUŁA, K., DOMINIK, W. & OSTROWSKI, W.: Enhancement of Lidar Planimetric Accuracy using Orthoimages . . . . .	143
GOLOVKO, D., ROESSNER, S., BEHLING, R., WETZEL, H.-U. & KLEINSCHMIT, B.: Development of Multi-Temporal Landslide Inventory Information System for Southern Kyrgyzstan Using GIS and Satellite Remote Sensing . . . . .	157
ZHAO, Q., HÜTT, C., LENZ-WIEDEMANN, V.I.S., MIAO, Y., YUAN, F., ZHANG, F. & BARETH, G.: Georeferencing Multi-Source Geospatial Data using Multi-Temporal TerraSAR-X Imagery: a Case Study in Qixing Farm, Northeast China. . . . .	173

---

### Mitteilungen

#### Berichte von Veranstaltungen

Symposium der ISPRS Commission III, 5.–7. September 2014, Zürich, Schweiz . . . . .	187
14th RACURS Photogrammetric Conference, 19.–23. October 2014, Hainan, China . . . . .	189
Symposium der ISPRS Commission I, 17.–20. November 2014, Denver, USA . . . . .	190
<b>Persönliches</b>	
Nachruf auf GERHARD NEUKUM . . . . .	192
Veranstaltungskalender . . . . .	193
Korporative Mitglieder . . . . .	195

Zusammenfassungen der „Originalbeiträge“ und der „Beiträge aus Wissenschaft und Praxis“ (deutsch und englisch) sind auch verfügbar unter [www.dgpf.de/neu/pfg/ausgaben.htm](http://www.dgpf.de/neu/pfg/ausgaben.htm)





# Multi-temporal Analysis of RapidEye Data to Detect Natural Vegetation Phenology During Two Growing Seasons in the Northern Negev, Israel

STEFANIE ELSTE, CORNELIA GLÄSSER, IVO WALTHER & CHRISTIAN GÖTZE, Halle (Saale)

**Keywords:** RapidEye, phenology, natural vegetation, semi-arid, multi-temporal analysis

**Summary:** This study focused on the analysis of semi-arid natural vegetation phenology in the Northern Negev in Israel during the two growing seasons in 2010/2011 and 2012/2013 with different precipitation patterns. The objective was to develop a methodology based on vegetation indices to detect the characteristic phenological cycles of three types of vegetation, annual grasses, perennial shrubs and biological soil crusts, with multi-temporal RapidEye data. For the first time the usage of RapidEye's high temporal resolution as well as its red edge band enabled a detailed detection of this phenology in semi-arid environments. In doing so, the vegetation indices differed in their suitability for the different vegetation types. One could benefit from the Normalized Difference Vegetation Index (NDVI) for annual plants, the Normalized Difference Red Edge Index (NDRE) for perennial plants and the Modified Normalized Difference Vegetation Index (MNDVI) for biological soil crusts. The spatial distribution of the vegetation is illustrated by combining the three indices during their maximal photosynthetic activity.

**Zusammenfassung:** *Multitemporale Analyse von RapidEye-Daten zur Untersuchung der phänologischen Entwicklung natürlicher Vegetation zweier Vegetationsperioden in der nördlichen Negev, Israel.* In vorliegender Studie wurde die phänologische Entwicklung semiarider, natürlicher Vegetation im Norden der Wüste Negev während zwei Vegetationsperioden mit sehr unterschiedlichen Niederschlagsverhältnissen anhand von RapidEye-Daten untersucht. Ziel ist die Entwicklung einer Methode auf der Basis von Vegetationsindizes wie dem NDVI, welche die charakteristischen phänologischen Zyklen der Vegetation ermittelt: einjährige Gräser, mehrjährige Büsche sowie biologische Krusten. Die hohe temporale Auflösung der RapidEye-Daten sowie der RedEdge Kanal ermöglichten zum ersten Mal eine detaillierte Erfassung der Phänologie in diesem Gebiet. Die Indizes eignen sich dabei für die Vegetationstypen unterschiedlich gut. So konnten für mehrjährige Pflanzen der NDRE sowie der MNDVI für biologische Krusten Informationsgewinne liefern. Die räumliche Verbreitung der Vegetation wird durch die Kombination jener Indizes, die die maximale photosynthetische Aktivität der Vegetationstypen widerspiegeln, dargestellt.

## 1 Introduction

The characteristic feature of arid and semi-arid ecosystems is their high temporal and spatial variability regarding precipitation (BLÜMEL 2013). Therefore, they are very vulnerable to additional climate extremes in terms of climate change (SCHLESINGER et al. 1990). Hence it is important to monitor this vegetation in relation to climate to notice changes in their development for the management and protection

of these ecosystems. Phenology has proven to be a very suitable tool for this because it comprises “the study of the timing of recurring biological events, the causes of their timing with regard to biotic and abiotic forces, and the interrelation among phases of the same or different species” (LIETH 1974). Due to the spatial coverage as well as financial and time related savings, remote sensing techniques proved to be very suitable for these kinds of analyses. For example until now especially dense

time series of NOAA AVHRR data were used in semi-arid environments like the Northern Negev because of its very high temporal resolution (SCHMIDT & KARNIELI 2000, WANG & TENHUNEN 2004). Contrarily, Landsat data would provide more spatial details due to its better spatial resolution but is limited concerning phenological analyses in very sensitive ecosystems in arid regions because of its coarser temporal resolution (ELMORE et al. 2000). Consequently, a combination of high temporal and spatial resolution data is needed to detect important phenological events as well as changes in the spatial distribution of vegetation especially in heterogeneous landscapes like the Northern Negev. With the development of multi-sensor satellite systems such as RapidEye, the temporal resolution of high spatial resolution optical sensors has increased remarkably. Therefore, multi-temporal RapidEye data has been successfully applied to classify vegetation units or different plant parameter (SCHUSTER et al. 2012).

The Northern Negev is characterized by sparse natural vegetation cover that consists of annual grasses, perennial shrubs and biological soil crusts (KARNIELI 2003). KARNIELI (2003) described that each of these vegetation types exhibit their own typical phenology in relation to precipitation (Fig. 1). In the following these different phenologies are referred to as phenological cycles. In contrast to shrubs and grasses, biological soil crusts consist of cyanobacteria, algae, mosses, fungi and lichens (DANIN 1996). These microphytes are typically representative in arid and semi-arid

id areas (DANIN 1996). Dry conditions force these organisms into a latent state; only when they have some water they become physiologically active and turn green due to their photosynthetic activity (DANIN 1996). Because of this very sensitive response to moisture, KARNIELI (2003) found that they are the first to become physiologically active at the beginning of the growing season when the first rainfall occurred (Fig. 1). At this point annuals and perennials are still dormant, because water is only available at the soil surface. The seeds of annual vegetation in the deeper soil layers require water to germinate, so they will not become active until more precipitation is available, which occurs in the middle of the rainy season. After the annuals fulfilled their development and become dry organic matter, perennial plants start to become active at the end of the growing season, when water is available for their deeper roots.

From the remote sensing point of view it is very difficult to discriminate photosynthetically active biological soil crusts from vital grasses and shrubs because their spectral signatures resemble each other (WEBER et al. 2008). KARNIELI et al. (1999) discovered that phycobilin pigments in the crusts cause a stronger reflection in the blue region of the electromagnetic spectrum which facilitates the discrimination. When dry, their spectral signature resembles soil (KARNIELI et al. 1999).

The objective of this study was to develop a methodology to detect this characteristic natural vegetation phenology based on vegetation indices due to the different spectral characteristics of the vegetation types. Time series of RapidEye datasets with a high temporal resolution were analyzed for two seasons. 2010/2011 was a relatively dry season and 2012/2013 reached nearly the annual average for the study area. The comparison of the phenology of these seasons should reveal the sensitive reaction of the vegetation to different precipitation patterns.

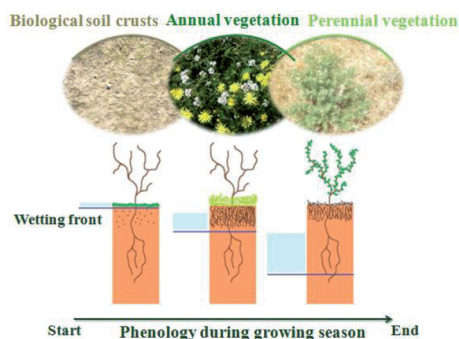


**Fig. 1:** Phenology of different vegetation types during the growing season in the Negev, Israel (after KARNIELI 2003).

## 2 Study Area

Sayaret Shaked Park, a heterogeneous landscape formed by loessial soils, is an area of one km<sup>2</sup> located in the Northern Negev

with center coordinates of 31°16'11" N and 34°39'10" E in Israel. The annual mean precipitation is 200 mm and mainly concentrates between November and April and constitutes semi-arid climatic conditions (KARNIELI et al. 2002). During this rainy period, later referred to as growing season, vegetation get photosynthetically active due to better moisture conditions (CLIMATE SERVICE CENTER 2.0 2014). The climatic and topographic conditions lead to a heterogeneous mosaic of perennial shrubs (e.g. *Noaea mucronata*, *Thymelea hirsute*), annual grasses (e.g. *Stipa capensis*, *Avena barbata*) and biological soil crusts which consist mostly of cyanobacteria (BURGHEIMER et al. 2006). While shrubs and grasses settle predominantly on sinks and slopes, the crusts cover the whole soil surface (BURGHEIMER et al. 2006), which leads to a lot of transition zones. One part of the park is closed off to livestock grazing since 1987 (KARNIELI et al. 2002) and represents a research area of the Long Term Ecological Research Programme (LTER) and the Experimentation in Ecosystem Research Programme (ExpeER). Therefore, it is possible to study the natural vegetation in a small undisturbed ecosystem. Nevertheless, very dry consecutive years led to the death of numerous perennial shrubs recently, which partly destabilizes the ecosystem (SHER et al. 2012).

### 3 Data and Methodology

To cope with the sparseness and heterogeneity of the vegetation cover in Shaked Park, RapidEye data was chosen for the multi-temporal analysis because it combines high temporal with high spatial resolution. The five identical earth observation satellites located in a sun-synchronous orbit in approx. 630 km height record information in five multispectral bands with a temporal resolution of 1 to 5.5 days and a spatial resolution of 6.5 m (BLACKBRIDGE 2013). Designed predominantly for agriculture and forestry, RapidEye provides additional information for vegetation applications by the red edge channel from 690 nm – 730 nm (BLACKBRIDGE 2013) (Tab. 1).

To characterize the seasonal phenology of the three vegetation types, temporal dense

**Tab. 1:** Spectral band widths of the RapidEye sensor.

Multispectral bands	Band widths
Blue	440 nm – 510 nm
Green	520 nm – 590 nm
Red	630 nm – 685 nm
Red Edge	690 nm – 730 nm
NIR	760 nm – 850 nm

time series of RapidEye data were required. Hence, images were ordered every 10 days, but due to meteorological and technical conditions the scenes were sometimes limited. Finally, as shown in Fig. 2, for the season 2010/2011 nine and for 2012/2013 thirteen cloud-free images were used.

Preprocessing of the data included orthorectification of Level 1B data and an atmospheric correction with ATCOR<sup>®</sup> 2 of every image (RICHTER & SCHLÄPFER 2012). Furthermore, the geometric correction of the data was improved by additional co-registration because the spatial location of the scenes was partly inaccurate. This is caused by the small number of ground control points which varies from region to region and influences the spatial accuracy (BLACKBRIDGE 2013). In addition to the satellite images, daily precipitation data for the two seasons was available from the Ben-Gurion University weather station. During a field campaign in spring 2013 different kinds of reference data were gathered from various test sites, which were selected separately for areas with predominantly coverage of annual grasses, perennial bushes and biological soil crusts. The data contained photos of vegetation coverage during the growing season, field mapping for the vegetation index (VI) analysis and GPS data, which served as reference pixel for each type of vegetation.

Due to their simple and robust application, vegetation indices, which proved to be very suitable for remote sensing of vegetation, were chosen for the multi-temporal analysis (CHU-

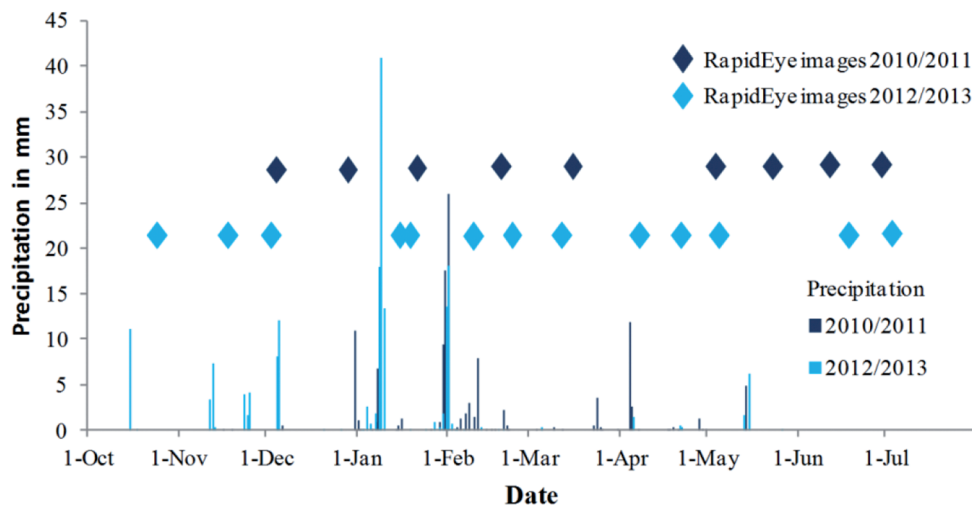


Fig. 2: Acquisition dates of RapidEye data in relation to precipitation.

VIECO & HUETE 2010). The NDVI (1) (ROUSE et al. 1974) was selected as the basic VI since up to now it is proved as suitable tool for vegetation analysis in numerous studies (PETTORELLI 2013). To test whether the red edge band provides additional information for this study, the NDRE was used (2), where the NIR band of the NDVI formula is replaced by the red edge band (BARNES et al. 2000). The red edge spectral region is also very sensitive for mapping stressed vegetation (EITEL et al. 2011). Furthermore, the specific spectral features of biological soil crusts lead to the application of the MNDVI (3), where the blue band is integrated in the original NDVI formula (SIMS & GAMON 2002).

$$NDVI = \frac{NIR - RED}{NIR + RED} \quad (1)$$

$$NDRE = \frac{Red\ Edge - RED}{Red\ Edge + RED} \quad (2)$$

$$MNDVI = \frac{NIR - RED}{NIR + RED - 2BLUE} \quad (3)$$

After preprocessing, each VI was calculated for every reference pixel of the test sites. For each vegetation type the values of the ref-

erence pixels were averaged and visualized as VI curves and analyzed in relation to precipitation. These temporal profiles proved to be a very useful tool in phenological research with remote sensing data (FÖRSTER et al. 2012, RASMUSSEN 1997, ODENWELLER & JOHNSON 1984, JUSTICE et al. 1985). Knowledge-based, accordingly to Fig. 1, the slopes and local maxima – as indicators of photosynthetic activity – in the graphs were assigned to the phenological cycles of the vegetation types. During this process it was investigated which VI shows the best result to characterize the phenology of each vegetation type. Finally, the index images with the maximal photosynthetic activity for each type of vegetation were chosen and combined in a false colour composite to illustrate their spatial distribution.

## 4 Results

This section shows the results of the multi-temporal analyses. We determined the typical phenological cycles for the two growing seasons 2010/2011 and 2012/2013 with multi-temporal remote sensing data as a function of time and precipitation. A dotted line between each index value shall help to interpret the graphs in Figs. 3 and 4.

#### 4.1 Vegetation Period 2010/2011

Multi-temporal index profiles for the growing season 2010/2011 are illustrated in Fig. 3. Based on our research it is observed that crusts got photosynthetically active relatively late, because significant rainfall did not occur until the end of December. Therefore, the growing season started in late December and ended in July. The NDVI of annual plants stayed constant from December until the middle of January although considerably rainfall occurred during December and the beginning of January. Subsequently it increases rapidly to its peak from February until March because the red portion of the electromagnetic spectrum declines and the NIR increases due to the photosynthetic activity. Afterwards, the NDVI declines to the level at the beginning in May and June as a result of reduction of photosynthetic activity which leads to a relatively stronger reflectance in the red spectral region. Based on the explanations to Fig. 1 a peak of photosynthetic activity in the middle of the growing season suggests the phenological cycle of annual vegetation.

At the beginning of the growing season the MNDVI shows a different behaviour in comparison to the NDVI of the annuals, because it increases to the middle of January when the NDVI stood constant. This is an important indication of the photosynthetic activity of the crusts, because the RapidEye image

of the 19<sup>th</sup> January was acquired briefly after rainfall occurred (Fig. 2). Consequently, this scene is very suitable to discriminate the phenological cycle of the crusts from the annual vegetation phenological cycle which starts about one month later than the cycle of the soil crusts. Since this increase cannot be found in the NDVI curve, it indicates a benefit of the additional blue spectral band of the MNDVI to detect the physiological activity of the soil crusts. After this increase it also reaches its maximum in March and declines until May, similar to the NDVI of the annuals. This supports the assumption of the peak of the phenological cycle of the annuals during March 2011, because annuals appear on these sites too and cover the spectral signal of the crusts due to their more intensive coverage at this time.

Noticeably there is no further increase of these two indices at the end of the growing season and therefore no sign of the activity of perennial plants. In contrast to that, there is a slight increase in the curve of the NDRE for areas with predominantly perennial vegetation cover from the beginning until the middle of May with a clearer decrease at the end of July. Unfortunately there is no RapidEye image in June which could confirm this assumption. Even though this is just a slight indication of the phenological cycle of the perennials it is an important sign of their activity in regards to this very dry year and the plant's

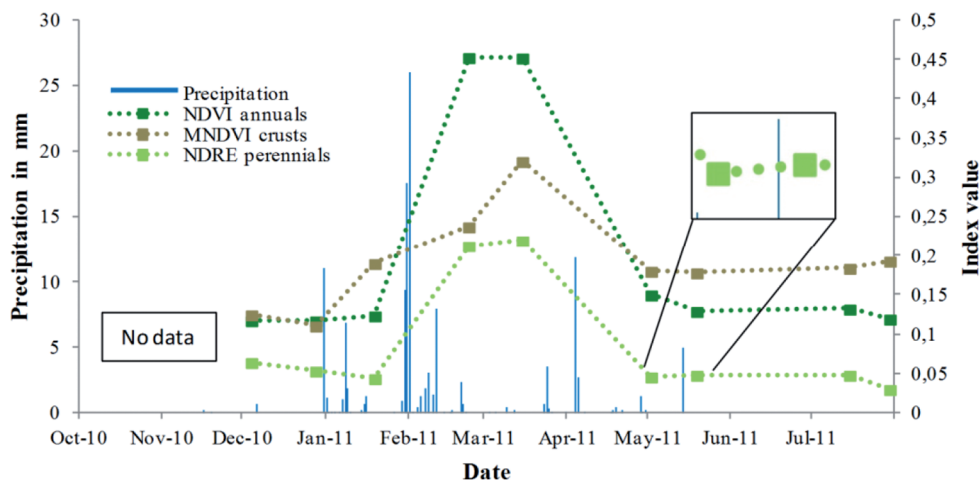


Fig. 3: Multi-temporal index profiles of the growing season 2010/2011.

partly critical health status due to the drought from 2008 until 2010 (SHER et al. 2012). Furthermore, the fact that only the NDRE shows the indication of this cycle it can be reasoned that the red edge channel contributes to an improved detection of their photosynthetic activity in Shaked Park.

In summary the phenological cycles for biological soil crusts and annuals of the growing season 2010/2011 could be detected completely with the datasets. The phenological cycle of the annuals from the middle of January until May with a peak from February until March could be determined completely while the crust cycle started at the end of December, due to the precipitation, with a peak in the middle of January. Contrarily to the annuals, a clear end of the cycle of crusts could not be determined because the MNDVI does not decline before the annuals started to germinate. The start and end of the phenological cycle of the perennials was more complicated to determine because their scarce distribution and critical health status led to a very low signal of photosynthetic activity in this very dry year.

#### 4.2 Vegetation Period 2012/2013

The phenological cycles for natural vegetation during the growing season 2012/2013 differ in the timing as well as in the duration of the

cycles and the growing season in general in comparison to 2010/2011. Accordingly to the previous period, the multi-temporal profiles of the three VI are illustrated in relation to precipitation in Fig. 4. As consequence of the different precipitation pattern the vegetation types are active from November until May. In this figure relatively similar courses of the index profiles with slight differences can be recognized.

As seen in the previous season 2010/2011, the different behaviour of the NDVI of the annuals and the MNDVI of the crusts at the beginning of the growing season is repeating but occurs earlier. The NDVI stays constant from the middle of October until the middle of November although significant rainfall occurred just two days before the RapidEye image in November was recorded. In the meantime the MNDVI of the crusts increases due to the sensitive reaction of these organisms to moisture. Again the combined analysis of these two indices proved to be suitable to discriminate the beginning of the phenological cycle of the biological soil crusts from the annual grasses. The MNDVI further increases from that point until the 17<sup>th</sup> January. Three days after this RapidEye image was taken, the MNDVI declines due to the missing precipitation which leads to a decline of the photosynthetic activity of the crusts. This would not be the case if the annuals were already active so that this

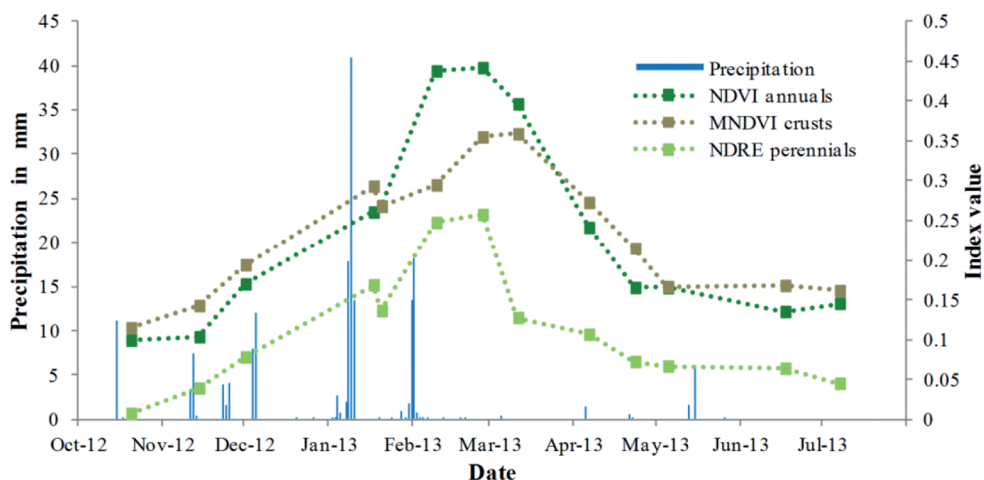


Fig. 4: Multi-temporal index profiles of the growing season 2012/2013.

point of time represents the end of the phenological cycle of the crusts. After this decline the MNDVI reaches its peak in March before it declines until May due to the photosynthetic activity of the annuals which superimpose the signal of the crusts because of their dense coverage at this point of time.

In contrast to that, the NDVI of the annuals starts to increase continuously from the middle of November to February where it reaches its maximum until March before it declines at the end of April almost to the base level. Consequently, it does not decline in January like the MNDVI. This is a clear sign of the photosynthetic activity of the annuals at that time. However, it is not definitely clear when the phenological cycle of the annuals starts because the NDVI increases already from the beginning of the growing season 2010/2011 which is unusual for these plants. A potential

explanation for that is the early beginning of the precipitation season that leads to a stronger signal of the photosynthetic activity of the biological soil crusts which superimposed that of the annuals so that the NDVI increases at that early stage of this season.

Similar to the previous season (2010/2011) the phenological cycle of perennial vegetation cannot be extracted from the multi-temporal profiles of the NDVI and MNDVI but is shown more clearly in the NDRE profile. At the end of the growing season the NDRE falls not directly after the decline since the peak of the annuals in March. From the end of March until the beginning of April it stays almost constant before it declines until May which is again an indication of the activity of perennial plants.

All in all the existent RapidEye images allowed the complete detection of the pheno-

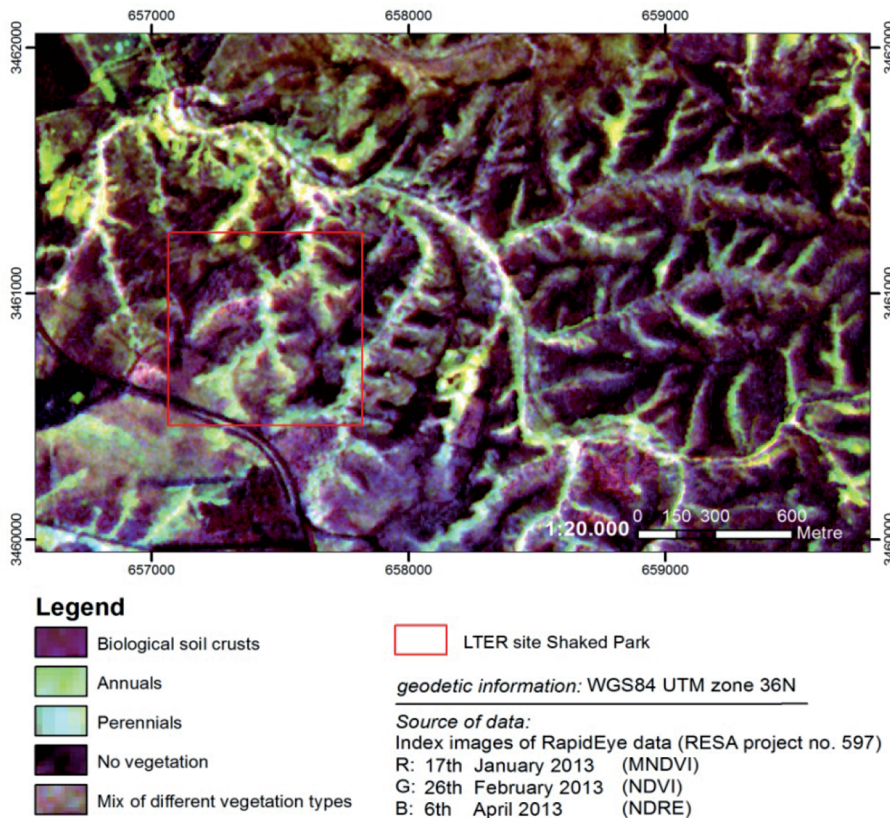


**Fig. 5:** False colour composite of index images of RapidEye data which show the maximal photosynthetic activity of each vegetation type in Shaked Park.

logical cycle of the crusts which lasts from November until January except of their maximum because no RapidEye images were available in December. The peak and end of the cycle of the annuals could be determined, too. In contrast to that, uncertainty exists for its beginning. The perennials were active from March until April.

For the season 2012/2013, the spatial distribution of natural vegetation in Shaked Park is illustrated with a false colour composite (Fig. 5). For this composite the three indices which show the maximal photosynthetic activity of the different vegetation types were combined. The red channel represents the MNDVI for crusts at the middle of January, the green represents the NDVI for annuals at the end of February and the blue represents the NDRE for perennials at the beginning of April (Fig. 5). Because there are predominantly areas with different portions of annuals, perennials and crusts, the colours in this image represent a mixture of red, green and blue. Obviously, annuals (green colours) and perennials (cyan-green colours) concentrate on sinks and slopes due to the better water availability. In contrast, biological soil crusts (dark purple-brown colours) are broadly distributed in the park due to their excellent adaptation to semi-arid conditions.

## 5 Discussion

For the first time the typical natural vegetation phenology in the Northern Negev could be detected by high resolution RapidEye datasets. RapidEye images proved to be very suitable for the multi-temporal analysis because its high temporal resolution was helpful to determine the phenological cycles in detail. A robust methodology based on a combination of different vegetation indices could be developed which was applied successfully to two seasons with different precipitation patterns. The results correspond very well with those of other studies of this region (KARNIELI 2003, KARNIELI et al. 2002) and could be verified by field data.

Nevertheless, the results depend strongly on the availability of satellite data. So missing scenes in time periods of one month in

June 2011 and December 2012 led to incomplete phenological cycles without maxima. Also every other index feature just shows the photosynthetic activity of the vegetation types at a specific point of time. For example, the start of the phenological cycle of the biological soil crusts in November 2012 cannot be fixed to that point because significant rainfall events were recorded in the middle of October which would cause the crusts to become active. So probably the MNDVI would be lower than in the end of October, but there was no scene available that was acquired earlier. Consequently, the time lag between rainfall events and the acquisition dates of the satellite images are also essential to describe the phenological cycles in detail especially for the sensitive reaction to moisture of the biological soil crusts.

The comparison of temporal profiles of the different vegetation indices demonstrated the NDVI as the most suitable index for detecting the phenological cycle of annual vegetation because it presented the maximum photosynthetic activity most clearly. Every investigated VI, i.e. NDRE, MNDVI, and NDVI, shows this maximum because all computation methods are an enhancement of the NDVI. Furthermore the MNDVI proved to be most suitable to determine the physiological activity of the biological soil crusts because it experienced the fastest reaction to precipitation at the beginning of the growing season. This is probably due to the phycobilin pigments whose stronger reflection in the blue spectral region could be registered much better by incorporating the blue band. The phenological cycle of perennial vegetation could only be detected by using the NDRE which confirms the generation of additional information through the red edge band. Other studies which evaluated the benefit of the red edge channel discovered an improvement of classification accuracies by using the NDRE, too (SCHUSTER et al. 2012). SCHUSTER et al. (2012) stated the higher sensitivity of the red edge band for vegetation adapted to dry climate conditions. One reason could also be the higher sensitivity of this spectral region for stressed vegetation, which could also be confirmed with RapidEye data for woody vegetation (EITEL et al. 2011). All in all one single index could not always

represent the whole natural vegetation phenology. In this study the NDRE in 2012/2013 was the only situation where this VI shows all phenological cycles together. Probably high precipitation during this season led to a strong growth of the plants and therefore a strong spectral signal, but to be sure further analyses are required. Hence a combined analysis with the three proposed VI is recommended.

Furthermore, the sensitive reaction of the natural vegetation to different precipitation patterns could be revealed by comparing the timing and duration of the cycles for each season. The variations of the durations of the cycles were less compared to variations in timing. Due to the earlier onset of precipitation in the growing season 2012/2013, the phenological cycles in this season started about one month prior to the average. For instance, the cycle of biological soil crusts started in the 2012/2013 season in the middle of November, while in the previous season the start was dated in the middle of January 2011. In general, the complete phenological development pattern is shifted to earlier dates by one month. This clearly demonstrates the good adaption of desert plants to the highly temporal variable moisture conditions.

## 6 Conclusion and Outlook

For the first time high resolution RapidEye images allowed a detailed multi-temporal analysis concerning phenological events in a semi-arid region in Israel with high variability in precipitation. To detect the characteristic natural vegetation phenology a robust methodology based on a combination of the vegetation indices NDVI, MNDVI and NDRE was developed, which can be applied independently to the distribution and quantity of precipitation. Each of these three indices turned out to be suitable for one particular type of vegetation: the MNDVI for biological soil crusts, the NDVI for annual grasses and the NDRE for perennial vegetation. Furthermore, the methodology allows analyses of the spatial distribution of this natural vegetation by combining the index images of the scene of the respective maximal activity of each component in a false colour composite. The comparison of two

growing seasons showed the shifting of phenological events due to the different precipitation patterns which emphasizes their role as important indicators of climate change and ecosystem stability in a very vulnerable semi-arid environment. RapidEye datasets proved to be very suitable for the multi-temporal analysis of phenological analyses in semi-arid environments especially with regards to its high temporal resolution and the gain of additional information with the NDRE provided by the red edge band. The time-series allowed the detection of natural vegetation phenology after the scheme of (Fig. 1) in both seasons, but uncertainties exist for perennial shrubs due to their scattered distribution and critical health status. Also the transition between the start and end of the phenological cycles is highly variable because of their spatial overlap. Future work will aim on the adaption of the approach to other sensors like WorldView-2 with a better spatial resolution of 2 m which can improve the detection of the perennial shrubs.

## Acknowledgements

We thank the DLR for providing data from the RapidEye Science Archive (RESA project no. 597). Financial support by the Transnational Access to Research Infrastructures activity in the 7<sup>th</sup> Framework Programme of the EC under the ExpeER project for conducting the research is gratefully acknowledged. We also want to thank Prof. ARNON KARNIELI, ALEXANDER GOLDBERG and NATALIA PANOV of the Remote Sensing Laboratory of the Ben-Gurion University of the Negev for the very good cooperation. Furthermore we are grateful for the support of a research stay in Israel in the framework of the PROMOS programme of the DAAD.

## References

- BARNES, E.M., CLARKE, T.R., RICHARDS, S.E., COLLAZZI, P.D., HABERLAND, J., KOSTRZEWSKI, M., WALLER, P., CHOI, C., RILEY, E., THOMPSON, T., LASCANO, R.J., LI, H. & MORAN, M.S., 2000: Coincident detection of crop water stress, nitrogen status and canopy density using ground-based multispectral data. – ROBERT, P.C., RUST, R.H. &

- LARSON, W.E. (eds.): Fifth International Conference on Precision Agriculture: 1–15, Bloomington, IL, USA.
- BLACKBRIDGE, 2013: Satellite Imagery Product Specifications. – [http://www.blackbridge.com/rapideye/upload/RE\\_Product\\_Specifications\\_ENG.pdf](http://www.blackbridge.com/rapideye/upload/RE_Product_Specifications_ENG.pdf) (3.2.2014).
- BLÜMEL, W.D., 2013: Wüsten – Entstehung, Kennzeichen, Lebensraum. – First Edition, 327 p., Ulmer, Stuttgart.
- BURGHEIMER, J., WILSKE, B., MASEYK, K., KARNIELI, A., ZAADY, E., YAKIR, D. & KESSELMEIER, J., 2006: Ground and space spectral measurements for assessing the semi-arid ecosystem phenology related to CO<sub>2</sub> fluxes of biological soil crusts. – *Remote Sensing of Environment* **101** (1): 1–12.
- CHUVIECO, E. & HUETE, A., 2010: Fundamentals of Satellite Remote Sensing. – 436 p., CRC Press, Boca Raton, FL, USA.
- CLIMATE SERVICE CENTER 2.0, 2014: [http://www.climate-service-center.de/033626/index\\_0033626.html.de](http://www.climate-service-center.de/033626/index_0033626.html.de) (17.12.2014).
- DANIN, A., 1996: Plants of desert dunes. – Adaptation of desert organisms, 177 p., Springer, Berlin.
- EITEL, J.U.H., VIERLING, L.A., LITVAK, M.E., LONG, D.S., SCHULTHESS, U., AGER, A.A., KROFCHICK, D.J. & STOSCHECK, L., 2011: Broadband, red-edge information from satellites improves early stress detection in a New Mexico conifer woodland. – *Remote Sensing of Environment* **115** (12): 3640–3646.
- ELMORE, A.J., MUSTARD, J.F., MANNING, S.J. & LOBELLE, D.B., 2000: Quantifying Vegetation Change in Semiarid Environments: Precision and Accuracy of Spectral Mixture Analysis and the Normalized Difference Vegetation Index. – *Remote Sensing of Environment* **73** (1): 87–102.
- FÖRSTER, S., KADEN, K., FÖRSTER, M. & ITZEROTT, S., 2012: Crop type mapping using spectral-temporal profiles and phenological information. – *Computers and Electronics in Agriculture* **89**: 30–40.
- JUSTICE, C.O., TOWNSHEND, J.R.G., HOLBEN, B.N. & TUCKER, C.J., 1985: Analysis of the phenology of global vegetation using meteorological satellite data. – *International Journal of Remote Sensing* **6** (8): 1271–1318.
- KARNIELI, A., KIDRON, G.J., GLÄSSER, C. & BENDOR, E., 1999: Spectral Characteristics of Cyanobacteria Soil Crust in Semiarid Environments. – *Remote Sensing of Environment* **69** (1): 67–75.
- KARNIELI, A., GABAI, A., ICHOKU, C., ZAADY, E. & SHACHAK, M., 2002: Temporal dynamics of soil and vegetation spectral responses in a semi-arid environment. – *International Journal of Remote Sensing* **23** (19): 4073–4087.
- KARNIELI, A., 2003: Natural vegetation phenology assessment by ground spectral measurements in two semi-arid environments. – *International Journal of Biometeorology* **47** (4): 179–187.
- LIETH, H., 1974: Phenology and seasonality modeling. – *Ecological Studies* **8**, Springer, New York, NY, USA.
- ODENWELLER, J.B. & JOHNSON, K.I., 1984: Crop Identification Using Landsat Temporal-Spectral Profiles. – *Remote Sensing of Environment* **14** (1–3): 39–54.
- PETTORELLI, N., 2013: The Normalized Difference Vegetation Index. – First Edition, 208 p., Oxford University Press, New York, NY, USA.
- RASMUSSEN, M.S., 1997: Operational yield forecast using AVHRR NDVI data: Reduction of environmental and inter-annual variability. – *International Journal of Remote Sensing* **18** (5): 1059–1077.
- RICHTER, R. & SCHLÄPFER, D., 2012: Atmospheric/Topographic Correction for Satellite Imagery (ATCOR-2/3 User Guide). – [http://www.dlr.de/eoc/Portaldata/60/Resources/dokumente/5\\_tech\\_mod/atcor3\\_manual\\_2012.pdf](http://www.dlr.de/eoc/Portaldata/60/Resources/dokumente/5_tech_mod/atcor3_manual_2012.pdf) (13.5.2014).
- ROUSE, J.W., HAAS, R.H., SCHELL, J.A., DEERING, D.W. & HARLAN, J.C., 1974: Monitoring the vernal advancement and retrogradation (green-wave effect) of natural vegetation. – NASA/GFSC Type III, Final Report, Greenbelt, MD, USA.
- SCHLESINGER, W.H., REYNOLDS, J.F., CUNNINGHAM, G.L., HUENNEKE, L.F., JARRELL, W.M., VIRGINIA, R.A. & WHITFORD, W.G., 1990: Biological Feedbacks in Global Desertification. – *Science* **247** (4946): 1043–1048.
- SCHMIDT, H. & KARNIELI, A., 2000: Remote Sensing of the seasonal variability of vegetation in a semi-arid environment. – *Journal of Arid Environments* **45**: 43–59.
- SCHUSTER, C., FÖRSTER, M. & KLEINSCHMIT, B., 2012: Testing the red edge channel for improving land-use classifications based on high-resolution multi-spectral satellite data. – *International Journal of Remote Sensing* **33** (17): 5583–5599.
- SHER, Y., ZAADY, E., ROONEN, Z. & NEJIDAT, A., 2012: Nitrification activity and levels of inorganic nitrogen in soils of a semi-arid ecosystem following a drought-induced shrub death. – *European Journal of Soil Biology* **53**: 86–93.
- SIMS, D.A. & GAMON, J.A., 2002: Relationships between leaf pigment content and spectral reflectance across a wide range of species, leaf structures and developmental stages. – *Remote Sensing of Environment* **81** (2–3): 337–354.
- WANG, Q. & TENHUNEN, J.D., 2004: Vegetation mapping with multitemporal NDVI in North Eastern China Transect (NECT). – *International Journal*

of Applied Earth Observation and Geoinformation **6** (1): 17–31.

WEBER, B., OLEHOWSKI, C., KNERR, T., HILL, J., DEUSCHEWITZ, K., WESSELS, D.C.J., EITEL, B. & BÜDEL, B., 2008: A new approach for mapping of Biological Soil Crusts in semi-desert areas with hyperspectral imagery. – Remote Sensing of Environment **112** (5): 2187–2201.

Address of the Authors:

STEFANIE ELSTE, B.Sc., Prof. Dr. CORNELIA GLÄSSER, IVO WALTHER, B.Sc. & Dr. CHRISTIAN GÖTZE, Martin-Luther-University Halle-Wittenberg, Institute of Geosciences and Geography, Department of Remote Sensing and Cartography, Von-Seckendorff-Platz 4, D-06120 Halle (Saale), Tel.: +49-0345-55-26020, e-mail: stefanie.elste@student.uni-halle.de, cornelia.glaesser@geo.uni-halle.de, ivo.walther@student.uni-halle.de, christian.goetze@geo.uni-halle.de.

Manuskript eingereicht: Juni 2014

Angenommen: Dezember 2014





# Bi-temporal Change Detection, Change Trajectories and Time Series Analysis for Forest Monitoring

FRANK THONFELD, ANTJE HECHELTJEN & GUNTER MENZ, Bonn

**Keywords:** land cover change, change detection, time series analysis, forest monitoring

**Summary:** Traditional change detection refers to bi-temporal approaches. With the recent open access policy of several data providers, the use of multi- to hyper-temporal data for change detection and monitoring applications becomes feasible. Dense time series with several hundreds of Landsat-like satellite images are rarely used to date. This study exemplifies opportunities of three approaches with respect to forest monitoring on a local study area on Vancouver Island (Canada). Each of the approaches has advantages and disadvantages that make it particularly powerful for certain purposes. The more datasets are involved the more complex the analysis becomes. At the same time, complex processes such as forest structural development can only be resolved with multi- to hyper-temporal datasets. Dense time series are an adequate means to account for the dominant temporal dimensions of forest development and change including phenological or seasonal variation, structural or long-term trends, as well as abrupt changes and changes in forest dynamics. Exploration of dense time series is the key to efficient use of upcoming high temporal resolution sensors such as Sentinel-2.

**Zusammenfassung:** *Bi-temporale Veränderungsdetektion, Veränderungstrajektorien und Zeitreihenanalyse sowie deren Anwendung im Waldmonitoring.* Traditionelle Veränderungsdetektion bezieht sich meist auf bi-temporale Ansätze. Durch die derzeitige offene Datenpolitik verschiedener Datenanbieter wird die Anwendung von multi- und hyper-temporalen Datensätzen für die Veränderungsdetektion und das Monitoring zunehmend praktikabel. Dichte Zeitreihen von mehreren Hundert Landsat-ähnlichen Satellitendaten werden aktuell nur wenig genutzt. Diese Studie zeigt beispielhaft die Möglichkeiten dreier verschiedener Ansätze in Bezug auf das Waldmonitoring an einem Untersuchungsgebiet auf Vancouver Island (Kanada). Jeder der drei Ansätze hat Vor- und Nachteile, die sie besonders leistungsstark für bestimmte Anwendungen machen. Je mehr Daten in die Analyse einbezogen werden, desto komplexer wird die Analyse. Gleichzeitig können komplexe Prozesse wie die Waldstrukturentwicklung nur mit multi- und hyper-temporalen Daten entschlüsselt werden. Dichte Zeitreihen sind ein geeignetes Mittel, um die dominanten zeitlichen Dimensionen der Waldentwicklung und -veränderung zu erfassen, darunter phänologische oder saisonale Schwankungen, strukturelle oder Langzeittrends sowie abrupte Veränderungen und Veränderungen in der Walddynamik. Die Analyse dichter Zeitreihen ist essenziell für den effizienten Einsatz zukünftiger Satelliten mit hoher zeitlicher Auflösung wie Sentinel-2.

## 1 Introduction

Change detection is a key remote sensing application. Many state-of-the-art methods were developed as early as in the 1970s and 1980s, e.g., image differencing (WEISMILLER et al. 1977), post-classification comparison (PCC) (JENSEN et al. 1987), or change vector analysis

(CVA) (MALILA 1980). From a technical perspective, remote sensing change detection is the identification of differences between two or more images. Generally, these changes can be measured in terms of intensity, frequency, spatial and temporal extent, spatial and temporal stability, rates and speed. Estimating change with remote sensing data of only one

acquisition requires detailed knowledge of the study site so that the features on the image can be related to processes on the ground. For long time, remote sensing analysts were mainly interested in what is known as conversion, i.e., the replacement of one land use class by another (COPPIN et al. 2004). Changes due to phenological changes of vegetation were frequently undesired, and it was seen as a prerequisite to avoid such changes by carefully selecting the images used for change detection. According to SINGH'S (1989) definition change detection is "the process of identifying differences in the state of an object or phenomenon by observing it at different times". Many comprehensive change detection reviews have been published (e.g., COPPIN et al. 2004, LU et al. 2004, SINGH 1989), most of them reflecting the long history of bi-temporal methods. Recent reviews include time series analysis (HECHELTJEN et al. 2014) but do not refer to forestry. Forest managers and climate modellers are not only interested in forest loss due to land use change. They also need detailed information about structural changes of the land cover including forest management, e.g., harvesting, replantation, and natural processes, e.g., forest growth, biomass accumulation, insect infestation, fire, and recovery. The opening of the Landsat archive in 2008 triggered the use of multi- to hyper-temporal datasets rather than bi-temporal data. However, to date there is no study examining potential and limits of each category. In the present paper, we compare bi-temporal change detection, change trajectory analysis and time series analysis and their implications for forest monitoring. We focus on a demonstration of specific advantages and disadvantages that complement the current understanding of change detection rather than rating each category according to achieved accuracies.

## 2 Data and Study Site

The study site is located on southern Vancouver Island, British Columbia, Canada (Fig. 1). Most of the area is composed of forested land. The Vancouver Island forests are a major resource for the Canadian timber and paper industry. Thus, there is a long history of forest

use and management. Dominant tree species in the southern part of Vancouver Island are western hemlock (*Tsuga heterophylla*), western redcedar (*Thuja plicata*), Amabilis fir (*Abies amabilis*), Douglas-fir (*Pseudotsuga menziesii*), yellow-cedar (*Chamaecyparis nootkatensis*), lodgepole pine (*Pinus contorta*), grand fir (*Abies grandis*), and Sitka spruce (*Picea sitchensis*) (POJAR et al. 1991). Red alder (*Alnus rubra*) is a widespread species on logged or otherwise disturbed sites (POJAR et al. 1991).

The area has a strong climatic gradient, pronounced topography, and complex ecosystem dynamics. Rainfall varies between about 700 mm per year in Victoria and more than 3500 mm per year at the west coast of Vancouver Island (GOVERNMENT OF CANADA 2011). Precipitation falls mainly as rain predominantly in autumn and winter. The study site (Fig. 1) was chosen in the overlapping part of two world reference system (WRS-2) tiles with path/row indices p048r026 and p047r026. The study site has an area of  $1000 \times 1000$  pixels (i.e.,  $30 \times 30$  km<sup>2</sup>) with elevation ranging from about sea level to heights of about 1.135 m. In the present study, we processed all available Landsat images taken between 1984 and end of 2012 available from the USGS Global Visualization Viewer (<http://glovis.usgs.gov/>). They amount in 1.550 scenes including cloudy images as well as Landsat ETM+ SLC-off data. In the eighties and nineties, winter acquisitions were rarely taken. With the start of Landsat 7 in 1999 and Landsat 5 working simultaneously

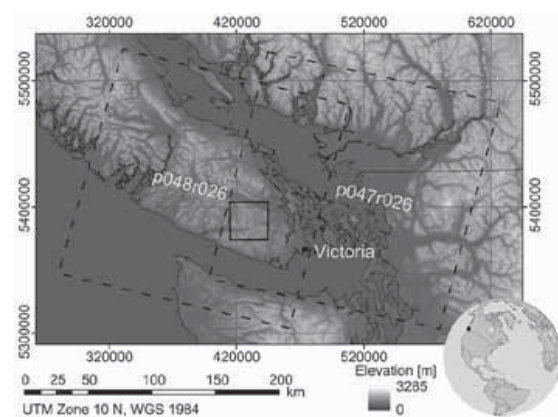


**Fig. 1:** Study site (black solid quadrangle) in the overlapping part of two neighbouring WRS-2 tiles (black dashed line).

the number of acquisitions was increased up to eight per month. The Scan Line Corrector (SLC) of Landsat 7 ETM+ failed in May 2003 resulting in data gaps whose extent increases towards the far edges of each scan resulting in a loss of about 22% per scene whilst the precise location of the missing scan lines varies from scene to scene (CHEN et al. 2011). From late 2011, no Landsat 5 TM data are available for the study area. Thus, only Landsat 7 ETM+ SLC-Off images are available for 2012. One additional cloud free image from Landsat 8 OLI from July 2013 was processed as a reference image at the end of the observation period. All Landsat data have been processed consistently in order to allow for automated time series analysis. The datasets used for the bi-temporal change detection and trajectory analysis have been selected from the cloud and gap free datasets.

### 3 Methods

#### 3.1 Pre-processing

Pre-processing included geometric and radiometric processing as well as cloud detection. The latter becomes relevant when all data of a time series are to be analyzed (ZHU & WOODCOCK 2014) or compositing techniques are chosen to create cloud free composites (GRIFFITHS et al. 2013).

The majority of the established change detection methods require high geometric registration accuracy at subpixel level as image misregistration may cause image object properties to be evaluated at incorrect locations. This can lead to the identification of spurious changes as well as the failure to identify genuine changes due to even slight dislocations of image objects (TOWNSHEND et al. 1992). Very good geometric quality is reported for Landsat data processed with the Landsat Product Generation System (LPGS) which processes all Landsat scenes to Standard Terrain Correction Level 1T if the required ground control and elevation data are available. We removed all images exceeding 80% cloud cover to assure good geometric quality. The resultant number of images is lowered from 1.550 to 778.

Atmospheric correction was applied to all images using the Landsat Ecosystem Disturbance Adaptive Processing System (LEDAPS) atmospheric correction tool (MASEK et al. 2006, VERMOTE et al. 1997).

Cloud cover is a severe problem when using optical data. This becomes even more evident when using time series of many images. For bi-temporal change detection and trajectory analysis cloud free images have been selected. The dataset used for time series analysis disregards the choice of cloud-free images. Instead, we made use of all cloud-free pixels. All pixels that are not contaminated by clouds, cloud shadows or snow are referred to as “clear”. Clear land pixels are clear pixels that do not show water bodies. Masking of clouds, cloud shadow, snow and water is essential. A sophisticated method was presented by ZHU & WOODCOCK (2012) with the object-based function of mask (Fmask) algorithm. It provides masks for clouds, cloud shadows, snow, and water. Recent advances extended the Fmask algorithm to reduce errors based on multi-temporal analysis of Landsat data (ZHU et al. 2012, ZHU & WOODCOCK 2014). In this study, we applied Fmask with standard configuration to all images and used the resultant mask to exclude contaminated pixels from time series analysis. Accordingly, each pixel has an individual time series. The number of observations varies over the image.

#### 3.2 Bi-temporal Forest Change Detection

Relatively few of the numerous change detection methods that have been developed go beyond the discrimination of changed and unchanged features (HECHELTJEN et al. 2014). Valuable information is added when additional information about the nature of change is provided. Change vector analysis (CVA) (MALILA 1980) is a widely used and robust method which produces two quantities of change information: 1) change magnitude which represents the intensity of change; and, 2) change direction which provides information about the spectral behaviour of the change vector. BOVOLO & BRUZZONE (2007) provided a comprehensive theoretical framework for CVA.

CVA performs change detection by differencing the spectral vectors of identical pixels in two co-registered multispectral images. The difference vector of all spectral bands can be described by its magnitude and its direction. Change magnitude is expressed as the Euclidean distance in the multidimensional feature space, calculated from the differences in each spectral band (1), (2):

$$x_{diff_i} = x_{2_i} - x_{1_i}, \quad (1)$$

$$m = \sqrt{\sum_{i=1}^n x_{diff_i}^2}, m \in [0, \max(m)], \quad (2)$$

where  $x_{1_i}$  and  $x_{2_i}$  are the reflectances of band  $i$  in images 1 and 2, respectively;  $x_{diff_i}$  is the difference of each band  $i$ ;  $m$  is the change magnitude; and  $n$  is number of bands.

Change direction indicates the spectral direction of change rather than providing from/to classes, e.g., increase or decrease in a given image band over time. It can be calculated in several ways. We adopt the methodology described by BOVOLO et al. (2010), who extended the polar domain approach (ALLEN & KUPFER 2000) to represent higher dimensional feature spaces in two dimensions (3):

$$\alpha = \cos^{-1} \left[ \frac{1}{\sqrt{n}} \left( \frac{\sum_{i=1}^n x_{diff_i}}{\sqrt{\sum_{i=1}^n x_{diff_i}^2}} \right) \right], \alpha \in [0, \pi], \quad (3)$$

where  $\alpha$  is the direction expressed as multidimensional angle.

To show the performance of the bi-temporal approach we used data taken virtually at the same day of the year but six years apart. The data are from 2004-07-24 and 2010-07-25. Both datasets are from the identical WRS-2 tile and from Landsat 5. Image noise that remains after atmospheric correction or results from sensor degradation was reduced by relative radiometric normalization using the iteratively re-weighted multivariate alteration detection (IR-MAD, CANTY & NIELSEN 2008). The T-point thresholding (COUDRAY et al. 2010) was applied to the magnitude component to separate change from no-change.

The final change detection map was derived by unsupervised clustering using the expectation maximization (EM) algorithm (BAZI et al. 2007). The map indicates vegetation losses, vegetation increases and unchanged vegetation. The study site does not cover urban areas. Thus, all occurring changes can be attributed to forest gain or loss.

### 3.3 Forest Change Trajectories

Trajectory analysis and time series analysis are often not clearly defined and the use of the terms is often confused. Time series in remote sensing simply describe a dataset consisting of a sequence of images taken from the same area at different times. Time series analysis, however, is related to the composition of a time series. Time series decomposition into trend, seasonal and remainder (noise) components is a common technique to characterize time series and describe their temporal behaviour. An example is the seasonal-trend decomposition procedure (STL) based on a locally weighted regression smoother (LOESS) (CLEVELAND et al. 1990). A well-established method for time series analysis of remote sensing data is breaks for additive season and trend (BFAST) (VERBESSELT et al. 2010a, VERBESSELT et al. 2010b) which allows for the detection of long-term trends and of abrupt breaks in the trend and seasonal components. Whereas many recent studies use time series they do not apply time series analysis in terms of decomposition (e.g., GRIFFITHS et al. 2012, KENNEDY et al. 2007). Since most of these approaches aim at fitting trend models and deriving trends from the data (LAWRENCE & RIPPLE 1999, KENNEDY et al. 2007, KENNEDY et al. 2010) they can be seen as a combination of time series analysis and trajectory analysis. As all of these studies focus on annual or less data, seasonal patterns cannot be explored.

Trajectory analysis in the present study is understood as analyzing multi-temporal datasets that have one observation per year or less. In the present case study, the trajectory is a composition of multiple bi-temporal change detection results. Trends have to be interpreted from the derived map rather than calculated from observed physical properties such

**Tab. 1:** Data used for change trajectories.

Dates	Path/Row	Sensor
1984-07-17	048/026	Landsat 5 TM
1986-08-08	048/026	Landsat 5 TM
1989-10-03	048/026	Landsat 5 TM
1992-08-17	047/026	Landsat 5 TM
1995-09-02	048/026	Landsat 5 TM
1998-09-26	048/026	Landsat 5 TM
2001-09-10	048/026	Landsat 7 ETM+
2004-07-24	048/026	Landsat 5 TM
2007-09-12	047/026	Landsat 5 TM
2010-07-25	048/026	Landsat 5 TM
2013-07-26	047/026	Landsat 8 OLI

as the normalized difference vegetation index (NDVI) or other spectral indices.

We take advantage of the CVA approach and perform bi-temporal change detection on consecutive image pairs instead of individually classifying them. LUNETTA et al. (2004) used CVA to assess land cover changes in a forested area in North Carolina in a similar approach. Their findings indicate that a repetition rate of 3 – 5 years is required to monitor forest cover change. Higher temporal resolution is recommended, however. For the 29-year observation period in our study we chose a time interval of about three years. The first time step is only two years (Tab. 1). Consequently, a dataset with 11 time steps was created. Ten individual bi-temporal change detection tasks have been performed as described in section 3.2. The individual results were subsequently combined in a way that allows to visualize the time span where the most intense changes have happened. These can be attributed to forest clearings.

### 3.4 Time Series Analysis for Forest Monitoring

Recent advances in medium and high resolution remote sensing focus on time series, i.e., trend analysis (DUBOVYK et al. 2013) or time series reconstruction by segmented regression modeling (KENNEDY et al. 2010). Most of these methods focus on trends or abrupt

changes (e.g., GRIFFITHS et al. 2012). The combined analysis of trends, seasonal cycles, and abrupt changes is rarely applied (VERBESSELT et al. 2010a, VERBESSELT et al. 2010b). A problem with Landsat data may be its irregular time spacing since many time series methods require regular time spacing.

Interpolation is a commonly applied technique in time series analysis to fill gaps (VERBESSELT et al. 2006). The average gap length in our time series varies between less than 20 days and more than 70 days in less favoured areas. The real gap length varies between 1 day (cross-sensor Landsat 5/7 and adjacent tiles) and more than 1000 days in the high altitude regions and along shorelines. As the time series contain outliers in spite of masking clouds and missing observations, filtering was applied to reduce noise. An adequate state-of-the-art method is the Savitzky-Golay filtering (SAVITZKY & GOLAY 1964) which is also used in other time series approaches (JÖNSSON & EKLUNDH 2004). As indicated previously great benefit of time series is expected in understanding additional process dimensions such as seasonal pattern and their changes over time, long-term trend direction and intensity, timing and intensity of abrupt changes, and subtle changes that might be lost when looking only on trends. These processes are usually not directly related to spectral responses. Some indices, however, are suitable to characterize at least some of the processes to a certain degree although additional information is often required for better characterization, e.g., lidar to quantify biomass accumulation (DUNCANSON et al. 2010). The selection of appropriate spectral indices is essential to understand forest development. An index that is closely related to the structure of coniferous forests is the normalized difference moisture index (NDMI) (HARDISKY et al. 1983). It is calculated from near-infrared (NIR) and shortwave-infrared (SWIR) bands as follows (4). The numbers in brackets indicate the respective Landsat TM/ETM+ bands:

$$\text{NDMI} = \frac{\text{NIR}(4) - \text{SWIR}(5)}{\text{NIR}(4) + \text{SWIR}(5)} \quad (4).$$

As the SWIR band is sensitive to foliage water content and the fraction of dead leaf ma-

terial, NDMI is promising in forest monitoring (GOODWIN et al. 2008). The pre-processing of the dense time series did not include radiometric normalization because IR-MAD obscures seasonal variation. Whereas this is appreciated in many bi-temporal studies where seasonal variation is considered as noise, it is important to keep the seasonal variation pattern in time series because of its additional information content.

As our main focus is on abrupt changes and recovery we used a robust method to detect breaks in the Landsat time series and estimate recovery trends subsequently. The interpolated and filtered NDMI time series was analyzed for discontinuities by applying the Webster measure (WEBSTER 1973). This measure is calculated with a pixel-based temporal moving window that is divided in two parts. For each part the mean is calculated, and the difference of the left hand and right hand means is plotted. The timing of change is assumed at the point with the biggest difference, i.e., the minimum value. The size of the moving window was defined with a width of 365 days. Hence, the time period considered in the moving window is always one full year, ensuring that seasonality is leveled out. This means that in a time series without change the Webster measure will be zero. To ensure the presence of real changes rather than outliers in the time series and at the same time preventing fixed thresholds, a statistical non-parametric Kolmogorov-Smirnov test was performed. Once the break point is detected several properties of the time series may be analyzed, e.g., magnitude of change or recovery rate following the disturbance. The recovery trends are not linear but for ease of interpretation we calculated linear trends for the periods directly following the clearcut event. The time series based change detection method follows the workflow presented in THONFELD et al. (2014):

- a) Construction of individual NDMI time series for each pixel
- b) Linear interpolation between all observations to create equally-spaced time series
- c) Filtering the time series using Savitzky-Golay filter (window = 365)
- d) Application of Webster discontinuity measure on the filtered time series

- e) Determination of the minimum in the Webster measure as the indicator of the break date
- f) Performing the statistical non-parametric Kolmogorov-Smirnov test
- g) Calculation of change properties, e.g., timing of change, intensity of change, recovery rates after change event

From dense time series of forests several features can be calculated that describe the temporal behaviour of the index including date, duration and intensity of abrupt changes, shifts in seasonality, trends before and after major change events, date, duration and intensity of secondary changes, long-term anomalies, and regrowth rates.

### 3.5 Accuracy Assessment

The validation of change detection results is particularly challenging due to the very common lack of reference data for all time steps. Frequently, available ground information is of different date than the image data. The detection of clearcuts in Landsat images by means of visual interpretation is feasible because their size is often several hectares, and the spectral change signal is usually very clear. However, analysts often apply minimum mapping units or spatial filters to get rid of small change areas which are often difficult to validate visually. Our validation procedure is based on the time series analysis. Studies exploring annual time series refer to the year of disturbance onset or the first year with detected disturbance (GRIFFITHS et al. 2012). We derived reference data from the dense Landsat time series itself since this dataset provides most comprehensive temporal information. Bi-temporal datasets (as well as annual time series) allow indicating a period of change rather than an exact year. We applied stratified random sampling on the time series results to select 30 pixels per disturbance year plus 30 pixels from the undisturbed pixels. For each of the resulting 900 locations we extracted the NDMI time series, plotted and manually checked them. For some of the reference points the labels had to be revised. This was mainly because the changes happened in late fall of the previous year rather than in spring of the next year. For

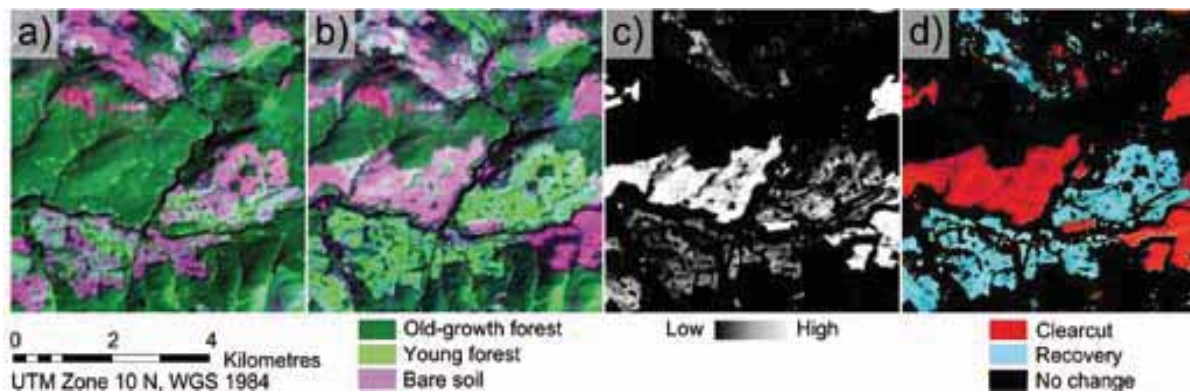


**Fig. 2:** Subset of the study site ( $6 \times 6 \text{ km}^2$ ), a) Landsat from 2004-07-24, b) Landsat from 2010-07-25 (RGB = 7-4-2), c) masked change magnitude, and d) masked change directions.

each of the 900 locations we checked if change and no-change pixels were detected correctly. For the trajectory and the time series we also evaluated if the year of change was specified correctly. The reference dataset was adjusted to the bi-temporal study and the trajectory, respectively. If there was a clearcut before the time covered by two observations, it was labeled as regrowth in the reference map.

#### 4 Results and Discussion

The results of the bi-temporal change detection based on CVA are shown in Fig. 2. It can be seen that the two major changes, i.e., forest loss due to clearcut harvesting (red) and forest recovery due to the establishment of new forest cohorts (blue), are well displayed in the direction component (Fig. 2d). Change intensity, i.e., magnitude, is shown in Fig. 2c in grey levels with bright colours indicating strong changes and dark areas indicating small or no changes. Since forest regrowth is rather slow compared to forest clearcut harvest, the change magnitude is higher for forest loss where the spectral signature has completely changed. Detectability of regrowth depends on the time-lag between the two images and the growth rate of the forest. The forests of the study site grow rather slowly. The overall accuracy of the final map indicating clearcuts, recovery, and unchanged areas was only 51.9%. The main reason is that recovery is a long-term process that causes only gentle spectral changes compared to the strong changes of clearcuts. Thus, the selection of ap-

propriate thresholds is challenging. The accuracy of clearcut detection, i.e., ignoring recovery, was 93.4%.

Results of the change trajectory analysis are shown in Fig. 3. The major changes, i.e., clearcuts, are displayed with the colours indicating the time span where the harvest happened. A specific date of the harvest events cannot be derived. The detected change patches retrace the clearcuts well. Some groups of trees left standing inside the clearcuts show up as well as small-scale change patches that have been rendered to install new forest roads. In the southern part of the study site, some mapped elongated clearcut patches are a result of topographic effects rather than real changes. It can be seen in Tab. 1 that it was not possible to establish a time series of annual data. Some off-season data had to be used. The results confirm that off-annual data should

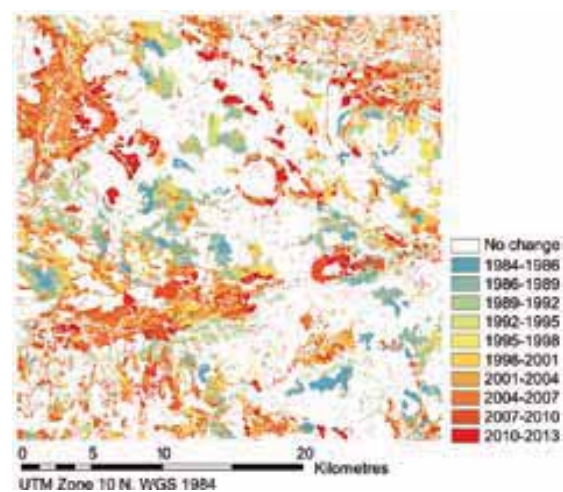


**Fig. 3:** Time span of clearcut events as result of change trajectory analysis.

be preferred over off-seasonal data. Assessing the regrowth rates is rather challenging with the data used for this experiment whereas clearcuts can be well detected even after a time lag of one or two years. The overall accuracy was 69.6%. However, the visual inspection of the dense time series revealed that there was often more than one change event in a time series. The trajectory analysis did only account for the first strong change signal. However, that one is sometimes not the most pronounced in a time series. In other words, changes are often well detected but at wrong dates. The analysis if change was correctly seen as change, and thereby ignoring the correctness of the date, revealed an overall accuracy of 91.4%.

Results of the time series analysis are shown in Fig. 4. The break date can be iden-

tified accurately. Besides the precise year of change, even the month of the clearcut can be derived (Fig. 4a, b). As the forest harvest within a clearcut area takes several weeks until all trees, branches, and woody debris are removed, there is some bias in this information. However, start, end and duration of the clearcut can be derived, e.g., break duration in Fig. 4c. A combined map of clearcut events detected during the observation period and trends is shown in Fig. 4d. The trends refer to those areas that have been harvested before the start of the observation period and regrow since that time. White areas refer to mature and old-growth forests or to non-forest areas. Years of change were detected with an accuracy of 93.1%. The overall accuracy of correctly identified changes was 95.4%.

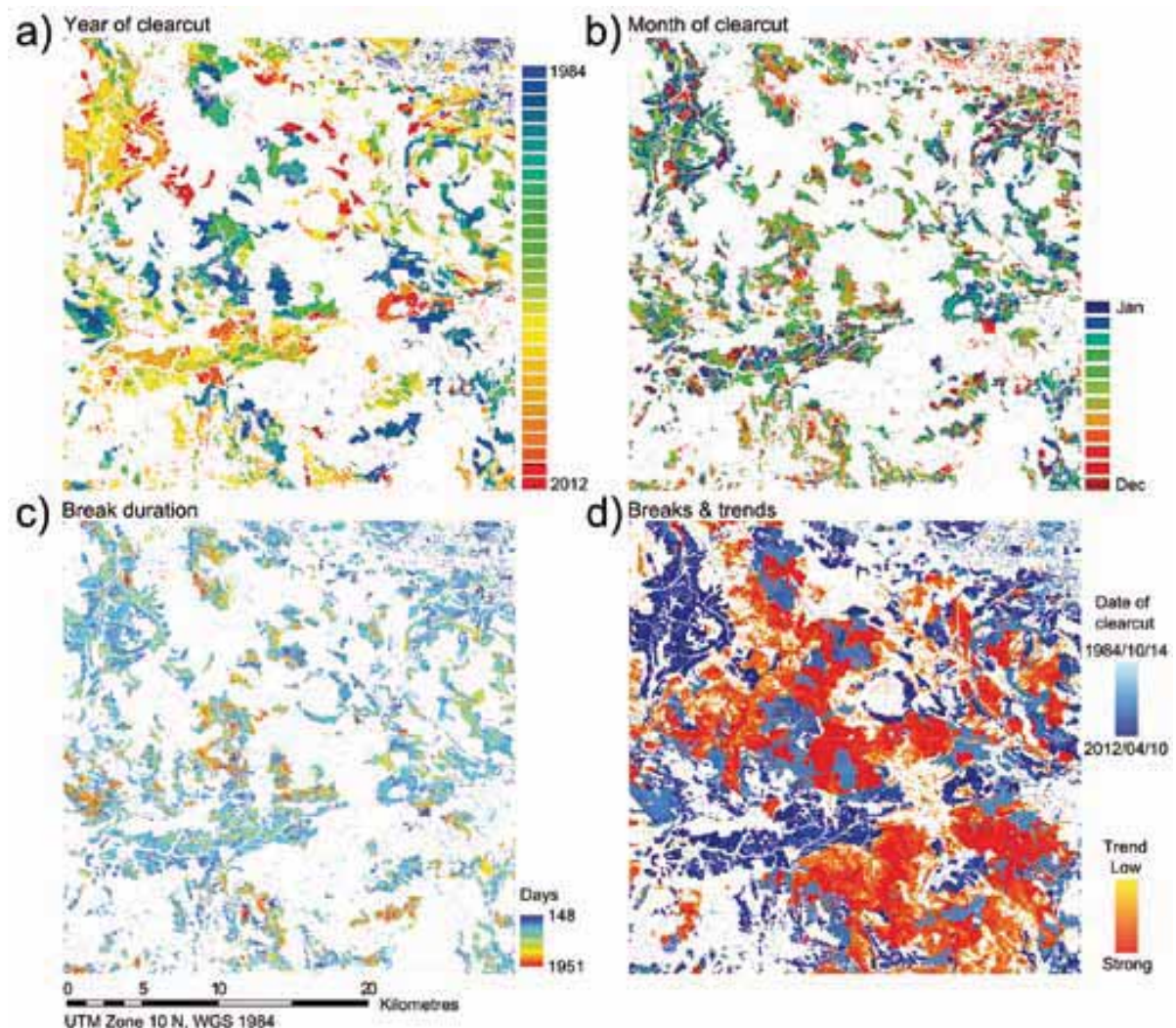


**Fig. 4:** Results of time series analysis: a) year of clearcut, b) month of clearcut, c) break duration, and d) combined break date and trend map.

**Tab. 2:** Comparison of bi-temporal change detection, multi-temporal change detection, and time series analysis.

	<b>Bi-temporal change detection</b>	<b>Multi-temporal change detection (including trajectories of annual observations)</b>	<b>Time series analysis (more than one observation per year)</b>
Suitable to detect abrupt changes?	yes	yes	yes
Suitable to detect long-term trends?	no, trends cannot be clearly separated from noise or phenological differences	yes	yes
Suitable to detect seasonal variation, e.g. phenology?	no	no, inter-annual changes that fall below a certain threshold are considered noise, those above are seen as abrupt change	yes
Date of change detectable?	no, it is only known that the change happened between two observations	a rather coarse indication of the date of abrupt changes can be estimated	changes can be detected with good temporal precision
Major pre-processing steps	co-registration; atmospheric correction or radiometric normalization; (manual) scene selection	geometric & radiometric processing (atmospheric correction, radiometric normalization); cloud detection; scene selection; compositing	geometric & radiometric processing (atmospheric correction); cloud detection
Requirements	cloudfree scenes; ideally equal phenological conditions & equal sun position	cloudfree pixels; each observation must be chosen with respect to rainfall, phenology, and sun illumination	cloudfree observations
Option to label changes?	yes, several methods exist (HECHELTJEN et al. 2014)	yes, if multi-temporal classifications are compared; usually, the change itself can be related to a certain class	yes (ZHU & WOODCOCK 2014); usually, the change itself can be related to a certain class
Advantages	small data volume; many algorithms (see COPPIN et al. 2004, HECHTLJEN et al. 2014)	moderate data volume; good balance of outcome and effort; trends and abrupt changes detectable	seasonal effects, inter- & intra-annual dynamics detectable; all observations used; no scene selection or compositing required; almost gapless process characterization; option of time series decomposition; no thresholding required
Limitations	processes and their spatio-temporal characteristics are not detectable; thresholding required to separate change from no-change	data selection and/or compositing required; areas of frequent cloud coverage; seasonal variation & dynamics are not detectable; data availability in some regions	big data volume; comprehensive preprocessing requires automation; data availability in some regions
Application	various, e.g., emergency response, flood detection, urban expansion	various, e.g., forest cover change, mining	various, e.g., forest cover change, continuous map update
Examples of methods	CVA , Post Classification Comparison	LandTrendr	BFAST, time series approach used here

Some of the most relevant characteristics of the three approaches demonstrated in this study are listed in Tab. 2. The information content that can be derived with bi-temporal datasets, trajectories of triennial data, and dense time series with gaps in the range of few days to several weeks increases with the number of available observations (cf. rows 1-3 in Tab. 2). Secondary changes, information on seasonal variation and changes therein are not displayed in Fig. 4. However, this information can be derived from the dense time series as well.

Although bi-temporal change detection (cf. column 2 of Tab. 2) is very powerful in forest change detection it is rarely used in operational monitoring projects. Methods such as the land-cover change mapper (LCM) (CASTILLA et al. 2009) are efficient tools but require knowledge of the study site for the interpretation of changes. The bi-temporal example shown here based on CVA provides additional information about the nature of change. The link to processes, however, is challenging. Any quantification needs well adjusted images that do not only account for illumination differences but also for phenological differences and weather impacts such as rainfall, drought, and wind. Even annual data do not guarantee identical phenological conditions. Radiometric normalization may reduce noise but does not eliminate illumination differences that occur when off-season data are used. The problem of finding data taken under comparable conditions becomes even more critical when time series are used. Although the summers on Vancouver Island are relatively dry, the time suitable for cloud free acquisitions is rather limited. Recently, compositing techniques have been developed (GRIFFITHS et al. 2013) to avoid the laborious and sometime misleading task of seeking cloud free images. Those techniques aim at finding clear land pixels that are as close to a predefined reference date as possible. Off-year acquisitions are preferred over off-seasonal images (WULDER et al. 2004). Compositing is promising when annual data are sufficient or when several tiles have to be combined to seamless image mosaics. In a way compositing can be seen as a data reduction which may also be regarded as a disadvantage. Data reduction also

means information loss. To date only a very small portion of the Landsat archive has been explored (WULDER et al. 2012). Exploring all datasets may improve our understanding of processes on the ground rather than disregarding the vast majority of datasets.

The trajectory analysis presented here is suitable to detect major changes, i.e., timber extraction and forest regrowth. The detection of insect infestation and other subtle changes is difficult with such datasets or even annual time series because they are often too weak to exceed the noise level that is included in these time series. Consequently, subtle changes are often identified as noise. The quantification of the forest recovery is also challenging because the timing of each acquisition has enormous impact on the shape of the recovery curve. Change trajectories of classified images are thus of limited use in forest studies. Trends can be derived from trajectories (cf. column 3 of Tab. 2) with appropriate methods such as Landsat-based detection of trends in disturbance and recovery (LandTrendr) (KENNEDY et al. 2010). This time series segmentation techniques calculates trend curves based on any spectral index. It is very powerful in detecting strong changes. The accuracy of the recovery trends, however, is hard to estimate. Divergence from idealized time series models is considered noise. Compositing techniques are an appropriate means to reduce spurious changes that result from imperfect data. Noise is reduced as well. Seasonal dynamics, inter-annual variation and non-linear dynamics, however, are neither displayed in annual time series nor in trajectories of categorized data.

A more comprehensive way towards better understanding of ecosystem processes, landscape dynamics, and their relationship to driving forces is using all available information. This can be achieved by using Moderate Resolution Imaging Spectroradiometer (MODIS)-like standardised products such as the 16-day-NDVI product (ROY et al. 2010), the multitemporal multispectral modeling of land cover classes based on all observations (ZHU & WOODCOCK 2014) or the time series analysis approach used here. Future satellite missions such as Sentinel-2 will deliver data at high temporal resolution. Comprehensive ecosystem process understanding requires the ef-

ficient exploration of as many observations as possible – including multi-sensor approaches.

## 5 Conclusion

The study presented here revealed that each of the three different change detection strategies has advantages and disadvantages that make it suitable for different applications in forest management. The most comprehensive information can be derived from dense time series. The superiority in information detail is at the expense of high computational efforts. With the launch of recent, e.g., Landsat 8, and upcoming, e.g., Sentinel-2, sensors the processing of dense time series is likely to become more feasible also in regions that have been less covered to date. When processes are in the scope of a study, remote sensing based time series are a good means for improved understanding. Forest monitoring and forest change detection requires high spatial and temporal resolution for comprehensive structural characterization and process understanding which can be achieved with dense time series. The use of dense time series does not only deliver more information about ongoing processes; changes can also be detected with higher temporal precision and higher accuracy.

## Acknowledgement

We wish to thank MORTON J. CANTY for his free ENVI/IDL implementation of IR-MAD (<http://ms-image-analysis.appspot.com/static/homepage/index.html>), ZHE ZHU and CURTIS E. WOODCOCK for providing the Fmask (<https://code.google.com/p/fmask/>) and JEFFREY G. MASEK for providing the LEDAPS software tools (<http://ledaps.nascom.nasa.gov/tools/tools.html>). ENVI/IDL and R were used for scripting and change detection analyses.

## References

- ALLEN, T.R. & KUPFER, J.A., 2000: Application of Spherical Statistics to Change Vector Analysis of Landsat Data: Southern Appalachian Spruce-Fir Forests. – *Remote Sensing of Environment* **74** (3): 482–493.
- BAZI, Y., BRUZZONE, L. & MELGANI, F., 2007: Image thresholding based on the EM algorithm and the generalized Gaussian distribution. – *Pattern Recognition* **40** (2): 619–634.
- BOVOLO, F. & BRUZZONE, L., 2007: A Theoretical Framework for Unsupervised Change Detection Based on Change Vector Analysis in the Polar Domain. – *IEEE Transactions on Geoscience and Remote Sensing* **45** (1): 218–236.
- BOVOLO, F., MARCHESI, S. & BRUZZONE, L., 2010: A nearly lossless 2d representation and characterization of change information in multispectral images. – *IEEE International Geoscience and Remote Sensing Symposium (IGARSS)*: 3074–3077.
- CANTY, M.J. & NIELSEN, A.A., 2008: Automatic radiometric normalization of multitemporal satellite imagery with the iteratively re-weighted MAD transformation. – *Remote Sensing of Environment* **112** (3): 1025–1036.
- CASTILLA, G., GUTHRIE, R.H. & HAY, G.J., 2009: The land-cover change mapper (LCM) and its application to timber harvest monitoring in Western Canada. – *Photogrammetric Engineering & Remote Sensing* **75** (8): 941–950.
- CHEN, J., ZHU, X., VOGELMANN, J.E., GAO, F. & JIN, S., 2011: A simple and effective method for filling gaps in Landsat ETM+ SLC-off images. – *Remote Sensing of Environment* **115** (4): 1053–1064.
- CLEVELAND, R.B., CLEVELAND, W.S., McRAE, J.E. & TERPENNING, I., 1990: STL: A Seasonal-Trend Decomposition Procedure Based on Loess. – *Journal of Official Statistics* **6** (1): 3–73.
- COPPIN, P., JONCKHEERE, I., NACKAERTS, K., MUYS, B. & LAMBIN, E., 2004: Digital change detection methods in ecosystem monitoring: a review. – *International Journal of Remote Sensing* **25** (9): 1565–1596.
- COUDRAY, N., BUSSLER, J.-L. & URBAN, J.-P., 2010: Robust threshold estimation for images with unimodal histograms. – *Pattern Recognition Letters* **31** (9): 1010–1019.
- DUBOVYK, O., MENZ, G., CONRAD, C., KAN, E., MACHWITZ, M. & KHAMZINA, A., 2013: Spatio-temporal analyses of cropland degradation in the irrigated lowlands of Uzbekistan using remote-sensing and logistic regression modeling. – *Environmental Monitoring and Assessment* **185** (6): 4775–4790.
- DUNCANSON, L.I., NIEMANN, K.O. & WULDER, M.A., 2010: Integration of GLAS and Landsat TM data for aboveground biomass estimation. – *Canadian Journal of Remote Sensing* **36** (2): 129–141.
- GOODWIN, N.R., COOPS, N.C., WULDER, M.A., GILLANDERS, S., SCHROEDER, T.A. & NELSON, T., 2008: Estimation of insect infestation dynamics

- using a temporal sequence of Landsat data. – *Remote Sensing of Environment* **112** (9): 3680–3689.
- GOVERNMENT OF CANADA, 2011: Canadian Climate Normals. – [http://climate.weather.gc.ca/climate\\_normals/](http://climate.weather.gc.ca/climate_normals/) (18.1.2015).
- GRIFFITHS, P., KUEMMERLE, T., KENNEDY, R.E., ABRUDAN, I.V., KNORN, J. & HOSTERT, P., 2012: Using annual time-series of Landsat images to assess the effects of forest restitution in post-socialist Romania. – *Remote Sensing of Environment* **118**: 199–214.
- GRIFFITHS, P., VAN DER LINDEN, S., KUEMMERLE, T. & HOSTERT, P., 2013: A Pixel-Based Landsat Compositing Algorithm for Large Area Land Cover Mapping. – *IEEE Journal of Selected Topics in Applied Earth Observations and Remote Sensing* **6** (5): 2088–2101.
- HARDISKY, M.A., KLEMAS, V. & SMART, R.M., 1983: The Influence of Soil Salinity, Growth Form, and Leaf Moisture on-the Spectral Radiance of *Spartina alterniflora* Canopies. – *Photogrammetric Engineering & Remote Sensing* **49**: 77–83.
- HECHELTJEN, A., THONFELD, F. & MENZ, G., 2014: Recent Advances in Remote Sensing Change Detection – A Review. – MANAKOS, I. & BRAUN, M., eds.: *Land Use and Land Cover Mapping in Europe*. – Springer Netherlands, Dordrecht: 145–178.
- JENSEN, J.R., RAMSEY, E.W., MACKAY, H.E., CHRISTENSEN, E.J. & SHARITZ, R.R., 1987: Inland Wetland Change Detection Using Aircraft MSS Data. – *Photogrammetric Engineering & Remote Sensing* **53** (5): 521–529.
- JÖNSSON, P. & EKLUNDH, L., 2004: TIMESAT – a program for analyzing time-series of satellite sensor data. – *Computers & Geosciences* **30** (8): 833–845.
- KENNEDY, R.E., COHEN, W.B. & SCHROEDER, T.A., 2007: Trajectory-based change detection for automated characterization of forest disturbance dynamics. – *Remote Sensing of Environment* **110** (3): 370–386.
- KENNEDY, R.E., YANG, Z. & COHEN, W.B., 2010: Detecting trends in forest disturbance and recovery using yearly Landsat time series: 1. LandTrendr – Temporal segmentation algorithms. – *Remote Sensing of Environment* **114** (12): 2897–2910.
- LAWRENCE, R.L. & RIPPLE, W.J., 1999: Calculating change curves for multitemporal satellite imagery: Mount St. Helens 1980–1995. – *Remote Sensing of Environment* **67** (3): 309–319.
- LU, D., MAUSEL, P., BRONDIZIO, E. & MORAN, E., 2004: Change detection techniques. – *International Journal of Remote Sensing* **25** (12): 2365–2401.
- LUNETTA, R.S., JOHNSON, D.M., LYON, J.G. & CROTWELL, J., 2004: Impacts of imagery temporal frequency on land-cover change detection monitoring. – *Remote Sensing of Environment* **89** (4): 444–454.
- MALILA, W.A., 1980: Change vector analysis: an approach for detecting forest changes with Landsat. – 6th Annual Symposium on Machine Processing of Remotely Sensed Data: 329–335, Purdue University, IN, USA.
- MASEK, J.G., VERMOTE, E.F., SALEOUS, N.E., WOLFE, R., HALL, F.G., HUENNRICH, K.F., GAO, F., KUTLER, J. & LIM, T.-K., 2006: A Landsat surface reflectance dataset for North America, 1990–2000. – *IEEE Geoscience and Remote Sensing Letters* **3** (1): 68–72.
- POJAR, J., KLINKA, K. & DEMARCHI, D.A., 1991: Chapter 6: Coastal Western Hemlock Zone. – MEIDINGER, D.V. & POJAR, J., eds.: *Ecosystems of British Columbia*. BC Ministry of Forests: 95–112, Victoria, B.C., Canada.
- ROY, D.P., JU, J., KLINE, K., SCARAMUZZA, P.L., KOVALSKYY, V., HANSEN, M., LOVELAND, T.R., VERMOTE, E. & ZHANG, C., 2010: Web-enabled Landsat Data (WELD): Landsat ETM+ composited mosaics of the conterminous United States. – *Remote Sensing of Environment* **114** (1): 35–49.
- SAVITZKY, A. & GOLAY, M.J., 1964: Smoothing and differentiation of data by simplified least squares procedures. – *Analytical chemistry* **36** (8): 1627–1639.
- SINGH, A., 1989: Review Article Digital change detection techniques using remotely-sensed data. – *International Journal of Remote Sensing* **10** (6): 989–1003.
- THONFELD, F., FEILHAUER, H., DUBOVYK, O., SCHMIDT, M. & MENZ, G., 2014: Multi-decadal forest monitoring using dense satellite time series. – Poster Presentation Sentinel-2 for Science Workshop. ESA-ESRIN, Frascati (Rome), Italy.
- TOWNSHEND, J.R.G., JUSTICE, C.O., GURNEY, C. & MCMANUS, J., 1992: The impact of misregistration on change detection. – *IEEE Transactions on Geoscience and Remote Sensing* **30** (5): 1054–1060.
- VERBESSELT, J., JONSSON, P., LHERMITTE, S., VAN AARDT, J. & COPPIN, P., 2006: Evaluating satellite and climate data-derived indices as fire risk indicators in savanna ecosystems. – *IEEE Transactions on Geoscience and Remote Sensing* **44** (6): 1622–1632.
- VERBESSELT, J., HYNDMAN, R., NEWNHAM, G. & CULVENOR, D., 2010a: Detecting trend and seasonal changes in satellite image time series. – *Remote Sensing of Environment* **114** (1): 106–115.

- VERBESSELT, J., HYNDMAN, R., ZEILEIS, A. & CULVENOR, D., 2010b: Phenological change detection while accounting for abrupt and gradual trends in satellite image time series. – *Remote Sensing of Environment* **114** (12): 2970–2980.
- VERMOTE, E.F., EL SALEOUS, N., JUSTICE, C.O., KAUFMAN, Y.J., PRIVETTE, J.L., REMER, L., ROGER, J.C. & TANRÉ, D., 1997: Atmospheric correction of visible to middle-infrared EOS-MODIS data over land surfaces: Background, operational algorithm and validation. – *Journal of Geophysical Research* **102** (D14): 17131–17141.
- WEBSTER, R., 1973: Automatic soil-boundary location from transect data. – *Journal of the International Association for Mathematical Geology* **5** (1): 27–37.
- WEISMILLER, R.A., KRISTOF, S.J., SCHOLZ, D.K., ANUTA, P.E. & MOMIN, S.M., 1977: Change detection in coastal zone environments. – *Photogrammetric Engineering & Remote Sensing* **43** (12): 1533–1539.
- WULDER, M.A., FRANKLIN, S.E. & WHITE, J.C., 2004: Sensitivity of hyperclustering and labelling land cover classes to Landsat image acquisition date. – *International Journal of Remote Sensing* **25** (23): 5337–5344.
- WULDER, M.A., MASEK, J.G., COHEN, W.B., LOVELAND, T.R. & WOODCOCK, C.E., 2012: Opening the archive: How free data has enabled the science and monitoring promise of Landsat. – *Remote Sensing of Environment* **122**: 2–10.
- ZHU, Z. & WOODCOCK, C.E., 2012: Object-based cloud and cloud shadow detection in Landsat imagery. – *Remote Sensing of Environment* **118**: 83–94.
- ZHU, Z., WOODCOCK, C.E. & OLOFSSON, P., 2012: Continuous monitoring of forest disturbance using all available Landsat imagery. – *Remote Sensing of Environment* **122**: 75–91.
- ZHU, Z. & WOODCOCK, C.E., 2014: Continuous change detection and classification of land cover using all available Landsat data. – *Remote Sensing of Environment* **144**: 152–171.

#### Address of the Authors:

Dr. FRANK THONFELD, ANTJE HECHELTJEN & Prof. Dr. GUNTER MENZ, Rheinische Friedrich-Wilhelms-Universität Bonn, Geographisches Institut, Zentrum für Fernerkundung der Landoberfläche (ZFL), D-53113 Bonn, Tel.: +49-228-73-4975, Fax: +49-228-73-6857, e-mail: {frank.thonfeld}{a.hecheltjen}{g.menz}@uni-bonn.de

Manuskript eingereicht: September 2014

Angenommen: Januar 2015





# Enhancement of Lidar Planimetric Accuracy using Orthoimages

KRZYSZTOF BAKUŁA, WOJCIECH DOMINIK & WOJCIECH OSTROWSKI, Warsaw, Poland

**Keywords:** lidar, accuracy, georeferencing, orthoimage, quality, algorithms

**Summary:** In this study the planimetric accuracy of lidar data was verified by registration of laser reflection images, point cloud modelling results and true orthophoto. The presented research is the basis for improving the accuracy of the lidar processing products, which is particularly important in issues related to surveying measurements. In the experiment, the true orthophoto generated by dense matching of aerial images was used to check for the planimetric accuracy of lidar data in two proposed approaches. The first (intensity-based) analysis is carried out by comparing coordinates of manually selected, salient points in the true orthoimages and rasters of the lidar reflection intensity. The second (feature-based) method to verify planimetric accuracy is based on matching roof ridges extracted from lidar data and true orthoimages. Both analyses were carried out for 3 fragments of lidar strips. A detected systematic planimetric error in the centimetre level range enabled the implementation of appropriate local correction for the analyzed data. The presented solutions provide an opportunity to improve the planimetric accuracy of lidar data that allow its efficient usage.

**Zusammenfassung:** *Die Verbesserung der Lidar Lagegenauigkeit mit Orthofotos.* In dieser Studie wurde die Lagegenauigkeit von Daten aus Airborne Laserscanning (ALS) unter Verwendung von Messungen der aufgezeichneten Reflexionsintensität des Laserstrahls und der Modellierung von Punktwolken analysiert. Die Ergebnisse wurden verwendet, um die Genauigkeit der Verarbeitung von Lidar-Daten zu verbessern. Diese Art der Verarbeitung ist bei geodätischen Messungen besonders wichtig. Orthofotos wurden verwendet, um die Lagegenauigkeit von ALS Ergebnissen zu bewerten. Die Genauigkeit wurde mit zwei Verfahren bestimmt. Das erste basierte auf einem Vergleich der Position ausgewählter Punkte auf Luftbildaufnahmen mit Punkten auf dem Raster der Reflexionsintensität (Intensität-basiertes Verfahren). Das zweite Verfahren (Feature-basiertes Verfahren) verwendet zur Prüfung der Lagegenauigkeit Dachfirste von Gebäudemodellen aus Lidar-Daten. Diese Analysen erlauben die Erkennung systematischer Fehler von wenigen Zentimetern und damit die Berücksichtigung der entsprechenden lokalen Änderungen. Insgesamt, ermöglicht dieser Ansatz, die Genauigkeit der Lidar-Daten zu verbessern und deren Nutzung effizienter zu gestalten.

## 1 Introduction

Aerial 3D data acquisition is currently dominated by two leading technologies. The first is the usage of aerial images and their subsequent matching, and the second is airborne laser scanning (ALS). Both technologies are often considered as alternatives for 3D data collection and for the generation of consecutive products, such as digital elevation models and 3D city models. Moreover, products resulting from a fusion of these two data sources have

become increasingly more common in recent years. Their interaction for accuracy improvement of the final products has also been observed recently (PARK et al. 2011, BEGER et al. 2011, PARMEHR et al. 2013, GERKE & XIAO 2014).

Aerial images have been acquired since the beginning of photography. Over more than a century of development of photogrammetry very sophisticated methods of image processing and data acquisition were elaborated. Aerial images have been the main primary

source of data for most cartographic products for decades. Image data allow for the precise identification of control points. This results in centimetre-level planar accuracy of the exterior orientation of the images and facilities measurement accuracy better than the ground sampling distance (GSD). However, image-based approaches tend to fail in areas covered with vegetation and are labour-intensive. The advantage of automatic image-based data acquisition methods is the collection of 3D information from one source. Dense matching of images has revolutionised photogrammetry in the last decade and given an impulse to further development of automatic photogrammetric measurement methods. Since the publication of the semi-global matching (SGM) algorithm (HIRSCHMÜLLER 2008) much research into its application to aerial images has been conducted. The main areas of research are related to the application of the very dense point cloud for the generation of high quality digital surface models (DSM), digital terrain models (DTM) and 3D building models. The accuracy and other quality aspects of point clouds generated by dense image matching have been investigated in ROTHERMEL & HAALA (2011) and HIRSCHMÜLLER & BUCHER (2010). This research leads to the assumption that point clouds derived by dense image matching and subsequent fusion techniques are characterized by very high accuracy – less than 1 GSD both horizontally and vertically. It opens a very broad field of potential applications for this data source.

ALS, often called lidar (light detection and ranging), was initially seen as a technology for height measurements of the terrain to generate high-resolution DTM. After its commercial implementation the vertical accuracy of lidar point cloud was mainly considered (SHAN & TOTH 2008). In later years, with the increasing density of point clouds provided by lidar, its potential use in the context of other applications was recognized. The issue of the planar accuracy of lidar data also became a subject of discussion because vertical and planar accuracy are interdependent – which is particularly important for more complex DTM in sloped parts of terrain (AGUILAR et al. 2010). High horizontal accuracy is crucial in studies associated with point cloud processing in-

cluding: feature extraction, i.e. 3D modelling of buildings, engineering objects, roads, railways or river embankments, obstruction surveys as well as the merging of different datasets. Lidar datasets are frequently collected in country-wide or regional projects to generate elevation products such as DTM, DSM and 3D buildings models. The example of such a national program is the Polish IT System of the Country's Protection against extreme hazards (ISOK) where much higher vertical than planimetric accuracy is noticed (KURCZYŃSKI & BAKUŁA 2013). This is the reason why further using of lidar datasets collected within ISOK is sometimes limited in tasks requiring high planimetric accuracy specified by other legal restrictions related to surveying techniques.

The solution is to develop a method that can increase the horizontal accuracy. This could also be of interest for the alignment of lidar and photogrammetric data for subsequent data fusion. The main scope of the presented research is to develop and analyze methods for the improvement of the planar accuracy of lidar data. In this context, a true orthophoto generated from a DSM based on SGM can be very helpful due to its higher point density and its high planar precision. The proposed techniques might be utilized for applications in which the use of lidar is essential, e.g. for the determination of ground points in vegetated areas, for mapping small entities such as power lines (JWA et al. 2009) or railways (MARMOL & MIKRUT 2013), where high penetration of vegetation and high vertical accuracy as provided by lidar as well as a high planimetric accuracy offered by images are required.

Modern technologies of 3D data collection acquire lidar point clouds with a relative accuracy of 2 cm – 3 cm (VOSSELMAN 2008). CSANYI & TOTH (2007) demonstrate that the use of specially designed targets may enable a similar level of absolute accuracy considering a dense point cloud of 16 points/m<sup>2</sup>. However, the large amount of manual interaction associated with the use of control targets as well as the need for their installation before the flight makes it an impractical solution (RAY & GRAHAM 2008). Having in mind these problems and limitations, in this paper two methods for the validation of lidar point clouds and their correction for local biases are proposed. In

contrast to the concept of using back-projection of laser points to images by the collinearity equation as proposed by SEO et al. (2001), in this article the use of independent measurements derived from a true orthophoto and their use for the assessment and improvement of the planimetric accuracy of lidar point clouds is examined. Images provide a very large number of features which may be measured for a reliable evaluation of the accuracy and the estimation of local planimetric corrections for lidar data. In particular, the key advantage of using a true orthophoto is the opportunity for the selection of reference measurements not only at the ground level, but also on building roofs. A true orthophoto is a metric data source providing valuable spatial and spectral information for various GIS and mapping applications (BANG et al. 2007, KOWALCZYK et al. 2010). On the other hand, it cannot be disregarded that creating true orthophotos requires serious efforts and costs. The production of true orthophotos is justified particularly in urban areas with densely located and high buildings. They provide a continuous visualization with the exception of obscured areas which still enables the selection of corresponding features for the registration of lidar and other data sources. True orthophotos can be used for quality assessment of lidar data, and they can even support the georeferencing of these data without additional ground control. In this paper, they are used to validate and to improve the planar accuracy of lidar point clouds.

Methods for registration of images might be divided into two main groups: feature-based and intensity-based techniques (GOSHTASBY 2012). In addition, HUI et al. (2012) proposed a frequency-based approach for the registration of lidar data and optical images.

With the ability to register the intensity of the reflected signal, studies on the reflectance image have been carried out (MAAS 2002). Although the intensity images look similar to optical images, they have different characteristics. In addition, the intensity images are usually much noisier, which was noticed by VOSSELMAN (2002). Despite the limitations indicated in his research, VOSSELMAN (2002) showed that it is possible to use edges obtained from lidar intensity data to determine the offsets between scanning strips. Another

proposal for using reflectance images to compensate for systematic errors in the alignment of lidar strips can be found in MAAS (2001). He proposed fitting the surface fragments in a TIN structure where, instead of elevation, the intensity value was applied. MAAS states that it is possible to determine planimetric discrepancies between scanning strips with the accuracy of  $\frac{1}{4}$  of the distance between points. The application of the intensity images as one of the observation types used to define boresight misalignment is proposed by BURMAN (2000). Another example is presented in TOTH et al. (2007), where intensity is used to improve the absolute planimetric accuracy of lidar data by matching corresponding pavement markings on roads generated from GNSS surveying measurements with the same features identified in the lidar reflectance image. Similarly, RAY & GRAHAM (2008) propose the digitalization of road markings in the orthoimage from lidar intensity and their usage in the absolute orientation improvement.

Many attempts have been made to co-register image and lidar data. Some of them use lidar data as a reference for image registration (HABIB et al. 2005, KWAK et al. 2006, MITISHITAA et al. 2008, CHOI et al. 2011, CHUNJING & GUANG 2012) while others consider the improvement of lidar data using photogrammetric images, e.g. ARMENAKIS et al. (2013). The character of lidar data makes it difficult to extract precise features that would enable for co-registration of image and lidar data. To overcome this limitation more complex features extracted from the point cloud, e.g. edges (CHUNJING & GUANG 2012, CHOI et al. 2011), centre points of buildings (AHOCAS et al. 2004), planes (ARMENAKIS et al. 2013) or centroids of planes (MITISHITAA et al. 2008, KWAK et al. 2006) have been used. Another possibility is to use features extracted from the intensity raster, e.g. points (TOTH et al. 2007, BURMAN 2000), lines (VOSSELMAN 2002, RAY & GRAHAM 2008). In this paper the authors propose to use methods based on two types of features that enable a precise horizontal survey, namely roof ridges extracted from point clouds and points extracted from raster images generated from the lidar reflection intensity.

The novelty of the methods presented in this paper is the use of a true orthophoto that

is a side-product of SGM, generated by an orthogonal projection of the coloured point cloud from SGM rather than by back-projection of points interpolated from a DSM into the images (MILLER 2004). Despite of many shortcomings (incompleteness of the coverage, distortions in shadowed and vegetated areas) it is worth emphasizing that such a true orthophoto can be obtained fully automatically as a side product of photogrammetric projects without significant additional costs. The authors claim that it is worthwhile to look for applications that take advantage of the accessibility and great potential of this product.

In the presented research we show empirically that such a true orthophoto is characterised by a very high absolute horizontal accuracy, which give rise to its application as a reference for the lidar point clouds. Two independent methods of validation and correction of lidar horizontal accuracy are presented based on photogrammetric data source. Similar results obtained from both methods show that using true orthophotos generated as a side-product of SGM allows for the detection and correction of local lidar biases.

This paper is structured as follows. First we present the proposed methodology for validation and improvement of the planimetric accuracy of lidar data based on the calculation of the local (sub-block) error. The first method is based on manual measurement of points on the lidar intensity images and a true orthophoto. The second method is based on the distances between ridges generated automatically from lidar data and ridge lines extracted from the true orthophoto. After the description of these methods an experimental area is presented. The results obtained from both methods are compared to draw conclusions concerning the possibility of using true orthophotos from dense matching in the assessment and correction of the horizontal accuracy of lidar data. Future developments of the presented methods with the ultimate aim of a higher degree of automation are outlined in section 5.

## 2 Methodology

### 2.1 The Intensity-Based Approach

The first method proposed in this paper was to measure planimetric discrepancies between homologous points on the true orthophoto and lidar intensity image. The points were usually selected as distinct points in the lidar intensity image, because of its lower spatial resolution and the noise they are affected with (MAAS 2001). After that, they were also measured in the true orthophoto. The most frequently selected point types were associated with centres of white road markings, manhole covers and centres of visible small patterns on pavements surface because of their high contrast in the intensity images with respect to surrounding objects. Furthermore, they are expected to be less biased than the ends of linear objects or edges of surface objects.

Considering the methodology for the georeferencing of a lidar block, the accuracy is not constant over the area and can vary locally. Therefore, the local fragments (sub-blocks) are created to adapt best to local errors and help to minimize the overall error budget. The errors for X and Y co-ordinates are analyzed separately in the proposed approach by the estimation of appropriate corrections for both directions. The correction model is a simple shift, determined independently for each sub-block requiring an improvement of planar accuracy. Potential discontinuities at the sub-block boundaries can be limited by using overlapping sub-blocks. The values of potential planimetric corrections (1) are computed as the negative median value of the horizontal displacement for the whole test area:

$$\begin{aligned} v_x &= -\text{Median}(D(x)) \\ v_y &= -\text{Median}(D(y)) \end{aligned} \quad (1)$$

where

$D(x)$ ,  $D(y)$  are measured displacements between homologous points,

$v_x$ ,  $v_y$  are estimated corrections.

The estimated planar correction can be implemented locally. The aim of such a procedure is to obtain a limited area (sub-block) with augmented horizontal accuracy.

## 2.2 The Feature-Based Approach

The second method evaluated in this study was based on normal distances between the ridge lines of buildings which can be extracted from the lidar dataset automatically and digitalized on the true orthophoto to estimate the planimetric displacement. Ridge lines of gable roofs, obtained as the intersection lines of two planes fitted into the point cloud, are one of most accurate features extracted from lidar data and they can be used to improve the relative planimetric accuracy of the point clouds (VOSSELMAN 2008).

Automatic classification of point clouds and building roof extraction was performed using the TerraSolid software. Building models are generated by the TerraScan module, which is based on an algorithm for fitting planes to parts of point cloud classified as ‘buildings’, combining these planes in order to create roof models (SOININEN 2014).

Ridge lines of all detected buildings are also measured manually in the true orthophoto. In contrast to VOSSELMAN (2012), who measured the distance between centres of ridges, the displacement between the corresponding roof ridges from both data sources was calculated as the distance from the middle point of a ridge line on the true orthophoto in the normal direction, i.e. perpendicular to the direction of the ridge line from the true orthophoto. In the case of two ridges from the lidar data, it can be assumed that they are equal in length. However, in the case of ridges from different data sources, their lengths might not be identical. This may result in problems associated with determining the start and the end of the line and, consequently, centre point. Nevertheless, the directions of the ridges from both of these data sources are maintained. They should be approximately parallel and the normal displacement vector between pairs of ridge lines from two sources should indicate the magnitude of planimetric error of lidar data in this particular direction.

The polar coordinates of a local displacement vector were estimated by a least-squares adjustment in order to minimize the squared sum of the normal distances between the corresponding ridge lines after applying the dis-

placement vector. The objective function (2) was defined as:

$$\min \sum_i (D \cdot \cos(\Phi - \varphi_i) - d_i)^2, \quad (2)$$

where

$d_i$  is the observed length of the normal displacement vector between a pair of ridges,

$\varphi_i$  is the observed polar angle of the normal displacement vector between a pair of ridges,

$D$  is the unknown length of the local displacement vector and

$\Phi$  is the unknown polar angle of the local displacement vector.

The estimated corrections ( $v_x, v_y$ ) were calculated as follows:

$$\begin{aligned} v_x &= -D \cdot \cos \Phi \\ v_y &= -D \cdot \sin \Phi \end{aligned} \quad (3)$$

The proposed method for the implementation estimated correction in this approach can be applied the same way as in the first approach – as simple shift for both directions.

## 3 Experiments

### 3.1 Data used in this Study

In the presented research, aerial images and lidar data were used. Such datasets were collected in flight missions involving the whole city of Elbląg (about 100 km<sup>2</sup>). Both flight missions were conducted in March 2011 before the vegetation period with an interval of three weeks. As a test area for the experiments a fragment of the block (approximately 0.5 km<sup>2</sup>) with densely located buildings was selected.

Aerial images were acquired with an Intergraph DMC II 230 camera with 80% overlap, 40% side lap and a GSD of 5 cm. A block of 2.243 images was triangulated with the use of 86 GCPs. The obtained accuracies estimated by comparison of object coordinates to 96 check points were as follows: RMSE of 2.9 cm (Easting), 3.8 cm (Northing), 4.5 cm (Z). On the basis of the adjusted image block, point clouds were generated using the modified ver-

sion of SGM that is implemented in the SURE software (ROTHERMEL et al. 2012). Such point clouds with assigned RGB values from images were subsequently used to create raster images of point clouds in an orthogonal view, providing a true orthophoto without much effort and cost requirements.

These images were used to create a true orthophoto mosaic of the test area with a spatial resolution of 7 cm. The absolute accuracy of such a true orthophoto was verified because it is used as the reference for further research concerning planimetric accuracy. We determined 21 check points located in the test area using real time kinematic global navigation satellite system (RTK GNSS). The differences between the coordinates were manually measured on the true orthophoto and the surveying observations determined the accuracy characteristics of the true orthophoto. Based on the results presented in Tab. 1, it can be concluded that the true orthophoto shows no bias and the RMSE is 3 cm – 4 cm which is comparable with the accuracy of RTK GNSS measurements. This shows that the true orthophoto is a product of high planimetric accuracy and can be used as reference data for the assessment of the horizontal error in the lidar data.

**Tab. 1:** Accuracy characteristics of the true orthophoto.

Parameter	X (Easting) (m)	Y (Northing) (m)
Average residual	-0.001	0.014
RMSE	0.038	0.034
Std	0.038	0.031

Lidar data was acquired with a Riegl LMS-Q680i airborne laser scanner with 60% side-lap between scanning strips. A total of 70 strips were acquired. The average density of the point cloud in a single scanning strip was approximately 10 points/m<sup>2</sup>. The data were subjected to a process of internal, relative alignment and fitted to reference planes surveyed in situ. This process was carried out using the RiProcess software, which is applied to raw lidar data acquired by Riegl scanners. The roofs of the buildings in 5 locations were used as reference planes. In each location two roof planes oriented perpendicularly to each other were surveyed. The relative alignment of the block was carried out using 117,875 observations on the tie planes – as a result, the



**Fig. 1:** Spatial distribution of points manually measured on the intensity image and the true orthophoto overlaid with the presentation of the scanning strips edges.

correction for each scanning strip trajectories was made. After this process, the whole lidar block was fitted to the previously mentioned reference planes and the residuals indicate a global shift of 4.4 cm (X), 6.0 cm (Y) and 2.8 cm (Z) for the whole block. After the adjustment, the RMSE calculated from normal distances to the reference planes was 4.2 cm with the highest residual value of 8.8 cm. As a result of the described procedure the whole lidar block is best fitted into the reference planes by applying a global correction. However, the remaining residuals on the reference planes show that the georeferencing accuracy varies in different regions of the block. Therefore, we can still expect local errors at a level of a few centimetres.

In the presented research, fragments of three scanning strips were selected and intensity images with 15 cm GSD were prepared. Each of the intensity images was created by assigning the average intensity value to each pixel. The average intensity value scaled to the 8-bit greyscale of all lidar points was located inside this pixel. The intensity values for pixels with no points in its range were determined by bilinear interpolation.

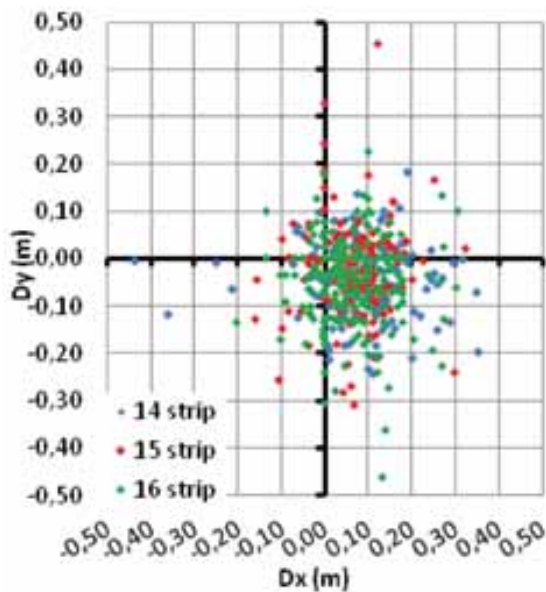


**Fig. 2:** Planimetric residuals of points measured on the intensity raster in reference to their location on the true orthophoto for 3 analysed scanning strips in the intensity-based approach.

### 3.2 Results of the Intensity-Based Approach

After the georeferencing procedure the intensity-based approach is applied. Though its accuracy is minor it helps to compensate local errors because the global approach is only based on a limited number of surveyed planes. The spatial distribution of observations in this approach is shown in Fig. 1. The results of the measurements on the intensity raster (planimetric displacement for each point) for single scanning strips are presented in Fig. 2. Measurements were carried out for 550 points totally in three strips: 150 points were measured in strip 14, 150 in strip 15 and 250 in strip 16.

In Fig. 2, significant shifts in the X direction for all strips are clearly visible. This is also confirmed by statistical parameters (Tab. 2). The final correction caused by shift parameters obtained in this method were calculated as -0.07 m in X direction and +0.04 m in Y direction.

Due to the large number of outliers which were expected in manual measurement, the

**Tab. 2:** The result of corresponding points measurements on ALS intensity image and true orthophoto for planar shift estimation.

Strip	Parameter	X (m)	Y (m)
14	mean	0.09	-0.05
	median	0.10	-0.05
	Std	0.11	0.08
150 points	RMSE	0.14	0.09
15	mean	0.07	-0.02
	median	0.07	-0.01
	Std	0.08	0.10
150 points	RMSE	0.10	0.11
16	mean	0.06	-0.05
	median	0.07	-0.05
	Std	0.08	0.09
250 points	RMSE	0.08	0.08
all 3 strips	mean	0.07	-0.04
	median	<b>0.07</b>	<b>-0.04</b>
	Std	0.09	0.09
550 points	RMSE	0.11	0.10

corrections were computed based on the median value instead the mean value. The measured points and the results were evaluated by the standard deviation of the observations (Std) and the root-mean-square error (RMSE) for the assessment of the planimetric accuracy of the lidar data.

In this paper we just want to show that such a method is possible for the error estimation without caring whether the measurement process is manual or automatic. Nevertheless, in these studies the automation of measurements was also attempted (Fig. 3), but it was associated with many difficulties caused by different geometry and radiometry of the images from different sources. Such activity which can lead to the synergy of lidar with optical imagery can be very sophisticated and it is still a big challenge (HUI et al. 2012). These datasets are derived from a different source and differ-

ent flight missions. Consequently, they have a different distribution of occluded areas. Shadows are another problem that can be observed in optical images. In addition, the spectral characteristics of the reflectance in the visible and the near-infrared spectrum and of lidar reflected intensity are different. This is especially evident for the vegetation. When analysing true orthophotos in the near-infrared spectrum, vegetation is characterised by high radiometric values. In contrast, because of the low value of reflection of the laser beam, trees are represented by low radiometric values on the intensity raster images. These problems hinder the automation of the measurement of corresponding points with area-based matching methods. In order to solve this problem only regions without occluded areas (intensity raster) and no shadows (true orthophoto) were analysed. It was therefore decided to analyze only fragments of roads without any difficulties related to distinguishable radiometry differences of the two data sources. Small pieces of true orthophoto and intensity raster were subjected to a least-square matching procedure. The experiments performed led to some interesting results (Fig. 3). The majority of automatically selected points was related to road markings as the most contrasting features in intensity raster. The experiment showed that there is the potential to enable automation of the proposed method. However, the above-mentioned problems related to co-registration of a whole sub-block led the authors to only use manually measured points, as they were considered reliable enough for the assessment of the lidar horizontal error estimation.

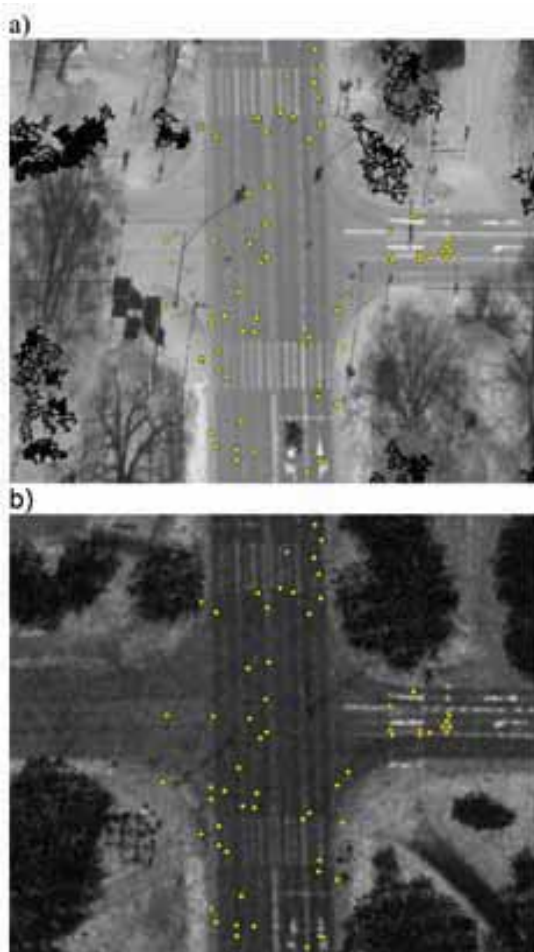


**Fig. 3:** Example of automatically generated corresponding points from image matching between true orthophoto (a) and raster of reflectance intensity (b).

### 3.3 Results of the Feature-Based Approach

For the experiments reported in this section a total number of 321 building models were used. Fig. 4 shows the distribution of the extracted ridge lines in the test area. The detailed view depicts automatically extracted building models based on lidar data. The background represents the true orthophoto generated by dense image matching. We determined 126 ridge lines from strip number 14, 130 from strip 15 and 67 from strip 16. The estimation of the er-



**Fig. 4:** An overview of all ridge lines extracted from true orthophoto in the test area and a detailed view presenting automatically lidar-extracted building models with true orthophoto from dense image matching in a background.

ror was performed individually for each of the scanning strips and also for all scanning strips together in order to characterize the planimetric error in the whole sub-block. Fig. 5 shows the values of the offset vectors between ridges digitized on the true orthophoto and those obtained from the 3D building models from the ALS data. It is worth noting that the concentration of points along the X-axis and Y-axis is caused by the orientation of roof surfaces in the test area. Points located around the X-axis are related to ridges oriented in the N-S direction and they have significant influence in determining the error in the X direction. On the other hand, points around the Y-axis are associated with ridges oriented in the E-W direction and they have a key impact on the estimation of the error in the Y direction.

In this method shift values were computed using the least-squares method. The results are presented in Tab. 3. The displacement estimat-

ed from ridge lines is similar to those measured on the intensity images (Tab. 2). In all three strips, the errors determined are compa-

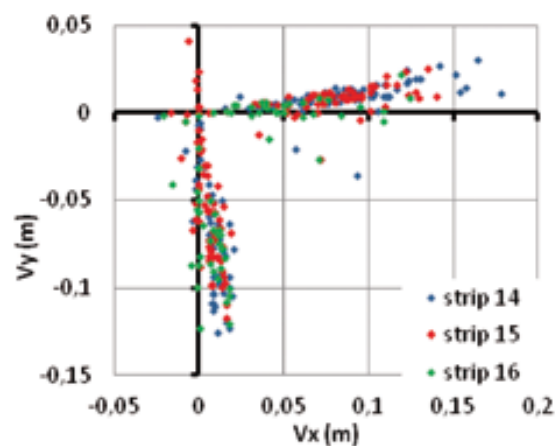


**Fig. 5:** Offset vectors between ridges digitized from the true orthophoto and those obtained from 3D building models from lidar data in feature-based approach.

**Tab. 3:** Horizontal shifts and their accuracy characteristics obtained from the measurements of roof ridges on the true orthophoto and from 3D building models.

Strip	Parameter	X (m)	Y (m)
14 126 ridges	Shift	0.09	-0.06
	Std	0.04	0.03
	RMSE	0.10	0.07
15 130 ridges	Shift	0.08	-0.05
	Std	0.05	0.03
	RMSE	0.09	0.06
16 67 ridges	Shift	0.05	-0.07
	Std	0.03	0.04
	RMSE	0.06	0.08
all 3 strips 323 ridges	Shift	<b>0.08</b>	<b>-0.06</b>
	Std	0.04	0.03
	RMSE	0.09	0.07

rable. Only results for scanning strip 16 differ slightly from the others, which can be caused by a lower number of ridges measured in this strip due to the topography of the selected urban area. The key point of the analysis of this approach is the fact that values of the standard deviations are much lower than with the previous method. The final corrections caused by shift parameters obtained in this approach were -0.08 m in X and +0.06 m in Y.

#### 4 Discussion

Both of the methods resulted in similar values of planimetric error for the analyzed area. Lower standard deviations in the feature-based approach indicate that the usage of measured roof ridges of buildings was more reliable. However, this method is more labour-intensive and difficult to automate. It is worth mentioning that both methods have some limitations. First of all, a suitable topography of the area is required. For the feature-based approach, an appropriate number of roof ridges oriented in different directions must be provided. The application of points measured on the intensity image in the first method requires

clearly defined features in both images. Consequently, there is no doubt that both methods are best suited for urban areas.

The results for both, the whole test object and individual strips, are quite comparable in the two presented methods, which confirm the correctness of both approaches as well as the possibility of the planimetric error detection in the sub-blocks on the basis of true orthophoto. Such data fitting approaches (similarly to VOSSELMAN 2008, 2012), without considering the rotation parameters correlated locally with the displacement are the least complicated methods for large-scale applications due to many factors that influence the lidar accuracy. The presented methodology shows that it is possible to determine the errors whose value is much lower than the point spacing in lidar datasets. The results are in accordance with the authors' expectations and some small differences between the estimations for separate strips can also be related to the accuracy of their relative alignment.

The results of point measurements are characterized by a visible, large dispersion of residual values. Manually measured points were difficult to identify in the intensity images, a fact that is also mentioned by RAY & GRAHAM (2008). However, the investigation carried out in this research indicates that in the case of good quality data, it is possible to select many corresponding points and the redundancy allows finding the expected value of the planimetric shift of ALS data, limiting the influence of gross errors. Nevertheless, the approach based only on manual measurements is time-consuming for the whole block error estimation, because different planar errors can be expected for various parts of the block. On the other hand, this paper shows the potential of this type of analysis. In such approaches it is very important to have a large contribution of automation in the matching of corresponding points (BURMAN 2000, MAAS 2002) which is, however, related to the problems previously mentioned. In contrast to other publications considering the analyzed subject, the detected errors are relatively small, which is caused by the increasingly higher quality of modern photogrammetric data characterized by a very small GSD (aerial images) and high density of the lidar point clouds.

In this study the intensity of laser beam reflection was applied to determine the absolute accuracy of ALS data with the product of aerial image processing (orthoimages) as a reference, while in the literature it is more likely to find approaches using the intensity images for analyzing only the relative lidar data orientation (BURMAN 2000, MAAS 2002). The presented research differs from some other methods regarding the absolute accuracy (CSANYI & TOTH 2007), because in contrast to those approaches, it is not based on control targets. This is particularly important when considering lidar data already acquired and archived in repositories. There are usually no control targets for such data because the main objective of their acquisition was not necessarily very high planimetric accuracy.

The presented research has shown that the use of a true orthophoto that is a side-product of SGM can allow for the enhancement of horizontal accuracy of lidar data. The application of this type of imagery has a considerable potential for the automation which would allow obtaining lidar data with an augmented horizontal accuracy in urban areas and hence the possibility of integration with other image data and GIS databases.

## 5 Conclusion

Using a true orthophoto with high planimetric accuracy as a reference, the presented methods allow for the calculation of the planimetric displacement of lidar data. It can correct it to a level that enables wider utilization of lidar data for applications which require a horizontal accuracy of a few centimetres. The determined systematic error can be corrected by the implementation of an appropriate correction to the point cloud or products of its processing. The basic condition of a successful application of the proposed methods is the high redundancy of the measurements. At present, this requirement is fulfilled by manual measurements which become inefficient for large areas. The effectiveness of the methods for such correction can be only guaranteed by automatic techniques of corresponding features matching (points, lines). The application of intensity-based matching algorithms, with

true orthophoto as a reference can be difficult due to the different characteristics of both data sources.

Future work should focus on larger and less fallible automatic techniques for the planimetric comparison and bias estimation of lidar by matching of orthophotos from aerial images and intensity of laser reflectance. It is expected that such automation is achievable in feature-based approaches based on true orthophotos. However the subject of horizontal accuracy, which is sometimes omitted, is still not exhausted assuming that it does not have to be limited to investigations in 2D. These analyses could also involve 3D features: ridge lines and even entire roof planes which can provide both vertical and planar discrepancies. Future activities in this work should also consider the evaluation of such methodologies as well as the assessment of intensity images or building ridge potential in improving the horizontal accuracy of lower quality lidar data that are usually available for large areas. The presented approach could then be used for the data already acquired in country-wide or regional systems for applications requiring high planimetric accuracy.

## Acknowledgements

The presented research was financed by statutory subsidies of the Polish Ministry of Science and Higher Education for WUT. The authors would like also to thank OPEGIEKA Sp. z o.o. for the permission of use of data collected in own projects of this company.

## References

- AGUILAR, J., MILLS, J.P., DELGADO, J., AGUILAR, M.A., NEGREIROS, J.G. & PÉREZ, J., 2010: Modelling vertical error in LiDAR-derived digital elevation models. – *ISPRS Journal of Photogrammetry and Remote Sensing* **65**: 103–110.
- AHOKAS, E., KAARTINEN, H. & HYYPPÄ, J., 2004: A quality assessment of repeated airborne laser scanner observations. – *ISPRS-International Archives of the Photogrammetry, Remote Sensing and Spatial Information Sciences* **35**: 237–242.
- ARMENAKIS, C., GAO, Y. & SOHN, G., 2013: Co-registration of aerial photogrammetric and LiDAR

- point clouds in urban environments using automatic plane correspondence. – *Applied Geomatics* **5** (2): 155–166.
- BANG, K.I., HABIB, A., KIM, C. & SHIN, S., 2007: Comparative analysis of alternative methodologies for true ortho-photo generation from high resolution satellite imagery. – *ASPRS Annual Conference*, Tampa, FL, USA.
- BEGER, R., GEDRANGE, C., HECHT, R. & NEUBERT, M., 2011: Data fusion of extremely high resolution aerial imagery and LiDAR data for automated railroad centre line reconstruction. – *ISPRS Journal of Photogrammetry and Remote Sensing* **66** (6): 40–51.
- BERALDIN, J.-A., BLAIS, F. & LOHR, W., 2010: Laser scanning technology. – *VOSSELMAN, G. & MAAS, H.-G. (eds.): Airborne and Terrestrial Laser Scanning*: 1–42.
- BURMAN, H., 2000: Adjustment of laser scanner data for correction of orientation errors. – *International Archives of Photogrammetry and Remote Sensing* **33**: 119–126.
- CHOI, K., HONG, J. & LEE, I., 2011: Precise Geometric Registration of Aerial Imagery and LIDAR Data. – *ETRI Journal* **33** (4): 506–516.
- CHUNJING, Y. & GUANG, G., 2012: The Direct Registration of LIDAR Point Clouds and High Resolution Image Based on Linear Feature by Introducing an Unknown Parameter. – *ISPRS-International Archives of the Photogrammetry, Remote Sensing and Spatial Information Sciences* **1**: 403–408.
- CSANYI, N. & TOTH, C.K., 2007: Improvement of Lidar Data Accuracy Using Lidar-Specific Ground Targets. – *Photogrammetric Engineering & Remote Sensing* **73** (4): 385–396.
- GERKE, M. & XIAO, J., 2014: Fusion of airborne laserscanning point clouds and images for supervised and unsupervised scene classification. – *ISPRS Journal of Photogrammetry and Remote Sensing* **87**: 78–92.
- GOSHTASBY, A.A., 2012: *Image registration: principles, tools and methods*. – Springer-Verlag, New York, NY, USA.
- HABIB, A., GHANMA, M., MORGAN, M.F. & AL-RUZOUQ, R.E., 2005: Photogrammetric and LiDAR data registration using linear features. – *Photogrammetric Engineering and Remote Sensing* **71** (6): 699–707.
- HIRSCHMÜLLER, H., 2008: Stereo Processing by Semiglobal Matching and Mutual Information. – *IEEE Transactions on Pattern Analysis and Machine Intelligence* **30**: 328–341.
- HIRSCHMÜLLER, H. & BUCHER, T., 2010: Evaluation of Digital Surface Models by Semi-Global Matching. – *DGPF*, July 2010, Vienna, Austria.
- HUI, J., TOTH, C. & GREJNER-BRZEZINSKA, D.A., 2012: A New Approach to Robust LiDAR/Optical Imagery Registration. – *PGF – Photogrammetrie, Fernerkundung, Geoinformation* **5**: 523–534.
- JWA, Y., SOHN, G. & KIM, H.B., 2009: Automatic 3D powerline reconstruction using airborne LIDAR data. – *International Archives of Photogrammetry and Remote Sensing* **38**: 105–110.
- KOWALCZYK, M., PODLASIAK, P., PREUSS, R. & ZAWIESKA, D., 2010: Evaluation of cartometric properties of true-ortho images. – *Archive of Photogrammetry, Cartography and Remote Sensing* **21**: 191–200.
- KURCZYŃSKI, Z. & BAKUŁA, K., 2013: The selection of aerial laser scanning parameters for country-wide digital elevation model creation. – *13th SGEM Geoconference on Informatics, Geoinformatics and Remote Sensing* **2**: 695–702.
- KWAK, T.S., KIM, Y.I., YU, K.Y. & LEE, B.K., 2006: Registration of aerial imagery and aerial LiDAR data using centroids of plane roof surfaces as control information. – *KSCE Journal of Civil Engineering* **10** (5): 365–370.
- MAAS, H.-G., 2001: On the Use of Pulse Reflectance Data for Laserscanner Strip Adjustment. – *International Archives of Photogrammetry and Remote Sensing* **34**: 53–56.
- MAAS, H.-G., 2002: Methods for Measuring Height and Planimetry Discrepancies in Airborne Laserscanner Data. – *Photogrammetric Engineering & Remote Sensing* **68** (9): 933–940.
- MARMOL, U. & MIKRUT, S., 2013: Attempts at Automatic Detection of Railway Head Edges from Images and Laser Data. – *Image Processing & Communications* **17** (4): 151–160.
- MILLER, S., 2004: *Photogrammetric Products*. – *McGLONE, J.C., MIKHAIL, E.M. & BETHEL, J. (eds.): Manual of Photogrammetry*, 5th ed., American Society of Photogrammetry and Remote Sensing, Bethesda, MD, USA: 983–1014.
- MITISHITAA, E., HABIB, A. & MACHADOA, A., 2008: Photogrammetric model orientation using LiDAR dataset. – *International Archives of Photogrammetry and Remote Sensing* **37**: 167–172.
- PARK, H., SALAH, M. & LIM, S., 2011: Accuracy of 3D models derived from aerial laser scanning and aerial ortho-imagery. – *Survey Review* **43** (320): 109–122.
- PARMEHR, E.G., FRASER, C.S., ZHANG, C. & LEACH, J., 2013: Automatic registration of optical imagery with 3D LIDAR data using local combined mutual information. – *ISPRS Annals of the Photogrammetry, Remote Sensing and Spatial Information Sciences* **II-5/W2**: 229–234.

- RAY, J.A. & GRAHAM, L., 2008: New Horizontal Accuracy Assessment Tools and Techniques for Lidar Data. – ASPRS Annual Conference, Portland, OR, USA.
- ROTHERMEL, M. & HAALA, N., 2011: Potential of Dense Matching for the Generation of High Quality Digital Elevation Models. – ISPRS Hannover Workshop 2011: High-Resolution Earth Imaging for Geospatial Information, IASPRS XXXVIII-4/W19.
- ROTHERMEL, M., WENZEL, K., FRITSCH, D. & HAALA, N., 2012: SURE: Photogrammetric Surface Reconstruction from Imagery. – LC3D Workshop, Berlin.
- SEO, S., SCHENK, T. & CSATHO, B., 2001: Accuracy study of airborne laser scanning data with photogrammetry. – International Archives of Photogrammetry and Remote Sensing **34**: 113–118.
- SHAN, J. & TOTH, C. (eds.), 2008: Topographic Laser Ranging and Scanning: Principles and Processing. – CRC Press, Taylor & Francis Group.
- SOININEN, A., 2014: TerraScan User's Guide. – <https://www.terrasolid.com/download/tscan.pdf> (11.9.2014), 485 p.
- TOTH, C., PASKA, E. & GREJNER-BRZEZINSKA, D.A., 2007: Using Pavement Markings to Support the QA/QC of LIDAR Data. – International Archives of Photogrammetry, Remote Sensing and Spatial Information Sciences **36**: 173–178.
- VOSSELMAN, G., 2002: On the Estimation of Planimetric Offsets in Laser Altimetry Data. – International Archives of Photogrammetry, Remote Sensing and Spatial Information Sciences **34**: 375–380.
- VOSSELMAN, G., 2008: Analysis of planimetric accuracy of airborne laser scanning surveys. – International Archives of Photogrammetry, Remote Sensing and Spatial Information Sciences **37**: 99–104.
- VOSSELMAN, G., 2012: Automated planimetric quality control in high accuracy airborne laser scanning surveys. – ISPRS Journal of Photogrammetry and Remote Sensing **74**: 90–100.

Address of the Authors:

KRZYSZTOF BAKULA, WOJCIECH DOMINIK & WOJCIECH OSTROWSKI, Warsaw University of Technology, Faculty of Geodesy and Cartography, Plac Politechniki 1, PL 00-661 Warsaw, Poland, Tel. +48-22-234-76-94, e-mail: {k.bakula}{w.ostrowski}@gik.pw.edu.pl, wojciech.a.dominik@gmail.com

Manuskript eingereicht: Februar 2014

Angenommen: Januar 2015





# Development of Multi-Temporal Landslide Inventory Information System for Southern Kyrgyzstan Using GIS and Satellite Remote Sensing

DARYA GOLOVKO, SIGRID ROESSNER, ROBERT BEHLING, HANS-ULRICH WETZEL, Potsdam & BIRGIT KLEINSCHMIT, Berlin

**Keywords:** landslide inventory, landslides in Kyrgyzstan, GIS-based data integration

**Summary:** In Southern Kyrgyzstan, landslides regularly endanger human lives and infrastructure. They are a very dynamic phenomenon with significant variations of the process activity in different years. This creates a need for the development of new methods of dynamic and spatially differentiated landslide hazard assessment at a regional scale. Because of the large size of the study area (over 12,000 km<sup>2</sup>), remote sensing data are a valuable and reliable source of detailed and consistent spatial information for landslide investigations in Southern Kyrgyzstan. The paper demonstrates how GIS and remote sensing techniques are used for the acquisition, verification and homogenization of heterogeneous multi-source landslide data with the goal of generating a multi-temporal landslide inventory. Special emphasis is placed on the spatial data consistency, the documentation of temporal information and the possibility to document repeated slope failures within the same slope. The multi-temporal landslide inventory is an integral part of a landslide inventory information system, which is implemented in the QGIS environment and provides self-customized functionality for data queries and spatial analysis including the derivation of landslide attributes. The information system contains additional spatial base data such as a spatially consistent multi-temporal archive of satellite images and topographic maps.

**Zusammenfassung:** *Entwicklung eines Informationssystems zur multitemporalen Inventarisierung von Hangrutschungen für Südkirgistan unter Verwendung von GIS und Satellitenfernerkundung.* In Südkirgistan werden durch Hangrutschungsereignisse regelmäßig Menschenleben sowie technische und soziale Infrastruktur gefährdet. Da die Hangrutschungsaktivität in dieser Region zwischen den Jahren sehr variiert, besteht der dringende Bedarf, Methoden zu entwickeln, welche eine dynamische und räumlich differenzierte Einschätzung der Hangrutschungsgefährdung auf regionaler Ebene erlauben. Aufgrund der Größe des Untersuchungsgebietes von über 12.000 km<sup>2</sup> sind für die Entwicklung dieser Methoden satellitengestützte Fernerkundungsdaten besonders geeignet, da sie die einzige räumlich kontinuierliche und zeitlich wiederholbare Informationsbasis für die gesamte Region darstellen. In diesem Paper wird gezeigt, wie GIS- und Fernerkundungsverfahren für die Erfassung, Überprüfung und Homogenisierung heterogener Hangrutschungsdaten aus mehreren Quellen verwendet werden, um eine multitemporale Inventarisierung von Hangrutschungen zu ermöglichen. Besonderer Wert wird dabei auf die räumliche Konsistenz der Daten, die Dokumentation des zeitlichen Auftretens und die Erfassung von wiederholten Hangrutschungsereignissen innerhalb desselben Hangs gelegt. Um die multitemporale Hangrutschungsinventarisierung zu unterstützen, ist ein QGIS-basiertes Informationssystem entwickelt worden, welches mit angepassten Datenabfragen und räumlichen Analysen zur Ableitung von Hangrutschungsattributen beiträgt. Das Informationssystem beinhaltet zusätzliche Geobasisdaten wie ein räumlich konsistentes multitemporales Archiv von Satellitenbildern und topographische Karten.

## 1 Introduction

The foothills of the Tien Shan mountain ranges along the eastern rim of the Fergana basin in Southern Kyrgyzstan are subject to high landslide activity as a result of pronounced relief and ongoing tectonic activity. Furthermore, the topographically rising eastern rim of the Fergana basin represents a barrier to the prevailing westerlies leading to increased precipitation levels in comparison to areas that are situated further east (KALMETYEVA et al. 2009). All of these factors create favourable conditions for the intense and frequent occurrence of landslides in this area of about 12,000 km<sup>2</sup> administratively covering the Osh and Dzhallal-Abad provinces (oblasts), presenting an important human living space in this mountainous country (Fig. 1). Large landslides occur mostly within weakly consolidated Mesozoic and Cenozoic sediments at elevations between 800 m and 2,000 m a.s.l. Slope failures in massive Quaternary loess sediments are especially dangerous due to their very rapid and destructive avalanche-like movement. Another type of landslides develops in more clay-

rich sediments and is characterized by lower movement rates but can nevertheless affect large areas (ROESSNER et al. 2014, ROESSNER et al. 2005, WETZEL et al. 2000). Since landslides represent a major threat to the local population frequently causing fatalities and severe economic losses, observations of landslide activity in Southern Kyrgyzstan have been carried out by local organizations since the 1950s. Between 1969 and 2010, approximately 4,500 landslides were recorded in Southern Kyrgyzstan (IBATULIN 2011). Since 1993, over 250 persons have died as a result of catastrophic slope failures in Kyrgyzstan (TORGONEV et al. 2010). Landslide activity in this region is characterized by frequent and at the same time sporadic occurrence of events. This creates a strong need for a spatially differentiated assessment of landslide hazard and risk.

A landslide inventory is one of the main prerequisites for an objective landslide hazard assessment, which includes both the spatial and the temporal aspects of the probability of landslide occurrence (GUZZETTI et al. 2005). A landslide inventory is a register of the distribution of landslides and their characteristics (HERVÁS

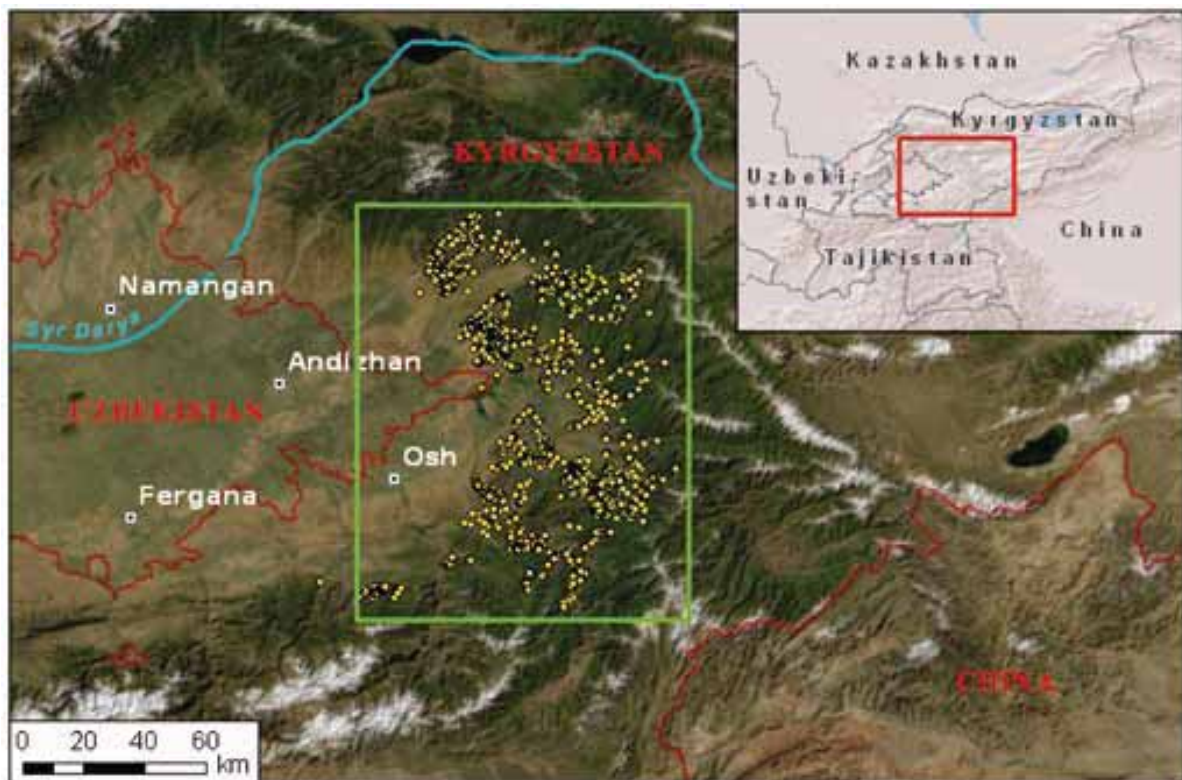


**Fig. 1:** Study area in Southern Kyrgyzstan (green) with landslide locations (yellow) according to data obtained from YEROKHIN (1999). Spatial base data from Esri.

2013, GUZZETTI et al. 2012). The latter usually include the landslide id, location, dates of first occurrence and reactivations, type, state of activity, area and volume. Additionally, information on landslide geometry, geo-environmental characteristics at landslide site, triggering factors, landslide impact, monitoring data, etc. can be incorporated. The set of recorded characteristics may differ depending on the scale and method used to create the inventory, on properties of the study area as well as on the project goals. An overview of the most common landslide attributes is presented in Tab. 1.

A wide range of methods have been developed in order to generate landslide inventories discussed in VAN WESTEN et al. (2008) and GUZZETTI et al. (2012). These methods include visual and (semi-) automated interpretation of optical, lidar and radar remote sensing data, geomorphological field mapping and archive studies. Geomorphological field mapping and visual interpretation allow integrating expert knowledge on the geological set-

ting in the region into the mapping process but these methods are prone to subjectivity and are only suitable for mapping areas of limited size. Visual interpretation of optical aerial and satellite images, sometimes combined with a DEM, remains a widely used technique for landslide mapping. In the recent years, approaches have been developed for automated and semi-automated landslide detection from high-resolution multi-spectral satellite images based on the classification of a single image or combined analysis of pre-event and post-event images. These approaches can be pixel-based or object-based. Whereas optical remote sensing enables the detection of slope failures that have already occurred, InSAR techniques allow detecting small surface deformations. In case of landslides, these deformations mainly indicate reactivations of previously active slopes that precede a new failure (MOTAGH et al. 2013, WASOWSKI & BOVENGA 2014). Overall, applications of satellite remote sensing for landslide mapping have become more im-

**Tab. 1:** Overview of landslide attributes: ‘++’ = ‘very suitable’, ‘+’ = ‘suitable’, ‘-’ = ‘unsuitable’ (after VAN DEN ECKHAUT & HERVÁS 2012, WP/WLI 1993, USGS 2004, HERVÁS 2013, WIECZOREK 1984).

Attribute Group	Selected Attributes	Methods for Derivation		
		Terrestrial	Map / GIS	Remote Sensing
General information	ID, reporter, photographs, bibliography	-	-	-
Landslide location	Coordinates, reference to river valley or settlements, administrative units	++	++	+
Landslide dimensions	Length / width / depth at head / middle / toe part	+	++	++
	Volume	++	-	-
	Area, perimeter / area ratio	+	++	+
	Elevation drop	+	+	++
Landslide classification	Type of movement (e.g. flow, rotational or translational slide), slope material (e.g. rock / debris / mud flow)	++	+	+
Geo-environmental characteristics	Relief: slope, aspect, curvature and derivatives	+	-	++
	Lithology, tectonic structures, land use, distance to roads	++	++	+
Landslide history and activity	Known failure and reactivation dates, state of activity (e.g. active / dormant / relict landslide)	++	+	++
Causes	Hydrometeorological, seismic and other conditions preceding the failure	++	-	+
Consequences and elements at risk	Fatalities and injuries	-	-	-
	Building damages, road closures, loss of arable land, number of people and buildings at risk	++	++	+

portant in the last decade due to the substantial increase in the satellite data availability, their spatial resolution and the development of hardware and software for image processing. The ongoing nature of satellite data acquisition permits going beyond producing a single landslide inventory map towards an information system with capabilities for future data updates as indicated by VAN WESTEN et al. (2006). Such dynamic landslide inventories can serve as the basis for improved landslide hazard assessment that can incorporate input data updates and be carried out repeatedly, e.g. upon the availability of new data. GIS tools can be used for an efficient derivation of many of the landslide attributes from vector and raster data (Tab. 1).

Objective landslide hazard assessment for the study area requires a systematic landslide record in form of a multi-temporal landslide inventory, which documents slope failures over a long period of time including the dates or periods of their occurrence. The goal of this study is the establishment of a landslide inventory information system for Southern Kyrgyzstan enabling convenient data access and analysis and serving as the basis for subsequent landslide hazard assessment at a regional scale. Due to the highly dynamic nature of the landslide activity in this region and its complex interrelations with factors that cause its differentiation in space and time, we aim at establishing a GIS-based multi-temporal landslide inventory enabling efficient derivation of landslide attributes and subsequent hazard analysis. For this purpose, we develop a GIS and remote sensing based approach for the generation of the inventory from multiple information sources with the possibility of future data updates. The resulting inventory contains spatially explicit and consistent information about landslide activity with the best possible temporal resolution. This information includes single landslide events as well as complex landslide-prone slopes, which have been subject to several phases of reactivation. Such a comprehensive inventory has not yet been compiled for the area of high landslide activity in Southern Kyrgyzstan and, when completed, can serve as an example of multi-source landslide inventory mapping in a data-scarce environment.

The use of customized GIS tools makes it possible to develop a spatial information system for landslide hazard assessment accommodating the heterogeneous data on landslides, their predisposing and triggering factors and other supplementary information as well as functionality adapted to the procedures of landslide hazard assessment. Such a system has the potential to provide more consistent data storage, efficient data access, systematic data update procedures and customized tools for spatial and statistical analysis. Due to the advances in open-source GIS, it is possible to implement the system in the framework of already existing software packages. This allows using already available GIS functionality and taking advantage of the benefits of open-source software, such as the possibility of customization, minimization of costs and flexibility. We implement the landslide inventory information system in the QGIS environment including self-customized functionality for efficient access to the landslide inventory data and derivation of additional landslide information.

## 2 Data Sources

The establishment of a multi-temporal landslide inventory for Southern Kyrgyzstan is a challenging task since the existing information on landslide failures is very heterogeneous. We consider all available sources of landslide data including information from local organizations, field work as well as results of multi-temporal satellite remote sensing analysis. The preparation of the landslide data from various sources for integration into the inventory and their verification requires the use of spatial base data of different kinds. In this section, we give an overview of the available sources of spatial base data and information on landslide occurrence.

### 2.1 Spatial Base Data

Spatial base data are needed for the derivation of the spatial location and extents of the landslides that originally did not have an explicit spatial reference and for the verification of

existing spatio-temporal information on slope failures. They are an integral part of the data provided by the landslide inventory information system and are used to derive landslide attributes, e.g. landslide dimensions, the reference to the river valley, settlement and administrative unit where the landslide is located, etc.

In order to obtain a consistent archive of surface conditions over large areas with the best temporal resolution possible and to provide common spatial reference for multi-source landslide data, a multi-temporal database of optical remote sensing imagery has been created (BEHLING et al. 2014a). It contains 592 multi-spectral middle- and high-resolution remote sensing datasets. This database includes Landsat (E)TM, ASTER, SPOT and RapidEye images acquired in 1986 – 2013 with the spatial resolution ranging between 5 m and 30 m. Standard orthorectified products from the providers were used to minimize the preprocessing effort. Even though the sensors record data in different channels, the combination of the green, red and near-infrared spectral bands is the least common spectral denominator which enables multi-sensor analysis of landslide-related surface changes. In order to ensure spatial consistency between the standard data products required for their automated analysis, they were co-registered to the Landsat reference using a fully automat-

ed approach. Overall accuracy has resulted in a high relative image-to-image accuracy of 17 m (RMSE) and a high absolute accuracy of 23 m (RMSE) for the whole co-registered database. Further details regarding the automated co-registration of the included 592 satellite images can be found in BEHLING et al. (2014a).

Derivation of landslide attributes, clarification of ambiguities related to landslide data and general orientation in the study area require the use of topographic data. We have used the 1:100 000 Soviet ordnance survey maps that were originally produced in the 1950s and 1960s and updated in the 1970s and 1980s. These topographic maps are consistently based on a transverse Mercator projection and represent a high level of spatial detail. However, they are in part outdated and many of the settlement names have changed since the independence of Kyrgyzstan in 1991.

Furthermore, digital elevation data have been used in this study to derive relief-related landslide characteristics and for perspective visualization. These data include an SRTM X-band DEM (RABUS et al. 2003), which was obtained from the German Aerospace Center (DLR) in a spike-removed form, and the freely available ASTER GDEM VERSION 2 (2011). These digital surface models largely correspond to the Earth's surface topography due to the predominantly treeless character of the vegetation in the study area.

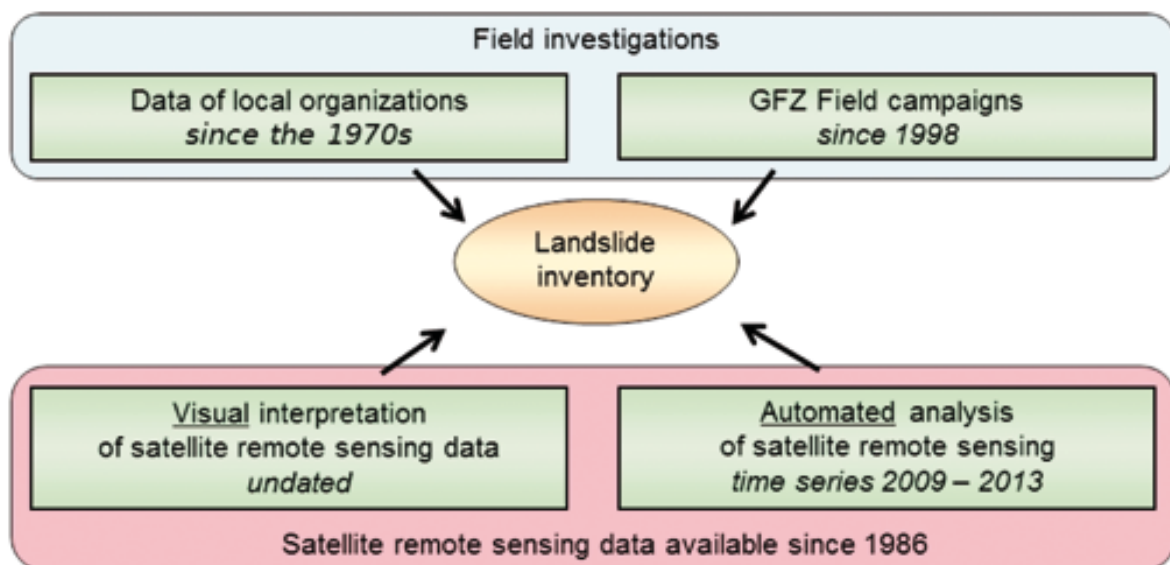


**Fig. 2:** Overview of main sources of data on landslide occurrence in Southern Kyrgyzstan.

## 2.2 Landslide Information

Multiple sources of landslide data are available (GOLOVKO et al. 2014). They include data obtained from local organizations, landslide mapping conducted during field campaigns, results of visual interpretation of mono- and multi-temporal satellite images as well as landslides which have been automatically detected from a multi-temporal satellite image database. However, these sources vary in their temporal coverage, their spatial and temporal completeness as well as their accuracy (Fig. 2). Furthermore, these landslide data are of analogue and digital origin. They have different formats, such as verbal description, tabular data, and vector information.

### 2.2.1 Information obtained from local organizations

From the 1960s until the breakup of the Soviet Union, regular landslide monitoring was conducted by local authorities for the most endangered areas in the region focusing on settlements and their surroundings (ROESSNER et al. 2005, ROESSNER et al. 2014). After the independence of Kyrgyzstan, these activities have continued; however, they decreased due to shortage of funding. The landslide records of local organizations are therefore a valuable source of landslide information covering the time period before regular satellite remote sensing data acquisition. One recent source of information on slope failures is the report by IBATULIN (2011) containing descriptions of selected landslide failures which have been documented mostly as the result of extensive field investigations carried out between the 1970s and 2004. The report comprises detailed verbal descriptions of the slope failures including results from geotechnical investigations of potentially endangered slopes. The report also contains precise temporal information on single landslide events whereby in most of the cases the exact day of the failure is known. However, it does not include explicit coordinate or map-based spatial information on the location of the slope failures. Instead, the landslide locations are described verbally in relation to significant topographic features. Overall, the report focuses on large landslides

in the vicinity of inhabited areas. Thus, it contains episodic rather than systematic landslide inventory information.

A less recent but more extensive and systematic source of information on past landslide activity is the report by YEROKHIN (1999) consisting of verbal descriptions accompanied by tabular and map-based information on landslides. It represents the cumulative assessment of the landslide situation by the end of the 1980s without specifying the dates of documented slope failures. Although this report contains spatially explicit information, the mapped landslides needed to be evaluated and spatially adjusted using satellite remote sensing data due to the coarse spatial resolution of the maps included into the report (Fig. 3). The report documents a number of landslide attributes including dimensions, position on the slope and activity stage making it the most comprehensive source of information on the properties of landslides in Southern Kyrgyzstan. Thus, the distribution of landslide attributes derived within a GIS can be validated against statistics calculated using this report.

Moreover, employees of the Ministry of Emergency Situations of Kyrgyzstan visited selected areas affected by landslides between the years 2002 and 2010 and recorded new landslides. The results of these surveys are available in form of tables. They represent only a small number of landslides which occurred in inhabited areas. Their location is represented in the table by a pair of x- and y-coordinates. However, their spatial extent is not documented. Temporal information is only contained in form of the date of field mapping whereas the time of the actual failure is mostly unknown.

### 2.2.2 GFZ field campaigns

The Remote Sensing Section of the German Research Centre for Geosciences (GFZ) has been conducting field work in Southern Kyrgyzstan since 1998 in cooperation with the Ministry of Emergency Situations of Kyrgyzstan with the purpose of selective landslide mapping and verification of data from other sources. Because of the large area affected by landslides, each of these field campaigns has covered selected parts of the study

area. However, many of these areas have been visited multiple times. Field work has been extensively supported by satellite remote sensing analysis in order to efficiently cover large areas, especially for structural geological and landslide mapping. The findings were recorded in GPS-waypoint-oriented field documentation, satellite remote sensing based maps and field photographs. Furthermore, high-accuracy measurement with differential GPS were carried out for selected topographic features and spatial reference points.

### 2.2.3 Satellite remote sensing analysis

Landslide mapping conducted during field investigations has been extended by expert interpretation of satellite remote sensing data in combination with digital elevation data and geological information using the perspective visualization capabilities of a GIS (ROESSNER et al. 2005). As a result, landslide scarps and bodies have been determined systematically for the whole area of interest. This method has proven to be especially suitable for mapping landslide-prone slopes which have experienced several phases of reactivation resulting in complex morphological structures.

However, visual mapping is labour-intensive and thus could only be carried out for subsets of the study area. In order to perform multi-temporal analysis for the whole study area, an approach for automated landslide detection has been developed based on the spatially aligned multi-temporal satellite remote sensing database (BEHLING et al. 2014a). This approach allows analysing large areas in multiple time steps. Applying this approach to the complete study area has resulted in automated detection of over 600 landslides that occurred between 2009 and 2013 (BEHLING et al. 2014b, ROESSNER et al. 2014). The obtained results, which were visually verified in the field, have revealed a constantly ongoing process activity in this region requiring regular and systematic landslide monitoring.

## 3 Methodology

The landslide inventory information system includes a landslide inventory and a spa-

tial base as well as standard and customized functionalities for data querying and analysis as part of a GIS. We have implemented the landslide inventory information system in the QGIS environment because QGIS is a well-developed open-source software package with an easy interface for the incorporation of new plugins (QGIS DEVELOPMENT TEAM 2014). Furthermore, working in the framework of QGIS allows using its available core functionality and many already existing plugins, e.g. the OpenLayers plugin for convenient visualization of data served by a Web Map Service, such as Google Satellite and OpenStreetMap, or plugins that integrate R scripts for statistical analysis.

Fig. 3 gives an overview of the steps necessary for the generation of the multi-source landslide inventory for Southern Kyrgyzstan. Most of the input data underwent preparatory processing such as digitalization, data verification and other procedures necessary to bring them to a spatially consistent form. Spatial base data were required at this stage. After the multi-source landslide inventory has been generated, it can be used for further analyses, such as derivation of landslide attributes and data preparation for landslide hazard assessment. In the following, we discuss particular steps of this workflow in more detail. They include the creation of common spatial reference, derivation of spatial mapping units, preparation of the multi-source landslide data for GIS-based integration into the resulting landslide inventory and the development of a customized functionality in the QGIS environment for efficient data access and derivation of additional landslide information.

### 3.1 *Creation of a Common Spatial Reference*

The integration of all described landslide information sources into a single system requires the establishment of a common spatial reference. For this study, the multi-temporal satellite remote sensing database (section 2.1) represents the common spatial reference. UTM/WGS84 was used as the common map projection. The resulting spatially adjusted multi-temporal satellite remote sensing data-

base is characterized by a high relative spatial accuracy between the image datasets amounting to less than the pixel size of the Landsat reference. Moreover, the absolute positional accuracy of this database has been assessed using high-accuracy differential GPS measurements. This investigation has revealed a systematic offset of the multi-temporal image database comprising 22 m in western and 5 m in northern direction (BEHLING et al. 2014a). Due to the use of orthorectified input imagery, this displacement can be regarded as a shift. The database was shifted accordingly in order to eliminate these systematic errors and ensure compatibility with spatial information originating from other sources. As a result, a consistent area-wide database of multi-temporal and multi-resolution images with a common

spatial reference has been created. All other spatial data used for the generation of the multi-source landslide inventory information system have been checked in regard to their spatial fit to this common spatial reference system. The positional accuracy of the DEMs was checked using drainage network analysis and no systematic shifts could be identified. Thus, the DEMs can be used in their original form. The scanned topographic maps were georeferenced to the common UTM/WGS projection based on their corner coordinates. In a next step, the topographic maps were used to geocode the scanned paper maps contained in the report by YEROKHIN (1999). Thus, conformity of all used spatial data with the common spatial reference has been achieved.

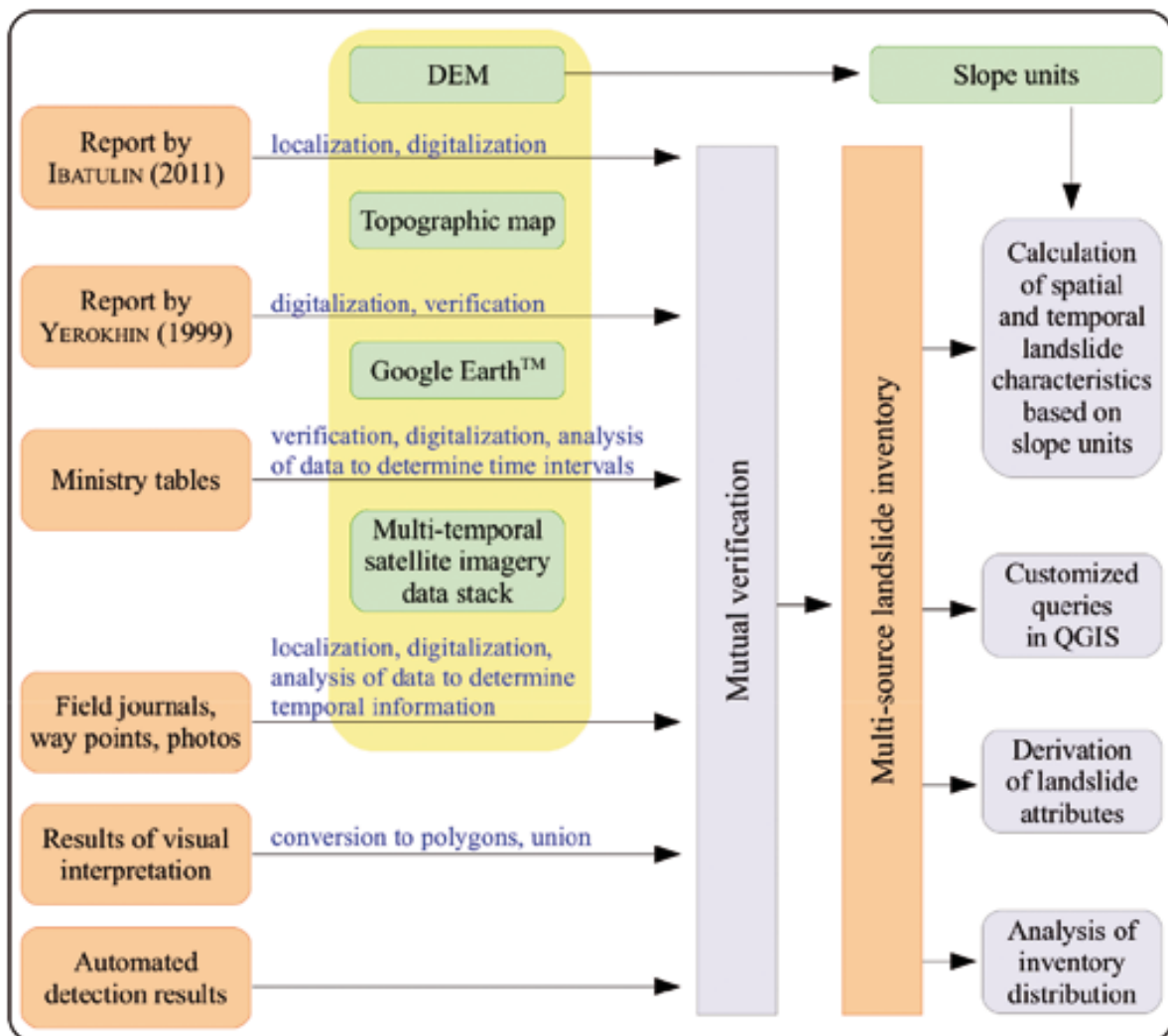


Fig. 3: Workflow for the generation of the multi-source landslide inventory.

### 3.2 *Derivation of Spatial Mapping Units*

Some of the landslide data sources provide information on single landslide failures, whereas the others document complex landslide-prone slopes, which are a result of a large number of landslide events. Both types of data need to be analysed in a combined way in order to reconstruct the spatial and temporal evolution of landslide activity for distinct slopes. This requires the determination of adequate spatial mapping units, which also form the basis for subsequent hazard assessment. They can comprise cells of a regular grid, slope units, unique condition units, seed cells and other spatial units (GUZZETTI et al. 1999, VAN DEN ECKHAUT et al. 2009, ERENER & DÜZGÜN 2012, SÜZEN & DOYURAN 2004). For this study, morphologically-based slope units which can be derived from DEM-based watershed delineation have been chosen as the most suitable mapping units because they reflect the physical properties of the relief as the main landslide predisposing factor and have the potential for handling the remaining spatial uncertainties contained in the landslide data. Due to the fractal nature of these units, their size can be adjusted to the different mapping scales by varying the parameters for watershed delineation, e.g. the stream orders or the minimum basin size (CALVELLO et al. 2013). For the study area, they were derived from the SRTM DEM and the ASTER digital elevation data and are shown in an exemplary way in Figs. 5 and 6.

### 3.3 *Landslide Data Preparation and Integration*

Landslide data from each of the sources described above differ in their properties and had to undergo a plausibility check due to imprecision, uncertainty or errors in the data. Additional data preparation was necessary to transfer landslide data from the different sources to a consistent vector form. Fig. 4 illustrates the initial situation of the landslide information availability and the outcome of the multi-source data integration for landslide inventory mapping using the example of a complex landslide-prone slope in the Kara-

Tuz river valley. Only slope failures detected automatically from multi-temporal satellite imagery in an object-based way were available in form of polygons that can be integrated into the inventory information system without further preprocessing (Fig. 4a). In case of this data source, the temporal information on the landslide occurrence was provided in form of a time interval between two image acquisition dates within which the slope failure occurred. This format was chosen for the resulting inventory to ensure comparability of data from the different sources. When the exact failure date was known, the start of the time interval was the same as its end.

Incorporating landslide information from verbal descriptions such as the report by IBATULIN (2011) required primary approximate localization of landslides using the topographic maps. Afterwards, the precise localization of the failures within the slope and the determination of their spatial extent were carried out using post-event satellite images. Sometimes, verbal information from reports concerning additional features such as landslide-dammed lakes or damage to buildings was helpful to localize the landslide in imagery acquired soon after the landslide failure. The longer the time between the slope failure and the image acquisition the more the landslide features have already been subject to erosion, revegetation and reactivations within the same slope. Often, Google Earth™ was used to supplement the multi-temporal satellite imagery due to the higher spatial resolution, convenient functionality for generating perspective views and easy-to-use digitalization tools offered by this software package.

Slope failures documented in multiple data sources were used to verify the data, correct inconsistencies, improve localization of the landslides and determine the time of their failure with higher accuracy and reliability. Even though the heterogeneous landslide data could be processed to a more consistent and mutually comparable form, differences between the data from the various sources could not be completely eliminated. Therefore, it is important to document the data source for each landslide as part of the metadata, which allows judgments about the properties and precision of the data.

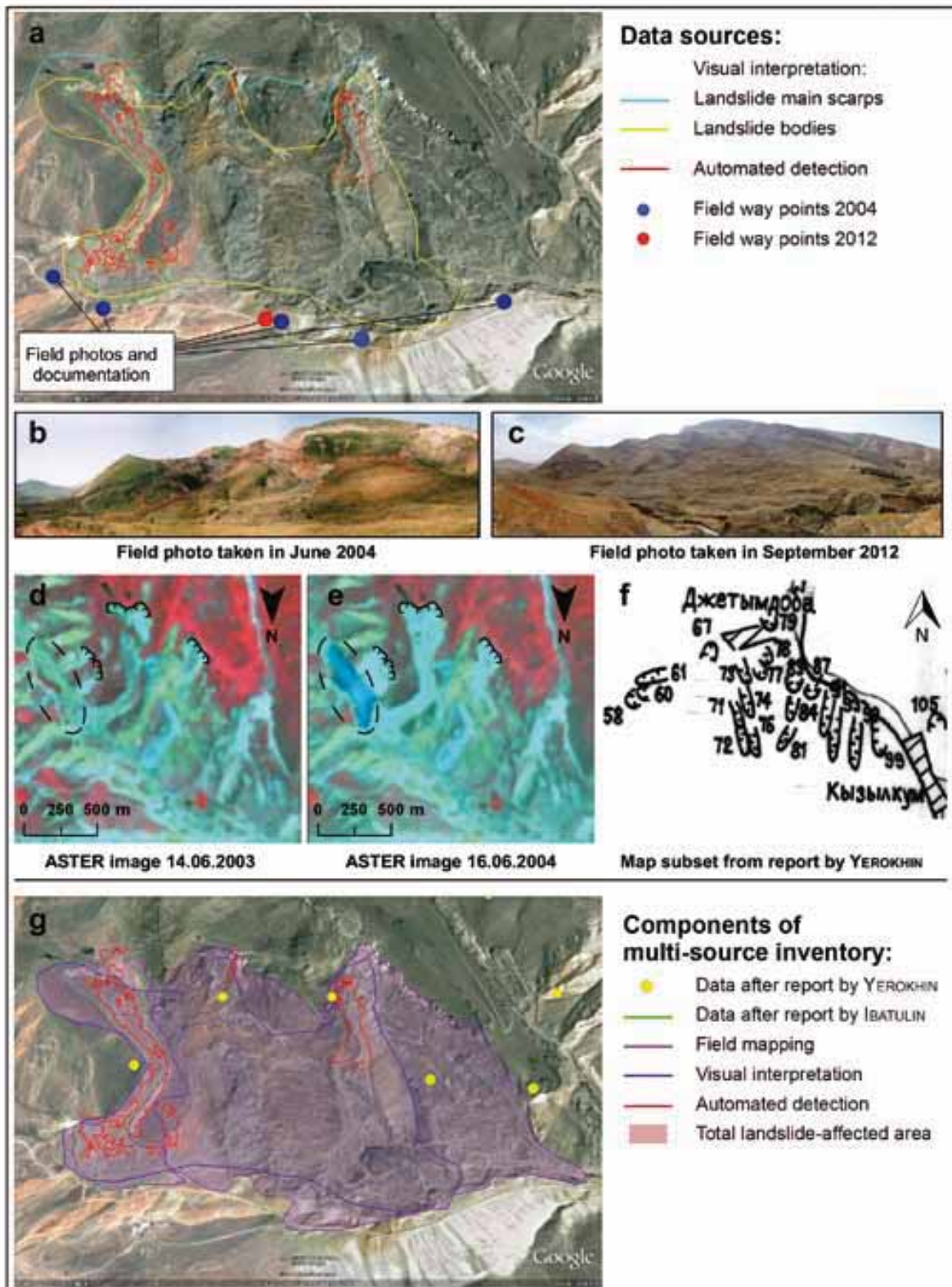


**Fig. 4:** (a–f) Input data from various sources of landslide information including field photos, pre-event and post-event ASTER images from the multi-temporal satellite remote sensing database and maps from the report by YEROKHIN (1999), (g) results of multi-source landslide mapping for a landslide-prone slope in the Kara-Tuz river valley. Google and the Google logo are registered trademarks of Google Inc., used with permission.

Additional information, such as photos, descriptions and other types of metadata, can be linked to the spatial landslide data via ids or using spatial proximity. We used ids to link attribute tables from the report by YEROKHIN (1999) to landslide locations and a spatial link between landslides and GPS waypoints recorded during field surveys, which, in turn, contain references to field photos and landslide descriptions from field journals.

The data contained in the resulting multi-source landslide inventory for the landslide-prone slope in the Kara-Tuz river valley are illustrated in an exemplary way in Fig. 4. The report by IBATULIN (2011) documents a failure which occurred in 2004 within this slope. This description contains additional information that the landslide dammed the river and formed a lake. This failure could be localized in the left part of the slope due to the availability of a post-event ASTER image where the lake is clearly visible. The location of the lake is indicated in the pre-event (Fig. 4d) and post-event image (Fig. 4e) with an ellipse. Landslides recorded in the report by YEROKHIN (1999) (Fig. 4f) prove that all parts

of the slope had already been subject to landsliding prior to the 2004 event. The results of automated landslide detection show that there were further activations within this slope in the period between 26.5.2009 and 14.5.2011 (red outlines in Fig. 4). This location was visited in 2004 and 2012 during field work when field photographs were taken and subsequently integrated into the GIS-based photo archive (Fig. 4b, c). This archive allows a better understanding of spatio-temporal dynamics of landslide-prone slopes. During field work, the whole landslide-affected slope was mapped as a single polygon because it was not possible to distinguish between individual failures. Thus, the dated landslide events occupy a relatively small area within the landslide-prone slope. However, this information is valuable for the evaluation of landslide activity in this area, and the undated landslide information allows mapping larger landslide-affected areas. The total extent of the landslide-affected area within the slope was derived as a spatial union of all landslide polygons described above and used for the calculation of landslide density as shown in Fig. 6b.

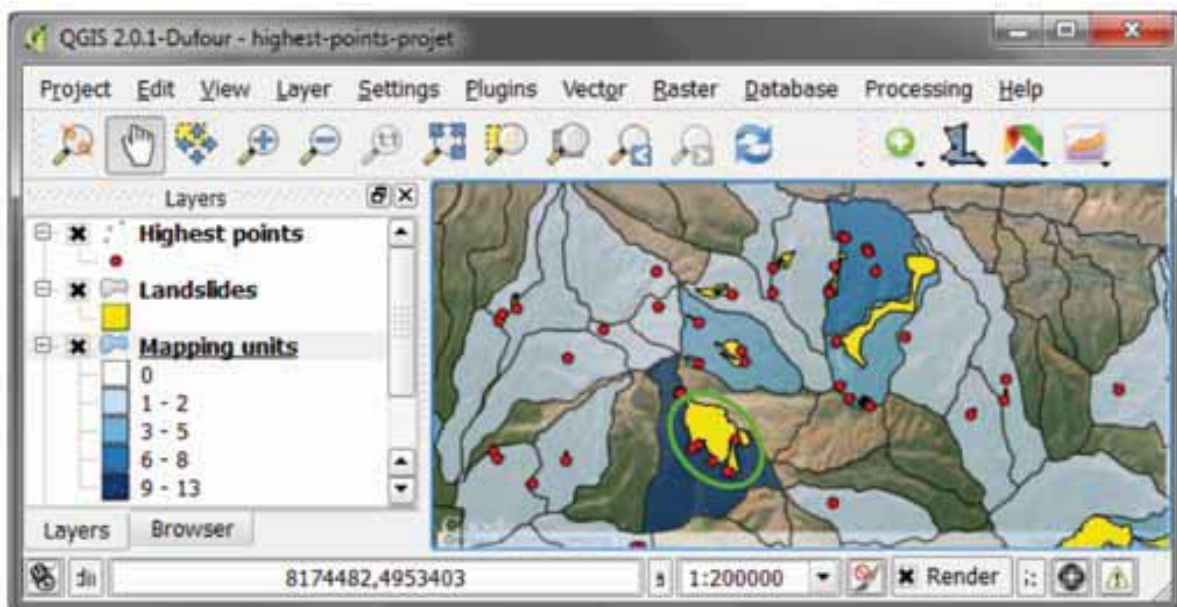


**Fig. 5:** QGIS window with landslides south of the Tar river (mapped after report by IBATULIN (2011), results of field surveys, visual and automated analysis of satellite imagery), landslide highest points and spatial mapping units indicating the number of landslides assigned to them. The green circle shows the position of the complex landslide-prone slope in the Kara-Tuz river valley used as example in the methodological description of section 3. Satellite imagery by Google via OpenLayers plugin. Google and the Google logo are registered trademarks of Google, Inc., used with permission.

### 3.4 Derivation of Additional Landslide Information

One of the components of the landslide inventory information system is a QGIS plugin written in the Python programming language. The plugin contains a set of customized functions implemented for the needs of working with the multi-temporal landslide inventory. It enables customized queries of the multi-source landslide data with an emphasis on temporal attributes. Furthermore, it provides spatial functionality for the derivation of landslide attributes, e.g. by automated referencing of landslides to spatial mapping units or finding highest points within a landslide body as an approximation of the landslide main scarp location. This type of analysis is based on the combination of vector data on landslides and spatial mapping units with a DEM. An exemplary result is shown in Fig. 5.

## 4 Results and Discussion

The resulting multi-temporal landslide inventory contains over 1.200 landslides which could be mapped as polygons based on the various sources of information (Tab. 2). The summary table also contains the total area covered by complex sequences of failures, where it has not been possible to identify individual landslides due to long-term process activity within these landslide-affected slopes. The table also shows differences in the size of the mapped landslides, e.g. the report by IBATULIN (2011)

documents a limited number of large slope failures, whereas automated landslide detection from multi-temporal satellite imagery has made it possible to map systematically landslides of all sizes including the small ones. Visual image interpretation allows mapping complex landslide-affected areas of large spatial extent, although individual failures cannot be distinguished. Automated detection enables reliable identification of the spatial extent of single slope failures. The level of detail for the temporal information depends on the availability of satellite imagery, which determines the length of the time interval between the pre-event and post-event satellite images used for dating automatically detected slope failures. The most detailed temporal information (exact day of the failure) is provided by the report by IBATULIN (2011), although the landslide extents are imprecise. Results of visual interpretation of landslide-prone slopes from satellite images and the information from the report by YEROKHIN (1999) contain no temporal information on landslide occurrence but document more landslides and a larger landslide-affected area than other sources. Thus, a trade-off between the inventory completeness, spatial and temporal information content can be observed. The integration of landslide information from multiple sources provides a way of improving the quality of the resulting inventory on these three aspects.

Fig. 6a shows the complete content of the multi-source landslide inventory for a 20 by 20 km<sup>2</sup> subset of the study area situated south of the Tar river and characterized by high re-

**Tab. 2:** Summary statistics representing the current stage of the landslide inventory according to different data sources.

Source	Period of assessment	Number of landslides	Landslide area, km <sup>2</sup>	Landslide type
Report by IBATULIN (2011)	1970s – 2004	67	22.0	Single failures
Report by YEROKHIN (1999)	1956 – 1986	1532	n/a	Single and complex failures
Ministry tables	2002 – 2011	73	n/a	Single failures
Field mapping by GFZ (status 2014)	not dated	555	119.9	Single and complex failures
Visual interpretation	not dated	n/a	172.9	Complex failures
Automated detection	2009 – 2013	625	8.2	Single failures

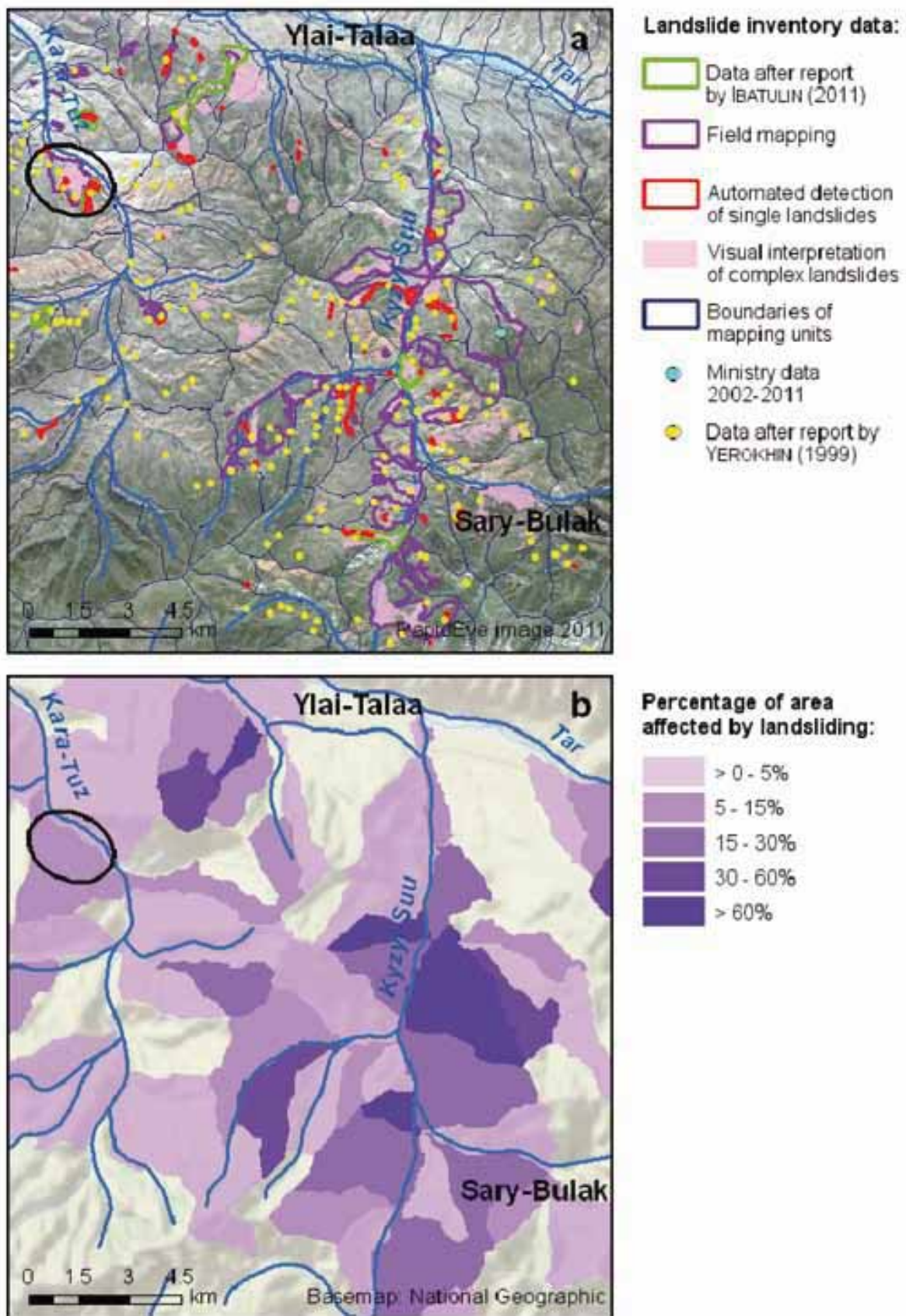


**Fig. 6:** Results of multi-source landslide mapping: (a) according to available data sources, (b) percentage of landslide-affected area per spatial mapping unit calculated using data from report by IBATULIN (2011), field mapping, visual interpretation of satellite imagery and automated landslide detection. The black ellipse shows the position of the landslide-prone slope in the Kara-Tuz river valley used as example in the methodological description of section 3.

cent landslide activity. The largest part of the mapped landslide area has been derived by visual interpretation of satellite remote sensing data in combination with field mapping (areas outlined in purple and filled in pink). Using the same combination of data sources, it has been possible to map selected large landslides contained in the report by IBATULIN (2011) in a spatially explicit way (landslides outlined in green). For these cases, the failure dates are known, all of them occurred before 2005. The areas outlined in red depict the landslide objects that have been automatically detected based on the multi-temporal RapidEye data available for the time period between 2009 and 2013. These objects include areas of fresh failures as well as areas of reactivation within previously active landslide-prone slopes.

In a second step, the total area which has been mapped as affected by landslides was derived and related to the spatial mapping units outlined in blue in Fig. 6a by calculating the landslide density as the ratio between the landslide-affected area and the total area of the respective mapping unit (GHOSH et al. 2012). The results shown in Fig. 6b indicate an especially high concentration of landslide-affected areas on the slopes along the Kara-Darya, Kyzyl-Suu and Kara-Unkyur river valleys. Overall, higher landslide densities can be observed for slopes of northern, northwestern and northeastern expositions.

The use of a common spatial reference has enabled the detection of surface cover changes in a more precise way allowing the assessment reactivations within an already known landslide complex. The precise spatial location of landslide-affected areas within a slope unit indicates the potential for the continuation of landslide activity within that slope unit. In the case of the landslide in the Kara-Tuz river valley, mass wasting has not affected the upper part of the slope unit yet, and that landslide activity may advance towards the watershed.

Although multiple sources of data on landslides have been used, each of them only provides information on a subset of the slope failures that have occurred in the study area. The degree of completeness varies depending on the examined period of time and the available data sources. Visual interpretation and auto-

mated landslide analysis based on satellite imagery allows the systematic detection of landslides independently of their proximity to settlements, whereas the completeness depends on their detectability in the image data and the temporal sequence of the imagery. However, due to the limited temporal resolution of the satellite imagery before the availability of multi-temporal RapidEye data, temporal information derived from satellite remote sensing data represents longer periods of occurrence ranging from several months to several years.

In contrast, the report by IBATULIN (2011) contains temporally explicit information on failure dates exceeding the time span which is covered by satellite remote sensing data. In case of failures that occurred before 1990, it represents the only source of temporal information on landslide events unless they have been documented otherwise. However, this information lacks explicit spatial reference and most of it has been acquired in the vicinity of settlements. Such explicit spatial information and extent of slope failures can be derived from remote sensing data, whereas the resulting accuracy is highest if the satellite imagery was acquired shortly after the occurrence of the failure. However, visual interpretation of satellite remote sensing data also allows mapping of older landslides which already have experienced several stages of revegetation and in parts have been affected by subsequent reactivations. In fact, this is the only way of mapping old landslides that had failed even before the start of landslide observations in the study area. Due to the use of the results of visual interpretation of satellite imagery, the resulting multi-source inventory combines features of both multi-temporal and historical landslide inventory mapping. The resulting spatially explicit assessment of landslide-affected areas can be used for subsequent GIS-based landslide susceptibility mapping.

## 5 Conclusions and Outlook

In this paper, we have demonstrated the use of remote sensing and GIS technologies for the development of a landslide inventory information system which is capable of integrating

multi-source information on landslide activity for the study area in Southern Kyrgyzstan. Special attention has been paid to spatially explicit landslide mapping and to the temporal dimension of landslide information. In this study area, satellite remote sensing data represent a valuable source of spatial and temporal information on landslide activity. Visual interpretation is especially suitable for mapping complex slope failures. Automated analysis allows the detection of single landslide events in an object-based form for the most recent period of time. Since none of the used sources is capable of providing a complete inventory, the combination of all of them has been required in order to derive a comprehensive landslide inventory. In this context, GIS-based data integration including homogenization and evaluation played an important role in the derivation of consistent and reliable multi-temporal information, which can be used in subsequent susceptibility and hazard analysis.

Moreover, multi-temporal satellite remote sensing data have been used as spatial reference information for establishing the multi-source GIS database since they are available in high spatial resolution and consistency for the complete study area. GIS technologies have also enabled efficient customized data access and joint processing in order to prepare all available information for subsequent landslide hazard assessment. For this purpose, a QGIS plugin is under development. Future work will focus on the development of GIS-based methods for susceptibility and hazard assessment which are capable of accommodating the spatially and temporally differentiated input information into the analysis including the results of ongoing monitoring of landslide activity in this area. In this context, special attention will be paid to the spatio-temporal assessment of landslide triggering factors, such as precipitation and seismicity in their relation to landslide activity.

## Acknowledgements

Research presented in this paper has been funded by the German Ministry of Research and Technology (BMBF) as a part of the Tien Shan – Pamir Monitoring Program (TIPTI-

MON) and PROGRESS projects. We kindly thank our colleagues from the Ministry of Emergency Situations of Kyrgyzstan K.V. IBATULIN and A.K. SARNOGOEV for providing information on landslide activity in the region and joint field work. We are grateful to developers of open-source GIS and providers of free-of-cost geodata.

## References

- ASTER GDEM VERSION 2, 2011: <http://gdem.ersdac.jspacesystems.or.jp/> (18.7.2014).
- BEHLING, R., ROESSNER, S., SEGL, K., KLEINSCHMIT, B. & KAUFMANN, H., 2014a: Automated Spatio-temporal Landslide Mapping over Large Areas Using RapidEye Time Series Data. – *Remote Sensing* **6** (3): 2572–2600.
- BEHLING, R., ROESSNER, S., KAUFMANN, H. & KLEINSCHMIT, B., 2014b: Robust Automated Image Co-Registration of Optical Multi-Sensor Time Series Data: Generation for Multi-Temporal Landslide Detection. – *Remote Sensing* **6** (9): 8026–8055.
- CALVELLO, M., CASCINI, L. & MASTROIANNI, S., 2013: Landslide zoning over large areas from a simple inventory by means of scale-dependent terrain units. – *Geomorphology* **182**: 33–48.
- ERENER, A. & DÜZGÜN, H.S.B., 2012: Landslide susceptibility assessment: what are the effects of mapping unit and mapping method? – *Environmental Earth Sciences* **66**: 859–877.
- GHOSH, S., VAN WESTEN, C.J., CARRANZA, E.J.M., JETTEN, V.G., CARDINALI, M., ROSSI, M. & GUZZETTI, F., 2012: Generating event-based landslide maps in a data-scarce Himalayan environment for estimating temporal and magnitude probabilities. – *Engineering Geology* **128**: 49–62.
- GOLOVKO, D., ROESSNER, S., BEHLING, R., WETZEL, H.-U. & KAUFMANN, H., 2014: GIS-Based Integration of Heterogeneous Data for a Multi-temporal Landslide Inventory. – SASSA, K., CANUTI, P. & YIN, Y. (eds.): *Landslide Science for a Safer Geoenvironment, Volume 2: Methods of Landslide Studies*: 799–804.
- GUZZETTI, F., CARRARA, A., CARDINALI, M. & REICHENBACH, P., 1999: Landslide hazard evaluation: a review of current techniques and their application in a multi-scale study, Central Italy. – *Geomorphology* **31**: 181–216.
- GUZZETTI, F., REICHENBACH, P., CARDINALI, M., GALLI, M. & ARDIZZONE, F., 2005: Probabilistic landslide hazard assessment at the basin scale. – *Geomorphology* **72**: 272–299.

- GUZZETTI, F., MONDINI, A.C., CARDINALI, M., FIORUCCI, F., SANTANGELO, M. & CHANG, K., 2012: Landslide inventory maps: New tools for an old problem. – *Earth Science Reviews* **112** (1–2): 42–66.
- HERVÁS, J., 2013: Landslide Inventory. – BOBROWSKY, P.T. (ed.): *Encyclopedia of Natural Hazards*: 610–611.
- IBATULIN, K.V., 2011: Monitoring of Landslides in Kyrgyzstan. – Ministry of Emergency Situations of the Kyrgyz Republic, Bishkek, Kyrgyzstan (in Russian).
- KALMETYEVA, Z.A., MIKOLAYCHUK, A.V., MOLDOBEKOV, B.D., MELESHKO, A.V., ZHANTAEV, M.M. & ZUBOVICH, A.V., 2009: Atlas of Earthquakes in Kyrgyzstan. – CAIAG, Bishkek, Kyrgyzstan.
- MOTAGH, M., WETZEL, H.-U., ROESSNER, R. & KAUFMANN, H., 2013: A TerraSAR-X InSAR study of landslides in southern Kyrgyzstan, Central Asia. – *Remote Sensing Letters* **4** (7): 657–666.
- QGIS DEVELOPMENT TEAM, 2014: QGIS Geographic Information System. Open Source Geospatial Foundation Project. – <http://qgis.osgeo.org> (9.12.2014).
- RABUS, B., EINEDER, M., ROTH, A. & BAMLER, R., 2003: The shuttle radar topography mission – a new class of digital elevation models acquired by spaceborne radar. – *ISPRS Journal of Photogrammetry and Remote Sensing* **57** (4): 241–262.
- ROESSNER, S., WETZEL, H.-U., KAUFMANN, H. & SARNAGOEV, A., 2005: Potential of satellite remote sensing and GIS for landslide hazard assessment in Southern Kyrgyzstan (Central Asia). – *Natural Hazards* **35** (3): 395–416.
- ROESSNER, S., BEHLING, R., SEGL, K., GOLOVKO, D., WETZEL, H.-U. & KAUFMANN, H., 2014: Automated Remote Sensing Based Landslide Detection for Dynamic Landslide Inventories. – SASSA, K., CANUTI, P. & YIN, Y. (eds.): *Landslide Science for a Safer Geoenvironment, Volume 2: Methods of Landslide Studies*: 345–350.
- SÜZEN, M.L. & DOYURAN, V., 2004: Data driven bivariate landslide susceptibility assessment using geographical information systems: a method and application to Asarsuyu catchment, Turkey. – *Engineering Geology* **71**: 303–321.
- TORGEOV, I.A., ALESHIN, Y.G., MELESHKO, A. & HAVENITH, H.-B., 2010: Landslide hazard in the Tien Shan, Kyrgyz Republic. – *International Conference Mountain Risk: Bringing Science to Society* **2010**: 171–174, Firenze, Italy.
- USGS, 2004: Landslide Types and Processes: <http://pubs.usgs.gov/fs/2004/3072/> (29.6.2014).
- VAN DEN EECKHAUT, M. & HERVÁS, J., 2012: State of the art of national landslide databases in Europe and their potential for assessing susceptibility, hazard and risk. – *Geomorphology* **139–140**: 545–558.
- VAN DEN EECKHAUT, M., REICHENBACH, P., GUZZETTI, F., ROSSI, M. & POESEN, J., 2009: Combined landslide inventory and susceptibility assessment based on different mapping units: an example from the Flemish Ardennes, Belgium. – *Natural Hazards and Earth System Sciences* **9**: 507–521.
- VAN WESTEN, C.J., VAN ASCH, T.W.J. & SOETERS, R., 2006: Landslide hazard and risk zonation – why is it still so difficult? – *Bulletin of Engineering Geology and the Environment* **65**: 167–184.
- VAN WESTEN, C.J., CASTELLANOS, E. & KURIAKOSE, S., 2008: Spatial data for landslide susceptibility, hazard, and vulnerability assessment: An overview. – *Engineering Geology* **102**: 112–131.
- WASOWSKI, J. & BOVENGA, F., 2014: Investigating landslides and unstable slopes with satellite Multi Temporal Interferometry: Current issues and future perspectives. – *Engineering Geology* **174**: 103–138.
- WETZEL, H.-U., ROESSNER, S. & SARNAGOEV, A., 2000: Remote sensing and GIS based geological mapping for assessment of landslide hazard in Southern Kyrgyzstan (Central Asia). – BREBBIA, C.A. & PASCOLO, P. (eds): WIT-Press: 355–366.
- WIECZOREK, G.F., 1984: Preparing a Detailed Landslide-Inventory Map for Hazard Evaluation and Reduction. – *Bulletin of the Association of Engineering Geologists* **21** (3): 337–342.
- WP/WLI (International Geotechnical Societies = UNESCO Working Party on World Landslide Inventory), 1993: *Multilingual Landslide Glossary*. – BiTech Publishers Ltd.
- YEROKHIN, S.A., 1999: Investigation of Landslide Occurrence in Osh and Dzhahal-Abad Provinces of the Kyrgyz Republic. – Bishkek, Kyrgyzstan (in Russian).

#### Addresses of the Authors:

DARYA GOLOVKO, SIGRID ROESSNER, ROBERT BEHLING & HANS-ULRICH WETZEL, GFZ German Research Centre for Geosciences, Section 1.4 – Remote Sensing, Telegrafenberg, D-14473 Potsdam, Tel.: +49-331-288-1765, Fax: +49-331-288-1192, e-mail: {dgolovko}{roessner}{behling}{wetz}@gfz-potsdam.de

BIRGIT KLEINSCHMIT, Technical University Berlin, Institute for Landscape Architecture and Environmental Planning, Straße des 17. Juni 145, D-10623 Berlin, Tel.: +49-30-314-72847, Fax: +49-30-314-73290, e-mail: birgit.kleinschmit@tu-berlin.de

Manuskript eingereicht: Juli 2014  
 Angenommen: Dezember 2014



## Georeferencing Multi-source Geospatial Data Using Multi-temporal TerraSAR-X Imagery: a Case Study in Qixing Farm, Northeast China

QUANYING ZHAO, CHRISTOPH HÜTT, VICTORIA I. S. LENZ-WIEDEMANN, Cologne, YUXIN MIAO, Beijing, China, FEI YUAN, Mankato, MN, USA, FUSUO ZHANG, Beijing, China & GEORG BARETH, Cologne

**Keywords:** georeferencing, spatial inconsistency, multi-source data, TerraSAR-X, topographic vector data, optical remote sensing imagery

**Summary:** Geodata, including optical remote sensing (RS) images and topographic vector data, can be collected from multiple sources such as surveying and mapping agencies, commercial data acquisition companies, and local research institutes. These multi-source data have been widely used in past RS and geographic information system (GIS) studies in various applications. However, spatial inconsistencies inherent in the multi-source data require accurate georeferencing to be applied. This is challenging for study sites with limited accessibility and few reference maps. To address this challenge, this paper proposes an approach for generating ground control points (GCPs) using TerraSAR-X (TSX) data. In a case study, TSX images were used to georeference multi-source data covering the Qixing Farm in Northeast China. First, a stack of five multi-temporal TSX images were processed into one reference image to retrieve GCPs. These were then used to georeference the other datasets including Huanjing (HJ), Landsat 5 (LS 5), FORMOSAT-2 (FS-2), and RapidEye (RE) satellite images, as well as topographic vector datasets. Identifying tie points in the multi-source datasets and the corresponding GCPs in the TSX reference image enables georeferencing without field measurements. Finally the georeferencing accuracies for the optical RS images were assessed by using independent check points. Good results were obtained for the HJ, LS 5, FS-2 and RE images, with an absolute error of 7.15 m, 6.97 m, 8.94 m and 10.52 m, respectively. For the topographic vector datasets, ideal visual results were achieved, attributable to the rubber sheeting algorithm. These results demonstrate that the TSX reference image is suitable for georeferencing multi-source data accurately and cost-efficiently. The developed procedure can be applied in other study regions and is especially valuable for data-poor environments.

**Zusammenfassung:** Georeferenzierung von Raster- und Vektordaten aus unterschiedlichen Quellen mit Hilfe von multitemporalen TerraSAR-X-Aufnahmen – eine Fallstudie der Qixing-Farm im Nordosten Chinas. Für räumliche Analysen kommen Geodaten wie Fernerkundungsdaten und topographische Vektordaten zum Einsatz, die von diversen Einrichtungen, u.a. Vermessungsämtern, kommerziellen Geoinformations-Dienstleistern und Forschungsinstituten bereitgestellt bzw. bezogen werden. Diese aus unterschiedlichen Quellen stammenden Daten (Multidaten) werden für zahlreiche Anwendungen in Fernerkundungs- und GIS-Studien genutzt. Jedoch beinhalten diese Daten räumliche Ungenauigkeiten, die zunächst eine präzise Georeferenzierung erforderlich machen. Dieses stellt vor allem für Untersuchungsgebiete mit eingeschränkter Zugänglichkeit und nicht verfügbaren Referenzdaten eine Herausforderung dar. Dieser Artikel erklärt, wie Passpunkte aus Daten des Radarsatelliten TerraSAR-X (TSX) für die Georeferenzierung von Multidaten generiert werden können. In einer Fallstudie der Qixing-Farm im Nordosten Chinas wurden fünf multitemporale TSX-Radarbilder zu einem Referenzbild zusammengefügt, um mit hoher Genauigkeit Passpunkte abzuleiten. Diese Passpunkte dienen der Georeferenzierung mehrerer Multidaten aus diversen Quellen, welche sowohl Huanjing (HJ)-, Landsat 5 (LS 5)-, FORMOSAT-2 (FS-2)-, und RapidEye (RE)-Satellitenbilder als auch topographische Vektordaten umfassen. Die Identifizierung derselben Passpunkte in dem TSX-Referenzbild und in den Multidaten diverser Quellen ermöglicht eine genaue Georeferenzierung ohne im Gelände aufgenommene Messdaten. Die Genauigkeit der Georeferenzierung für die optischen Satellitenbilder wurde durch unabhängige Kontrollpunkte bewertet. Es wurden gute Ergebnisse für die HJ-, LS 5-, FS-2-

und RE-Satellitenbilder mit absoluten Fehlern von 7,15 m, 6,97 m, 8,94 m bzw. 10,52 m erzielt. Für die Georeferenzierung der topographischen Vektordaten wurden optimale visuelle Resultate erzielt, welches dem eingesetzten „Rubber Sheeting Algorithm“ zuzuschreiben ist. Diese Ergebnisse demonstrieren die Eignung der aus TSX-Daten abge-

leiteten Passpunkte, um Multidaten verschiedener Quellen genau und kosteneffizient zu georeferenzieren. Das entwickelte Verfahren kann auf andere Untersuchungsregionen übertragen werden und ist besonders wertvoll für Gegenden mit schlechter Verfügbarkeit von Referenzdaten.

## 1 Introduction

Data quality plays a critical role in geodata related research (BARETH 2009). To ensure data quality, georeferencing becomes a mandatory and crucial task. In this paper, datasets from different sources, each characterized by their unique attributes and properties, are referred to as multi-source data. Compared to single-source data, multi-source data can provide adequate information with different spatial and temporal resolutions, map scales, and spectral properties (LI 2010, WALDHOFF et al. 2012). Multi-source data provided by various governmental bureaus or non-governmental organizations such as local research institutions or special research groups may vary in many interpretation aspects and in terms of (spatial) data quality. Both geographic information system (GIS) and remote sensing (RS) data carry plenty of geospatial information but with different nature and content and with different semantics (WEIS et al. 2005). The integration of RS and GIS is emerging as a new research field (ZHANG 2010). GÓMEZ-CANDÓN et al. (2012) indicated that the locational errors in high resolution images, e.g. GeoEye-1 images, affect the delineation of the input prescription map which is a core problem for the implementation of site-specific agricultural management strategies. WEBER et al. (2008) confirmed that coregistration errors between imagery and field sites led to remarkable errors in landscape classification, particularly when the size of the target site was similar to the image pixel size. Moreover, in some cases, such as in China, detailed topographic data (1:5,000 – 1:25,000) with high spatial accuracy may not be accessible due to data sharing and management policies or lack of surveying and mapping activities (BARETH & YU 2004). Because of heterogeneous qualities, the integration and georeferencing processes for mul-

ti-source data are indispensable, complex and highly dependent on the purpose of the study.

A variety of methods for multi-source data integration and georeferencing have been developed in the past decades to eliminate spatial inconsistencies in multi-source datasets. For example, a Markov random field model was applied to merge images from multiple sensors for a land use classification (SOLBERG et al. 1996). A statistical approach to match relational features was introduced by WALTER & FRITSCH (1999). An iterative closest point algorithm was implemented to match features using a spatially precise map as the reference (VON GÖSSELN & SESTER 2004). Empirical and theoretical methods were implemented by USERY et al. (2009) for integrating the national maps of the United States with different scales and resolutions in vector and raster datasets. In addition, several automatic approaches have been developed to compute the imagery-to-vector conversion (WU et al. 2007), identify control point pairs from images using vector datasets as the glue layers (CHEN et al. 2006), conflate vector maps to high resolution imagery (SONG et al. 2009), or georeference image sequences in real-time (CHOI & LEE 2012).

In recent studies, Synthetic Aperture Radar (SAR) imagery has been used to quantify the spatial inconsistencies of geodata and to collect ground control points (GCPs) for georeferencing. SAR sensors are all-weather and day-night active microwave sensors that collect information of the targets according to the signal transport time between the sensor position and the terrain height. They have the potential to provide images with very high geometric accuracy (AGER & BRESNAHAN 2009, RODRÍGUEZ et al. 2006). In particular, the German TerraSAR-X (TSX) satellite launched in 2007 is equipped with a highly flexible phased

array antenna for SAR Stripmap, ScanSAR, and Spotlight operations (MITTERMAYER & RUNGE 2003). An overall ground accuracy of less than 1 m has been demonstrated when the images are projected to a precise terrain height (AGER & BRESNAHAN 2009, KOPPE et al. 2010, NONAKA et al. 2008). Therefore, the TSX products can be used to generate topographic maps and create accurate orthoimagery products (BADURSKA 2011, REINARTZ et al. 2011, SCHNEIDER et al. 2009).

To further explore the potential capability of TSX imagery as a source for locating GCPs and subsequently to georeference multi-source data characterized by varying properties and accuracies over a large area, a feasible and robust method which takes the advantage of the high spatial resolution and high geometric accuracy of TSX imagery is introduced. The main specific objectives are (i) to georeference topographic vector data from multiple sources; (ii) to improve the georeferencing results of Huanjing (HJ), Landsat 5 (LS 5), FORMOSAT-2 (FS-2), and RapidEye (RE) satellite images; and (iii) to assess the accuracy of georeferenced datasets and to evaluate if the results are highly dependent on the spatial accuracy of the TSX imagery.

## 2 Study Area and Data

### 2.1 Study Area

The Sanjiang Plain (SJP), located in Northeast China, is an alluvial plain formed by the Songhua River, the Heilong River and the Wusuli River. The topography is fairly flat with a slope of  $< 0.012^\circ$ . With an area of approximately 11 million ha, it is an important wetland area and ecosystem in China. Some wetland sites in this area have been designated for the list of wetlands of international importance (WANG et al. 2006). In addition, the SJP is the largest food base of China, where 52 national-owned farms are located. The climate is temperate sub-humid, with a mean annual precipitation of 500 mm – 600 mm (80% of it occurring between May and September), and an average temperature of  $21^\circ\text{C}$  –  $22^\circ\text{C}$

in July and  $\sim -18^\circ\text{C}$  in January. Nowadays, single season crops of paddy rice, soybean and maize are mainly planted in this area.

The study site Qixing Farm ( $47.2^\circ\text{N}$ ,  $132.8^\circ\text{E}$ ), which covers an area of approximately 120,000 ha, is located in the central part of the SJP (Fig. 1). As of 2010, 62% of the study site was arable, dominated by three quarters of paddy rice and one quarter of dry-land (ZHANG 2012). In the paddy rice fields, rainfed and irrigation systems simultaneously exist. To improve the growing conditions of agricultural crops, shelter forests were planted in the late 1980s, primarily to reduce the speed of ground wind (LIU & ZHAO 1996).

### 2.2 Data Description

A time series of five TSX images (stripmap, VV-polarisation, incidence angle  $\sim 35^\circ$ , relative orbit 88, descending) was taken within 44 days from June 24 to August 7 of 2009 (see Tab. 1). These five stripmap images in the basic Single Look Slant Range Complex (SSC) form with intensity and phase information for each pixel in slant range geometry were used to create a TSX reference image. The orbit precision was set to ‘science’, which means that the satellite position during image acquisition is calculated with an error of less than 20 cm in a post processing step (FRITZ &

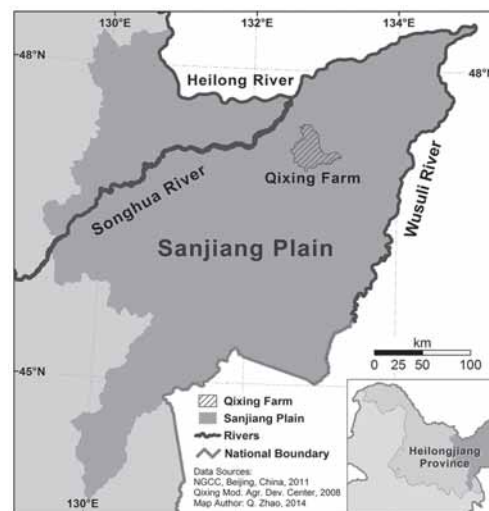


**Fig. 1:** Location of the study area Qixing Farm in Northeast China.

EINER 2013). This post processing dramatically increases the positional accuracy and thereby the image potential for generating GCPs (KOPPE et al. 2010).

The Qixing Farm field boundary file was produced by the Qixing Modern Agriculture Development Center. This GIS layer was given in Universal Transverse Mercator (UTM) coordinate reference system, zone 53 N. It provides the information on crop field boundaries, irrigation wells, water drainages, and shelter forests edges at a fine field unit scale. However, this dataset did not line up with any of the other datasets in our project. The inconsistency was nonsystematic in distance or directions (Fig. 3). An offset of more than 200 m between this dataset and the TSX images was identified in the northwest part, whereas in the southeast part the shift was more than 300 m in the opposite direction.

The public version of the 1:250,000 topographic vector dataset was produced by the National Geomatics Center of China (NGCC). This dataset includes multiple layers of administration boundaries, settlements, railways, roads, hydrological information, and landscapes. However, as BARETH & YU (2004) indicated, the spatial accuracy is not as high as expected. Therefore, a refined georeferencing of the public version is needed in this study.

The HJ, LS 5, FS-2, and RE satellite images were acquired from 2009 to 2012 in the growing season. The agricultural constructions, e.g. irrigation channels and raised ridges, for paddy rice in the study area are the same year

by year and the field boundaries are mostly stable. Therefore, one TSX reference image can be used in multiple years. The detailed information of the RS data is listed in Tab. 1.

### 3 Methods

#### 3.1 Workflow of Georeferencing Multi-source Datasets

The schematic workflow of multi-source data georeferencing is shown in Fig. 2. There are mainly four steps involved: (1) pre-processing of the multi-temporal TSX images to generate one single reference image; (2) selection of GCPs from the processed TSX imagery and corresponding tie points from optical RS images or topographic vector maps; (3) reducing locational errors by recursively reselecting GCPs and corresponding tie points until achieving low positional error (PE) values or satisfactory visual results; (4) generating georeferenced datasets by image resampling or GIS data matching. Steps 1 and 2 are the key steps of this approach, which highly affect the quality of the GCP interpretation and consequently the final results.

We decided to use the PE because it is implemented in the software that we used and because the documentation of the individual error of every point proves best the efficiency of the proposed method. The standard deviation (Std.) that characterizes the overall error is also given as a comparison (Tab. 2).

**Tab. 1:** Characteristics of the RS images (az = azimuth, along track, rg = range, across track).

Satellite	Pixel Spacing (m)	Bands	Acquisition Date	Projection	Cloud Cover (%)	Processing Level
TSX	1.89 (az) × 1.57 (rg)	-	June 24, July 5, 16, 27, Aug. 7, 2009	WGS 84 UTM 53 N	--	SSC
HJ(CCD2)	30 × 30	4	June 29, 2012	WGS 84 UTM 53 N	0 (subset)	2
LS 5	30 × 30	7	Aug. 26, 2011	WGS 84 UTM 52 N	0 (subset)	1T
FS-2	2 × 2 (PAN)	5	July 6, 2009	Geographic (Lat/Lon)	0	1A
RE	5 × 5	5	May 19, 2012	WGS 84 UTM 53 N	0	3A

### 3.2 Creation of the Reference Image from TSX Stripmap Acquisitions

A stack of five TSX stripmap images was used to create the reference image. Radar image processing was performed using the Next ESA SAR Toolbox (NEST) distributed under the GNU General Public License. To meet the requirement of a geocoded image in which the precise outlines of objects are identifiable, certain pre-processing techniques were applied. First the ‘complex pixel value’ were used to calculate an amplitude image representing the strength of radar backscatter for each radar pixel cell. During the following

‘range Doppler terrain correctio’, the elevation data from the Space Shuttle Topography Mission (SRTM) in a spatial resolution of 3 arc-seconds served to transform the radar images from slant range geometry into the UTM coordinate reference system. Pixel spacing of the resultant geocoded product was set to 2 m to minimize spatial information loss, and to meet the file requirements of a manageable product. The main drawback of the SAR image with regard to the visible interpretation is the speckle effect which is an inherent noise of all radar images, often called grainy salt and pepper noise. To reduce this effect, a mean image of the five geocoded images was calculat-

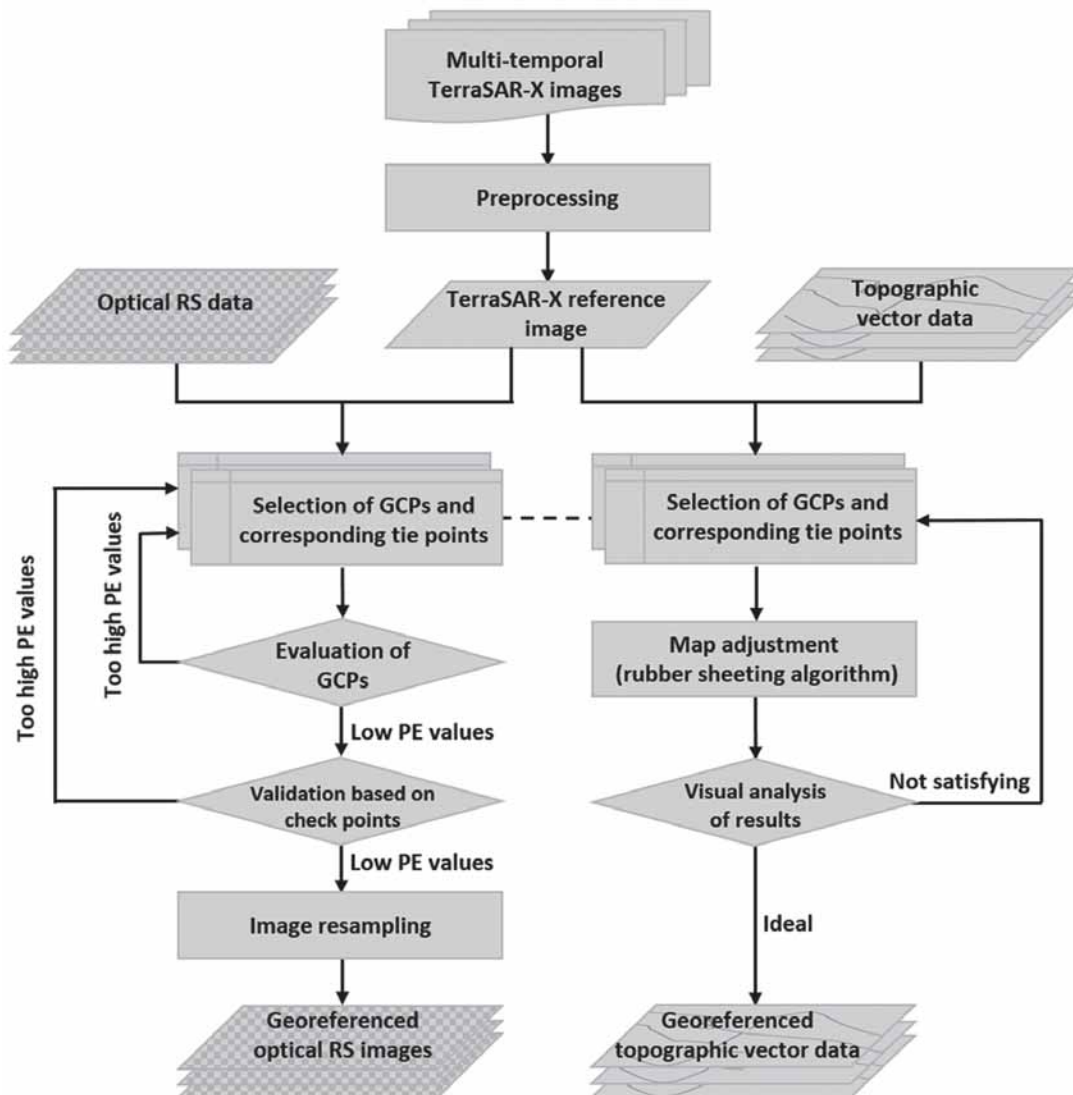


Fig. 2: Georeferencing workflow of the multi-source geospatial data, PE = positional error.

ed and a 3x3 mean speckle filter applied. The radiometric resolution was reduced from 16 bits to 8 bits. Therefore, the data size was considerably reduced. Likewise, the image representation speed was dramatically increased. In spite of a radiometric information loss during this procedure, the processed TSX reference image provides sufficient information for human interpreters to clearly define unambiguous GCPs with a high spatial resolution. Absolute radiometric calibration was not needed in this process as all five images have the same calibration constants, and moreover, the quantitative analysis of the backscattered signal was not the focus of this study. The resultant greyscale radar image was almost speckle-free and the shapes of all objects necessary in this research could be identified.

### 3.3 Georeferencing of Topographic Vector Data

Georeferencing of the topographic vector data was based on a rubber sheeting algorithm. The rubber sheeting, alternatively called rubber sheet, algorithm is one of the earliest and the most common computer cartogram algorithms (TOBLER 2004). This technique derives its name from the logical analogy of stretching a piece of rubber to fit over some objects (COBB et al. 1998). During the process, map areas are subdivided into triangular-shaped regions and local adjustments are applied on each single region. After that, each triangle either enlarges or shrinks iteratively toward its ideal size without changing the topology of the map (GILLMAN 1985, DOUGENIK et al. 1985). An iterative math-physical cartogram algorithm for continuous area was proposed by DOUGENIK et al. in 1985. This algorithm was recently improved by implementing an auxiliary quadtree structure in the process (SUN 2013a, 2013b).

In this study, the rubber sheeting tool of ArcGIS 10.1 was used to transfer the topographic vector data. Approximately 600 reference points, evenly distributed over the entire area of Qixing Farm, were selected as georeferencing points from the TSX reference image. As REINARTZ et al. (2009) proposed, the selection of reference points from the TSX image is not always a straightforward procedure. Based on

our experience, corresponding points were selected according to following rules: (i) Select points in the TSX reference image that are located at the intersection of the paddy field ridges, rural road edges, canopy crossings of different crops, or corners of artificial waters, which are in all cases clearly identifiable and unchanged during the 3 year-period from 2009 to 2012. (ii) Avoid elevated objects such as forest edges or tall buildings due to their systematic locational errors such as foreshortening, layover, and shadowing, induced by the radar imagery acquisition procedure. (iii) Select only points that have a corresponding (tie) point in the vector dataset, e.g. the Qixing Farm boundary data with line intersections and corners. A similar process was applied to the topographic GIS data provided by the NGCC.

### 3.4 Georeferencing of Optical RS Data

Multiple optical RS aforementioned data were also selected to demonstrate the georeferencing process based on the TSX reference image. In particular, image subsets covering the Qixing Farm were created for the HJ and LS 5 satellite data. All optical satellite images were georeferenced according to these main steps: First, all satellite images were reprojected into the UTM WGS 84 system to obtain an overview of the data inconsistencies. Second, a set of control points was selected from the TSX reference image based on the aforementioned rules. Consequently, the corresponding points have to match the objects which can be clearly identified in the optical RS imagery in this case. Third, in order to improve the transformation model and to minimize the errors caused by the manual measurement, GCPs and corresponding tie points were updated iteratively by eliminating the points with highest PEs and selecting additional control points until the residual errors fell below the maximum allowed value. The decision if a PE value was too high depended on the spatial resolution of the image to be georeferenced. For every single GCP, the maximum allowed value was within the subpixel range. Finally, a certain number of independent points were de-

fined as check points to evaluate the accuracy of the transformation. During the validation process, the GCPs were used to calculate the transformation model while the check points were used to evaluate the errors in the geometric transformation independently.

In our case, the PE is the horizontal distance between the input location of a GCP and the transformed location of the same GCP. The PE was calculated according to (CONGALTON & GREEN 2008).

$$PE = \sqrt{\Delta X^2 + \Delta Y^2} , \tag{1}$$

where  $\Delta X$  and  $\Delta Y$  are the positional differences between the reference point and the corresponding image or map position in the  $X$  and  $Y$  directions, respectively.

## 4 Results

### 4.1 Georeferencing Results of Topographic Vector Data

After the georeferencing based on the rubber sheeting algorithm, the georeferenced vector data of the Qixing Farm field boundaries (cyan) sufficiently fit to the new field boundaries which are clearly detectable in the TSX image. The problem of nonsystematic spatial inconsistency was well overcome and the shape of the vector graphics was preserved (Fig. 3). Similar results were also obtained for the topographic data provided by the NGCC.

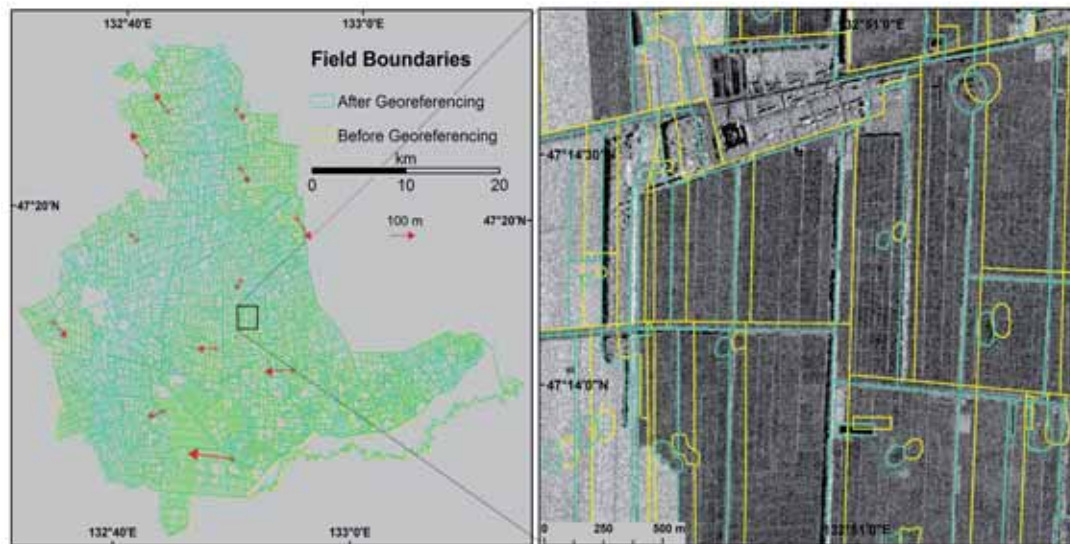


**Fig. 3:** Field boundary data, before (yellow) and after (cyan) the georeferencing; red arrows in the left figure show the vector force of the rubber sheeting procedure. Background data in the right figure: TSX reference image.

**Tab. 2:** Accuracy of the selected GCPs (PE = positional error, Std. = standard deviation).

Satellite	Pixel Size (resampled) (m)	Imagery/subset spatial extension (km)	Number of control points	PE (average) (m)	PE (max.) (m)	PE (min.) (m)	Std. (m)
HJ (CCD2)	30 × 30	55 × 55	100	12.66	27.39	1.87	6.70
LS 5	30 × 30	48 × 68	220	9.04	16.63	0.59	3.85
FS-2	2 × 2 (PAN)	30 × 28	143	3.43	5.91	0.3	1.35
RE	5 × 5	24 × 24	64	4.09	9.36	0.60	2.12

#### 4.2 Georeferencing Results of Optical RS Data

Optical RS data were georeferenced according to the method described in the previous sections. Tab.2 shows the relevant information of the selected GCPs.

After recursively selecting control points, the final PEs were less than half a pixel for both the HJ (CCD2) and LS 5 images, and nearly one pixel for the FS-2 and RE images. Fig. 4 shows the georeferencing results visually. The ground features from each of the images fit well. The roads match properly in all

images and the paddy field block boundaries are ideally aligned to each other in the higher resolution images (TSX, FS-2 and RE).

#### 4.3 Spatial Accuracies of the Georeferenced Optical RS Data

To evaluate the spatial accuracies of the georeferenced optical RS data, independent check points covering the whole scene were created and their spatial parameters were analyzed. To capture the maximum PE results, the check points were located in the areas where the

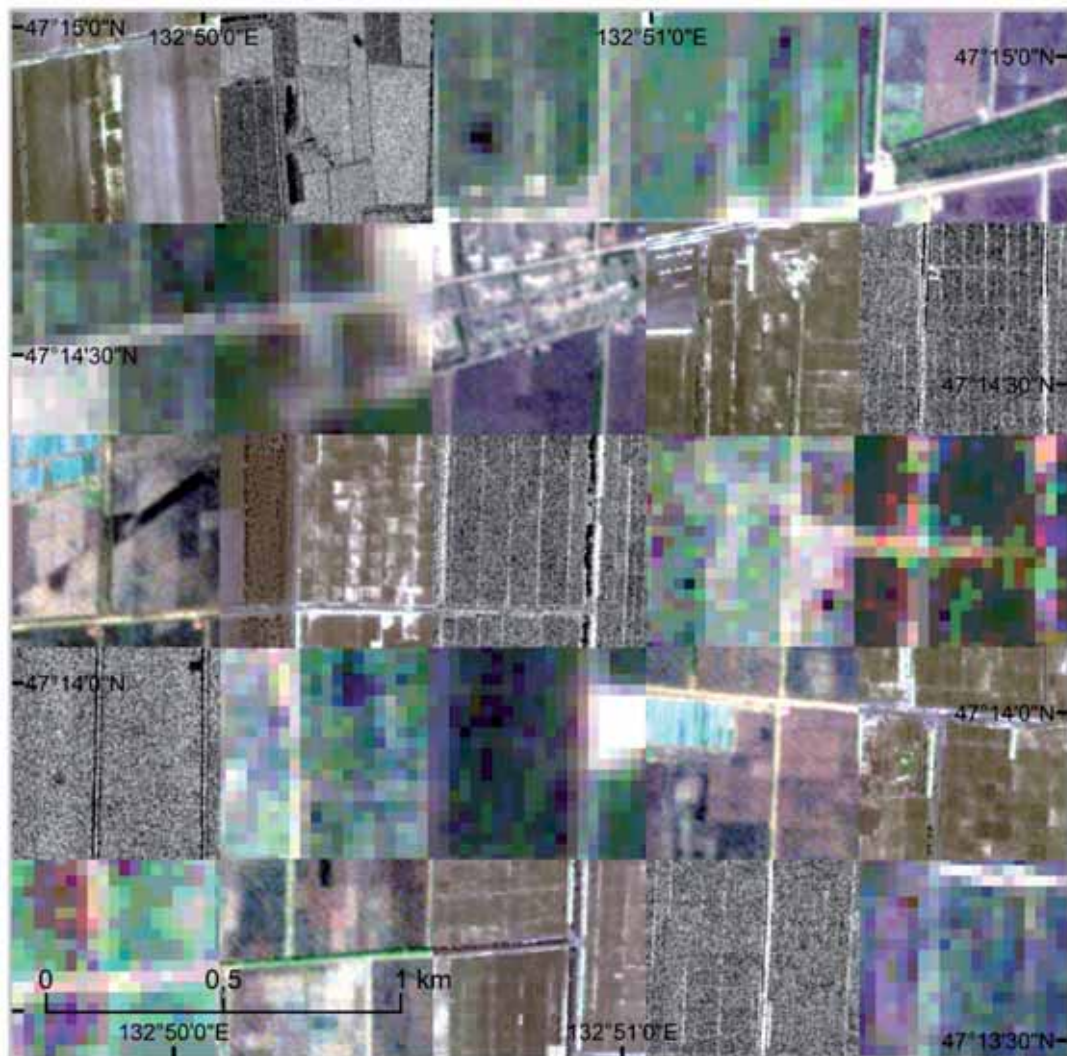


**Fig. 4:** An example of georeferenced multi-source RS images in comparison to the TSX image. From left to right: 1<sup>st</sup> row: FS-2, TSX, LS 5, HJ, RE; 2<sup>nd</sup> row: LS 5, HJ, RE, FS-2, TSX; 3<sup>rd</sup> row: RE, FS-2, TSX, LS 5, HJ; 4<sup>th</sup> row: TSX, LS 5, HJ, RE, FS-2; 5<sup>th</sup> row: HJ, RE, FS-2, TSX, LS 5.

**Tab. 3:** Accuracy of the independent check points.

Satellite	Pixel Size (resampled) (m)	Imagery/ subset spatial extension (km)	Number of check points	PE (average) (m)	PE (max.) (m)	PE (min.) (m)	Std. (m)
HJ (CCD2)	30 × 30	55 × 55	20	3.29	8.05	1.81	1.55
LS 5	30 × 30	48 × 68	34	3.11	6.48	1.80	1.11
FS-2	2 × 2	30 × 28	30	5.08	7.44	1.07	1.89
RE	5 × 5	24 × 24	10	6.66	8.42	4.08	1.21

GCP density was relatively low. The results were summarized in Tab. 3. The average PEs of the check points were at a sub-pixel value (slightly more than 0.1 pixel) in the HJ (CCD2) and LS 5 images. Accuracies of 2.5 pixels and 1.3 pixels were achieved for the FS-2 and RE imagery, respectively. The average PE values for all four types of satellite images ranged from 3.11 m to 6.66 m.

## 5 Discussion

### 5.1 Analysis of the Anticipated Spatial Error in the Processed TSX Reference Image

The geometric distortion of SAR imagery products can be caused by three components (CURLANDER & McDONOUGH 1991): (i) sensor/platform instability and signal propagation effects, (ii) terrain height, and (iii) processor induced errors. The uncertainties embedded in the SSC products comprise only the first type of error, which is less than 1 m (NONAKA et al. 2008, FRITZ & EINEDER 2013). The second type of errors comes from the SRTM DEM dataset. RODRIGUEZ et al. (2006) found that the absolute height error of the SRTM in Eurasia was less than 6.2 m; whereas in the SJP study site, where the topography is fairly flat, the absolute error was less than 2 m according to the SRTM THED (terrain height error data) product.

Hence, the target range location error ( $\Delta R$ ) determined by the terrain height estimation can be calculated using (2) (CURLANDER & McDONOUGH 1991):

$$\Delta R = \Delta h / \tan \eta, \quad (2)$$

where  $\Delta h$  is the height (DEM elevation) estimation error (2 m) and  $\eta$  is the location incidence angle ( $35^\circ$  in this study). Therefore, the  $\Delta R$  for this study was calculated as 2.86 m. The processor induced error is process dependent and is denoted as  $\Delta \delta_i$ . The overall absolute spatial error of the projected TSX imagery can therefore be calculated by these three components, with the result of  $(3.86 + \Delta \delta_i)$  m. Where the processor induced error  $\Delta \delta_i$  during TSX image processing can be assumed to be infinitely small.

### 5.2 Quantified Spatial Accuracy of the Georeferenced Datasets

Considering all spatial inconsistent sources, the overall absolute error of the georeferenced datasets can be estimated. The overall errors of the georeferenced optical RS data, which is equal to the sum of the PE in Tab. 3 and the geometric distortion of the TSX image (3.86 m), were 7.15 m, 6.97 m, 8.94 m, and 10.52 m for HJ, LS 5, FS-2, and RE satellite images, respectively. DAI & KHORRAM (1998) found that a registration error of less than one-fifth of a pixel should be achieved to detect 90% of the true changes. Hence, the registration results for the HJ (CCD2) and LS 5 images can support a change detection analysis with a spatial error close to 10%.

In surface area estimation, OZDOGAN & WOODCOCK (2006) noted that spatial errors are dependent on both RS image resolution and the field size because of ‘the distribution of subpixel proportions’, especially when the field size is similar to or less than the RS data resolution. In this study, the results of the FS-2 and RE images processing are suf-

ficient for field-unit level analysis since the size of each field block unit is typically larger than 5,000 m<sup>2</sup>. The field block is the smallest area of a farm management unit and is considered as the primary scale for management decisions. The high accuracies for the HJ and LS 5 image processing are also beneficial for studies at the farmer-unit level, as a farmer's crop field is generally larger than 20 ha. Fig. 5 provides a visual result of datasets from multiple sources over the entire area of the Qixing Farm.

### 5.3 Feasibility of the Approach

In this study, topographic vector datasets and optical RS images from multiple sources were georeferenced using GCPs derived from the TSX reference image without the need for labour intensive field work. The creation of the TSX reference image and its use to locate accurate GCPs is critical, because it not only determines the precision of the results but also the feasibility of this method.

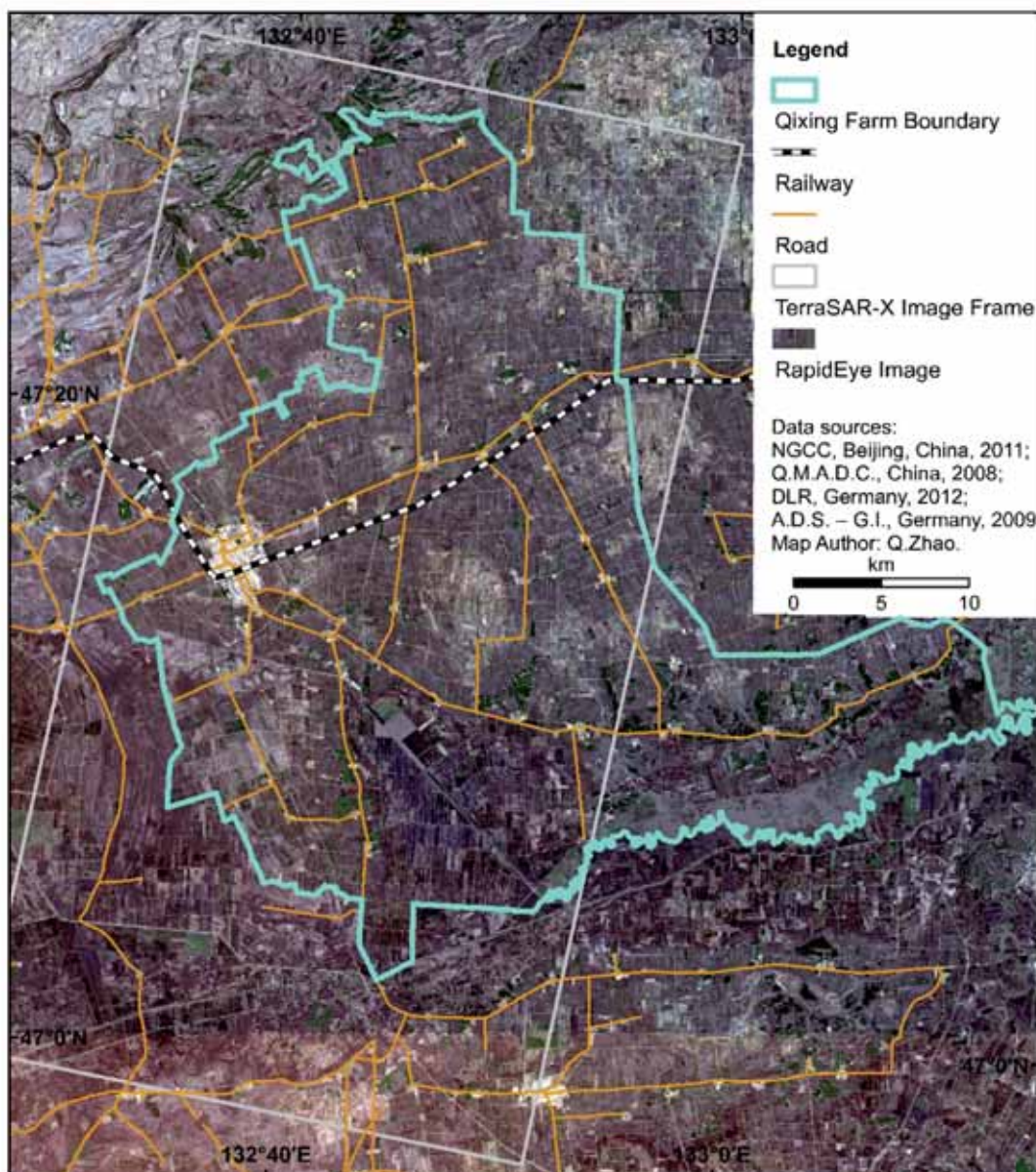


Fig. 5: Georeferenced multi-source data for the study area of Qixing Farm.

Although many studies (SOWMYA & TRINDER 2000, SOHN & DOWMAN 2007, REINARTZ et al. 2009) have attempted to extract geometric features, e.g. GCPs, automatically from satellite images, there is a lack of reports on automatic methods for georeferencing multi-source data. Automatic feature extraction methods have limited applicability due to their complex parameterization and strict condition requirements (COBB et al. 1998). Moreover, automatic methods for integrating GIS data and satellite imagery are rare.

The strategy proposed in this study showed that for each dataset, different GCPs were required due to the diverse characteristics of the multi-source data. Manual procedure meets this requirement and ensures the spatial accuracy. Although the high resolution TSX imagery supplies a sufficient number of GCPs, the selection of the GCPs and their corresponding tie points is never straightforward. There is still a need to establish the criteria for selecting reference points systematically. Another drawback of this method is its inefficiency in processing a large number of datasets. However, the proposed method still is especially valuable for data-poor environments lacking reference data.

## 6 Conclusions

This study provides an applicable and cost-effective approach for georeferencing multi-source data with different characteristics and non-systematic spatial inconsistencies. It is an especially beneficial technique for large study sites with limited accessibility and reference maps. The results demonstrated the feasibility of using TSX imagery to accurately georeference multi-source datasets without in-situ GCP data collection. By using the mean of five TSX images and the mean filter, a speckle-free reference image was generated. This proved to be critical for locating sufficient GCPs successfully. The PEs of the check points were less than 0.2 pixel for the 30 m resolution images (HJ and LS), approximately 2.5 pixels for the FS-2 images, and 1.3 pixels for the RE images. The overall errors were nearly less than 10 m for all four types of images. The discrepancies among each pair of the TSX and GIS

data were only assessed visually, which demonstrates a need for further study.

## Acknowledgements

This research was funded by the Natural Science Foundation of China (NSFC, project No. 31071859), the International Bureau of the German Federal Ministry of Education and Research (BMBF, project No. 01DO12013), and the German Research Foundation (DFG, project No. BA 2062/8-1). The TerraSAR-X images were provided by the Airbus Defence and Space – Geo-Intelligence. The GIS data layer of the Qixing Farm field boundary was provided by the Qixing Modern Agriculture Development Center in Heilongjiang, China. The 1:250,000 scale topographic dataset with multiple layers for the study area was provided by the National Geomatics Center of China (NGCC) (<http://ngcc.sbsm.gov.cn/>). The Huanjing satellite images were acquired from the China Centre for Resources Satellite Data and Application (CCRSDA) (<http://www.cresda.com/n16/index.html>). The Landsat 5 TM images were downloaded from the website of the Earth Resources Observation and Science (EROS) Center of U.S. Geological Survey (USGS) (<http://eros.usgs.gov/>). The FORMOSAT-2 images were obtained from the National Space Organization (NSPO) of Taiwan. The RapidEye satellite images were kindly provided by the RE Science Archive (RESA), German Aerospace Center (Deutsches Zentrum für Luft- und Raumfahrt, DLR). The leading author would also like to acknowledge the support of the China Scholarship Council (Nov. 2010 – Oct. 2014), Beijing, China.

## References

- AGER, T.P. & BRESNAHAN, P.C., 2009: Geometric precision in space radar imaging: results from TerraSAR-X. – ASPRS Annual Conference, Baltimore, MD, USA.
- BADURSKA, M., 2011: Orthorectification and Geometric Verification of High Resolution TerraSAR-X Images. – *Geomatics and Environmental Engineering* **5** (3): 13–25.

- BARETH, G. & YU, Z., 2004: Verfügbarkeit von digitalen Geodaten in China. – *Petermanns Geographische Mitteilungen* **148** (5): 78–85 (written in German with English abstract).
- BARETH, G., 2009: GIS- and RS-based spatial decision support: structure of a spatial environmental information system (SEIS). – *International Journal of Digital Earth* **2** (2): 134–154.
- CHEN, C.C., KNOBLOCK, C.A. & SHAHABI, C., 2006: Automatically conflating road vector data with orthoimagery. – *GeoInformatica* **10** (4): 495–530.
- CHOI, K. & LEE, I., 2012: A sequential aerial triangulation algorithm for real-time georeferencing of image sequences acquired by an airborne multi-sensor system. – *Remote Sensing* **5** (1): 57–82.
- COBB, M.A., CHUNG, M.J., FOLEY, H., PETRY, F.E. & SHAW, K.B., 1998: A Rule-based Approach for the Conflation of Attributed Vector Data. – *GeoInformatica* **2** (1): 7–35.
- CONGALTON, R.G. & GREEN, K., 2008: Assessing the accuracy of remotely sensed data: principles and practices. – 183 p., CRC press, Boca Raton, FL, USA.
- CURLANDER, J.C. & McDONOUGH, R.N., 1991: Synthetic aperture radar: systems and signal processing. – 1<sup>st</sup> edition, 672 p., Wiley, New York, NY, USA.
- DAI, X. & KHORRAM, S., 1998: The effects of image misregistration on the accuracy of remotely sensed change detection. – *IEEE Transactions on Geoscience and Remote Sensing* **36** (5): 1566–1577.
- DOUGENIK, J.A., CHRISMAN, N.R. & NIEMEYER, D.R., 1985: An algorithm to construct continuous area cartograms. – *The Professional Geographer* **37**: 75–81.
- FRITZ, T. & EINEDER, M., 2013 (eds.): TerraSAR-X Ground Segment. – Basic Product Specification Document. Issue 1.9, Doc.: TX-GS-DD-3302, DLR. [https://tandemx-science.dlr.de/pdfs/TX-GS-DD-3302\\_Basic-Products-Specification-Document\\_V1.9.pdf](https://tandemx-science.dlr.de/pdfs/TX-GS-DD-3302_Basic-Products-Specification-Document_V1.9.pdf) (18.4.2014).
- GILLMAN, D.W., 1985: Triangulations for rubber-sheeting. – 7<sup>th</sup> International Symposium on Auto-Carto: 191–199, Washington D.C., USA.
- GÓMEZ-CANDÓN, D., LÓPEZ-GRANADOS, F., CABALLERO-NOVELLA, J.J., PEÑA-BARRAGÁN, J.M. & GARCÍA-TORRES, L., 2012: Understanding the errors in input prescription maps based on high spatial resolution remote sensing images. – *Precision Agriculture* **13** (5): 581–593.
- KOPPE, W., KIEFL, N., HENNIG, S. & JANOTH, J., 2010: Validation of Pixel Location Accuracy of Orthorectified TerraSAR-X Products. – 8<sup>th</sup> European Conference on Synthetic Aperture Radar (EU-SAR), Aachen.
- LI, D., 2010: Remotely sensed images and GIS data fusion for automatic change detection. – *International Journal of Image and Data Fusion* **1** (1): 99–108.
- LIU, T. & ZHAO, Y., 1996: Ecological benefit analysis and estimation of the forest shelter in the Nongken area, Sanjiang Plain. – *Forest Science and Technology* **5**: 12–14 (written in Chinese).
- MITTERMAYER, J. & RUNGE, H., 2003: Conceptual studies for exploiting the TerraSAR-X dual receive antenna. – IGARSS: 2140–2142, Toulouse, France.
- NONAKA, T., ISHIZUKA, Y., YAMANE, N., SHIBAYAMA, T., TAKAGISHI, S. & SASAGAWA, T., 2008: Evaluation of the geometric accuracy of TerraSAR-X. – *The International Archives of the Photogrammetry, Remote Sensing and Spatial Information Sciences XXXVII*, Beijing, China.
- OZDOGAN, M. & WOODCOCK, C.E., 2006: Resolution dependent errors in remote sensing of cultivated areas. – *Remote Sensing of Environment* **103** (2): 203–217.
- REINARTZ, P., MÜLLER, R., SURI, S., SCHNEIDER, M., SCHWIND, P. & BAMLER, R., 2009: Using geometric accuracy of TerraSAR-X data for improvement of direct sensor orientation and ortho-rectification of optical satellite data. – *IEEE International Geoscience & Remote Sensing, IGARSS 5*: V-44–V-47, Cape Town, South Africa.
- REINARTZ, P., MULLER, R., SCHWIND, P., SURI, S. & BAMLER, R., 2011: Orthorectification of VHR optical satellite data exploiting the geometric accuracy of TerraSAR-X data. – *ISPRS Journal of Photogrammetry and Remote Sensing* **66** (1): 124–132.
- RODRÍGUEZ, E., MORRIS, C.S. & BELZ, J.E., 2006: A Global Assessment of the SRTM Performance. – *Photogrammetric Engineering & Remote Sensing* **72** (3): 249–260.
- SCHNEIDER, M., MÜLLER, R., KRAUSS, T., REINARTZ, P., HÖRSCH, B. & SCHMUCK, S., 2009: Urban Atlas – DLR Processing Chain for Orthorectification of Prism and AVNIR-2 Images and TerraSAR-X as possible GCP Source. – 3<sup>rd</sup> ALOS PI Symposium: 1–6, Kona, HI, USA. [http://www.asf.alaska.edu/content/pi\\_symp/Schneider\\_M.\\_urban-paper.pdf](http://www.asf.alaska.edu/content/pi_symp/Schneider_M._urban-paper.pdf) (20.4.2014).
- SOHN, G. & DOWMAN, I., 2007: Data fusion of high-resolution satellite imagery and LiDAR data for automatic building extraction. – *ISPRS Journal of Photogrammetry and Remote Sensing* **62** (1): 43–63.
- SOLBERG, A.H.S., TAXT, T. & JAIN, A.K., 1996: A Markov random field model for classification of multisource satellite imagery. – *IEEE Transactions*

- tions on *Geoscience and Remote Sensing* **34** (1): 100–113.
- SONG, W., KELLER, J.M., HAITHCOAT, T.L. & DAVIS, C.H., 2009: Automated Geospatial Conflation of Vector Road Maps to High Resolution Imagery. – *IEEE Transactions on Image Processing* **18** (2): 388–400.
- SOWMYA, A. & TRINDER, J., 2000: Modelling and representation issues in automated feature extraction from aerial and satellite images. – *ISPRS Journal of Photogrammetry and Remote Sensing* **55** (1): 34–47.
- SUN, S., 2013a: An optimized rubber-sheet algorithm for continuous area cartograms. – *Professional Geographer* **65** (1): 16–30.
- SUN, S., 2013b: A fast, free-form rubber-sheet algorithm for contiguous area cartograms. – *International Journal of Geographical Information Science* **27** (3): 567–593.
- TOBLER, W., 2004: Thirty five years of computer cartograms. – *Annals of the Association of American Geographers* **94** (1): 58–73.
- USERY, E.L., FINN, M.P. & STARBUCK, M., 2009: Data layer integration for the national maps of the United States. – *Cartographic Perspectives* **62**: 28–41.
- VON GÖSSELN, G.V. & SESTER, M., 2004: Integration of geoscientific data sets and the German digital map using a matching approach. – XX<sup>th</sup> Congress of the International Society for Photogrammetry and Remote Sensing, Commission IV, XXXV-B4: 1247, Istanbul, Turkey.
- WALDHOFF, G., CURDT, C., HOFFMEISTER, D. & BARETH, G., 2012: Analysis of multitemporal and multisensor remote sensing data for crop rotation mapping. – XXII<sup>th</sup> Congress of the International Society for Photogrammetry and Remote Sensing, Melbourne, Australia.
- WALTER, V. & FRITSCH, D., 1999: Matching spatial datasets: A statistical approach. – *International Journal of Geographical Information Science* **13** (5): 445–473.
- WANG, Z., ZHANG, B., ZHANG, S., LI, X., LIU, D., SONG, K., LI, J., LI, F. & DUAN, H., 2006: Changes of land use and of ecosystem service values in Sanjiang Plain, northeast China. – *Environmental Monitoring and Assessment* **112** (1–3): 69–91.
- WEBER, K.T., THÉAU, J. & SERR, K., 2008: Effect of coregistration error on patchy target detection using high-resolution imagery. – *Remote Sensing of Environment* **112** (3): 845–850.
- WEIS, M., MÜLLER, S., LIEDTKE, C.-E. & PAHL, M., 2005: A framework for GIS and imagery data fusion in support of cartographic updating. – *Information Fusion* **6** (4): 311–317.
- WU, X., CARCERONI, R., FANG, H. & KIRMSE, A., 2007: Automatic alignment of large-scale aerial rasters to road-maps. – 15<sup>th</sup> annual ACM international symposium on Advances in geographic information systems, Seattle, WA, USA.
- ZHANG, J., 2010: Multi-source remote sensing data fusion: status and trends. – *International Journal of Image and Data Fusion* **1** (1): 5–24.
- ZHANG, W., 2012: Personal communication, Qixing Farm, June 2012.

## Addresses of the Authors:

M.SC. QUANYING ZHAO, Dipl.-Geogr. CHRISTOPH HÜTT, Dr. VICTORIA I.S. LENZ-WIEDEMANN & Prof. Dr. GEORG BARETH, International Center for Agro-Informatics and Sustainable Development (ICASD) ([www.icasd.org](http://www.icasd.org)), Institute of Geography, GIS & RS Group, University of Cologne, D-50923 Köln, Tel.: +49-221-470-1951, e-mail: [zhaoquanying@gmail.com](mailto:zhaoquanying@gmail.com), {christoph.huett}{victoria.lenz}{g.bareth}@uni-koeln.de

Prof. Dr. YUXIN MIAO, ICASD, College of Resources and Environmental Sciences, China Agricultural University, Beijing China, 100193 Beijing, Tel.: +86-10-6273-2865, e-mail: [ymiao@cau.edu.cn](mailto:ymiao@cau.edu.cn)

Prof. Dr. FEI YUAN, ICASD, Department of Geography, Minnesota State University, Minnesota, MN 56001, USA, Tel.: +1-507-389-2376, e-mail: [fei.yuan@mnsu.edu](mailto:fei.yuan@mnsu.edu)

Prof. Dr. FUSUO ZHANG, College of Resources and Environmental Sciences, China Agricultural University, Beijing China, 100193 Beijing, Tel.: +86-10-6273-2499, e-mail: [zhangfs@cau.edu.cn](mailto:zhangfs@cau.edu.cn)

Manuskript eingereicht: August 2014

Angenommen: Dezember 2014



## Berichte von Veranstaltungen

### Symposium der ISPRS Commission III, 5. – 7. September 2014, Zürich, Schweiz

Das Midterm Symposium *Photogrammetric Computer Vision – PCV 2014* der ISPRS Technical Commission III fand vom 5. – 7. September 2014 an der Eidgenössischen Technischen Hochschule (ETH) in Zürich, Schweiz, statt. Die Hauptverantwortlichen für die Veranstaltung waren KONRAD SCHINDLER (ETH Zürich) und NICOLAS PAPANODITIS (IGN France).

Insgesamt umfasste das Symposium zwei Keynote-Vorträge, acht thematisch unterschiedlich ausgerichtete Oral Sessions, zwei Poster Sessions und eine Special Session. Die individuellen Blöcke fanden sequentiell statt, so dass alle Teilnehmer am gesamten Programm teilnehmen konnten.

Für die Keynote-Vorträge waren zwei namhafte Gastredner eingeladen: ANDREW DAVISON (Imperial College London) erläuterte in seinem interessanten Vortrag zum Thema *Towards real-time, dense tracking, reconstruction and scene understanding* die aktuellen

Möglichkeiten und Herausforderungen im Bereich der Robotik für die räumliche Wahrnehmung der lokalen Umgebung und zur autonomen Navigation sowie zur Ableitung einer semantischen Beschreibung von 3D-Szenen. Ferner referierte MICHAEL GOESELE (TU Darmstadt) zum Thema *Photometric reconstruction in the wild* und stellte dabei unterschiedliche Ansätze vor, mit denen aus Bildern möglichst viel Information bezüglich der geometrischen und räumlichen Anordnung von Objekten sowie deren Reflektanzeigenschaften abgeleitet werden kann.

Im Rahmen der Oral Sessions wurden insgesamt 27 Beiträge zu den Themen *Stereo and Multiview, Buildings, Point Clouds, Pose Estimation, Scene Interpretation, Calibration and Registration, Graphics and Texture* und *Performance Evaluation* vorgestellt. Die beiden Poster Sessions mit zahlreichen interaktiven Präsentationen deckten ebenfalls diese Themengebiete ab, und da die Poster strategisch günstig in der Nähe des Kaffeebuffets aufgehängt waren, nutzten viele Teilnehmer die Zeit zum wissenschaftlichen Austausch und

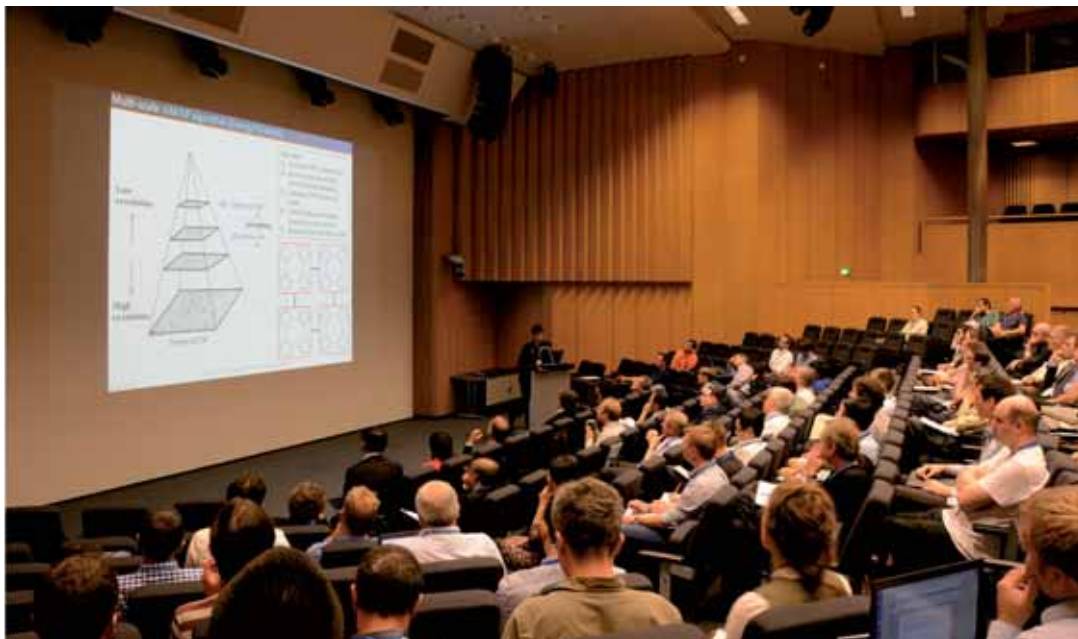


Abb. 1: Interessierte Zuhörerschaft während einer Oral Session.

für intensive Diskussionen mit den jeweiligen Autoren. Die Special Session bezog sich auf eine *Tracking and Imaging Challenge*, zu welcher sechs Beiträge in Form einer Kurzpräsentation vorgestellt wurden.

Für die Einreichung von Beiträgen gab es wie gewohnt wieder unterschiedliche Möglichkeiten. Zum einen konnten vollständige Beiträge mit einem Umfang von maximal acht Seiten für eine anonyme Begutachtung eingereicht werden, zum anderen gab es die Möglichkeit, Zusammenfassungen von Beiträgen für eine anonyme Begutachtung einzureichen. Von insgesamt 48 eingereichten vollständigen Beiträgen wurden 27 (56%) angenommen und in Form von Vorträgen präsentiert. Diese Beiträge sind in den *ISPRS Annals of the Photogrammetry, Remote Sensing and Spatial Information Sciences* erschienen. Für 17 weitere Beiträge wurde zusammen mit 62 Beiträgen, welche basierend auf einer Zusammenfassung begutachtet wurden, die Eignung für die *International Archives of the Photogrammetry, Remote Sensing and Spatial Information Sciences* geprüft. Von diesen Beiträgen wurden insgesamt 56 angenommen und als Poster präsentiert. Alle angenommenen Beiträge sind auch auf der Internetseite der ISPRS verfügbar.

Von allen eingereichten Beiträgen wurden drei mit Preisen ausgezeichnet. Der *PCV 2014 Best Paper Prize* wurde an PRZEMYSŁAW POLEWSKI, WEI YAO, PETER KRZYSZEK, MARCO

HEURICH und UWE STILLA für ihren Beitrag zum Thema *Detection of fallen trees in ALS point clouds by learning the Normalized Cut similarity function from simulated samples* verliehen. Zusätzlich wurden die Beiträge von DEVIS TUIA, NICOLAS COURTY und RÉMI FLAMARY zum Thema *A group-lasso active set strategy for multiclass hyperspectral image classification* und von MARTIN WEINMANN, BORIS JUTZI und CLÉMENT MALLET zum Thema *Semantic 3D scene interpretation: a framework combining optimal neighborhood size selection with relevant features* mit dem *PCV 2014 Best Paper Honourable Mention* ausgezeichnet.

Zusammenfassend ist festzuhalten, dass die Veranstaltung hervorragend organisiert war, wofür den Verantwortlichen und Helfern herzlich zu danken ist. Besonders hervorzuheben sind das ausgezeichnete fachliche Niveau der Veranstaltung, die beiden interessanten Keynote-Vorträge und ein gelungener technischer Ablauf, aber auch die bereits im Vorfeld termingerecht durchgeführte Koordinierung des Review-Prozesses sowie die Bereitstellung von Informationen auf der Internetseite. Ebenso wird das ansprechende Ambiente während der Social Events an der ETH Zürich und im Seebad Enge vielen Teilnehmern sicher noch lange in guter Erinnerung bleiben.

ROSMARIE BLOMLEY und  
MARTIN WEINMANN, Karlsruhe



Abb. 2: Eindrücke von der Abendveranstaltung im Seebad Enge.

### **14<sup>th</sup> RACURS Photogrammetric Conference, 19. – 23. October 2014, Hainan, China**

The 14<sup>th</sup> Racurs Photogrammetric Conference took place from October 19 to 23, 2014, in Hainan, China. This well respected conference is internationally very unique, since it bridges the technical developments in photogrammetry, remote sensing and geographic information systems between the Western World and the developments in the Russian Federation with its long and quite different tradition. Excellent simultaneous translation between Russian and English participants is provided, and this is the basis for an excellent interchange of ideas between the West and Russia. This year Chinese participants with English speaking knowledge were also invited to the meeting.

On Monday, October 20, the conference was opened. Dr. VICTOR ADROV, CEO and owner of Racurs, opened the conference which in the last 14 years gained significant international importance. He reviewed the Racurs history. XU MINGCE, the Racurs representative in China, CEO of the company “Smart Spatio”, joined with a welcome, mentioning that Racurs photogrammetric hard and software system “Photomod” is licensed to 30 sites in China as an English language version. Also, CHEN JUN, President of ISPRS, joined with a welcome on behalf of ISPRS.

GOTTFRIED KONECNY followed with a keynote on the *Current Status of Mapping in the World*. While for the last UN Secretariat Survey carried out in 1986 the world coverage of 1:25,000 maps was only 33% and of 1:50,000 only 67% with a complete coverage of the globe at the scale 1:250,000, recent UN-ISPRS surveys showed that a global coverage of 1:50,000 is now available, even though 80 of the 193 UN member countries do not wish to talk about it. CHEN JUN reported in another keynote on the Chinese global land cover project at 30 metre ground sample distance. The dataset on land cover for the years 2000 and 2010 has been verified with other satellite images and existing land cover data for China, Europe and some parts of Africa. It has been donated by the Chinese Government to the Secretary General BAN KI MOON of the United

Nations for use by UN Member countries. It will also be available through UN GEO in Geneva.

Progress in the Russian Federation was reported by ANDREY ZELEYAKOV (KB Panorama), who described the Russian governmental programs for conversion of reference frames, Open Street Map for updates, agrarian GIS, and 3D efforts. ARMIN GRUEN, ETH Zürich, who spent the last year at the University of Singapore for a “Smart City” Project, reported about modeling the city in 3D. As aerial mapping imagery is classified in Singapore and not available to civilians, he used UAVs (quadrocopters) to get high resolution urban information. Altogether 900 images were used. The software Apero was used for cm accuracy, an accuracy, which could not be reached by classical programs, such as Leica LPS. UAV images were combined with terrestrial laser scan information. In a second paper KONECNY discussed the *Situation of geographic base data modeling in different parts of the world*. Most countries only have CAD type digital map data, and only few have object oriented data models, which are needed if topographic and cadastral data are to be combined in 2D, since the cadastre needs frequent updates of objects. Whenever 3D data are envisioned for updates, they also need to focus on objects. A solution is CityGML, which has become an OGC standard. Thus, CityGML becomes a link between GIS and Building Information Models (BIM).

MATHIAS LEMMENS of Delft Technical University spoke on the developments in Lidar. In 1998, Lidar was available for a density of 1 point per 25 square metres. Now 10 points per square metre can be reached leading to the necessity to process point clouds. Terrasolid from Finland has proven to be a leading software. Point cloud processing can also be applied to aerial imagery by dense image matching up to 100 points per square metre. GRUEN continued with a paper on the application of UAVs for the survey of several Zhukov towers built of metal, in Moscow (150 m high) and Buchara, Uzbekistan. This was supplemented by MIKHAILOV from MIIGAiK with another presentation on 3D modelling of Shukhov Tower by a stereo-photogrammetric survey. The last presentation was given by ALEXANDER

CHEKURIN, Racurs, demonstrating a project from Ekaterinburg, where a 3D city model was created from triplet Pleiades satellite imagery (50 cm GSD), supplemented by aerial photos (3 cm – 20 cm GSD) and UAV images (5 cm GSD).

On Tuesday, October 21, VALERY ZAICHKO, head of the Department of the Russian Federation Space Agency, opened the session on satellite systems, which comprised numerous presentations about sensors, data, software and standards of spaceborne remote sensing programs. In particular, reports were given on the Russian Resurs P satellite program, the Chinese CBERS mission aiming at a total of ca. 100 satellites carrying pan, multispectral, hyperspectral and SAR sensors, the Rapid Eye-like satellite constellation planned by Kazakhstan (KazEOSat), the Korean Kompsat constellation, the WorldView-1, -2, -3 satellites, as well as SPOT and RapidEye products and applications.

On Wednesday, October 22, Master Classes for the use of Photomod software were arranged, as well as discussion panels.

The Racurs Conference in Hainan was an exceptional experience: an excellent conference facility, The Meridian Hotel at Shimei Bay with beautiful rooms, wonderful access to the beach alongside the South China Sea, excellent food and many entertainment facilities for the participants, which in such surroundings became a family reunion of professionals in our discipline, and moreover with an excellent technical program, which is difficult to find elsewhere.

GOTTFRIED KONECNY, Hannover

### **Symposium der ISPRS Commission I, 17. – 20. November 2014, Denver, USA**

Das ISPRS-Commission I Symposium fand dieses Jahr gemeinsam mit dem Symposium der International Association of Geodesy (IAG) Commission IV und dem 19. Pecora Memorial Remote Sensing Symposium statt. Die Konferenz wurde vom 17. bis 20. November 2014 in Denver, USA, abgehalten und stand unter dem Motto *Sustaining Land Im-*

*aging: UAS to Satellites*. Organisiert wurde die Veranstaltung von ISPRS Technical Commission I Präsident CHARLES TOTH (Columbus, OH, USA) und Vize-Präsident BORIS JUTZI (Karlsruhe).

Zum gemeinsamen Symposium wurden 157 Vorträge und 34 Posterbeiträge eingeladen. Die Vorträge gliederten sich in 35 technische Sitzungen, von denen teilweise bis zu sechs parallel abgehalten wurden. Das Motto und die Themen des gemeinsamen Symposiums sind sehr allgemein gehalten, so dass mit den Beiträgen ein recht breites Spektrum an Sensoren, Auswertungen und Anwendungsmöglichkeiten abgedeckt wurde. Begleitet wurde das Symposium von einer Firmenausstellung. Insgesamt nahmen 450 Teilnehmer am gemeinsamen Symposium teil.

In der Keynote ging BERRIEN MOORE von der Universität von Oklahoma auf die erfolgreiche Geschichte des Landsat-Programms ein. Er verwies auf die langjährigen kontinuierlichen Beobachtungsreihen seit Start des Programms im Jahre 1972, aus denen sich breit gefächerte Anwendungsmöglichkeiten entwickelt haben. Durch den freien Zugang zu den Daten ab 2008 stieg die Verbreitung der Landsat-Bilder exponentiell. Er kritisierte dann sehr deutlich, dass durch Budgetkürzungen in den USA die nachhaltige Fortführung des Landsat-Programms gefährdet ist. Problematisch erscheint auch, dass eine politisch geforderte Kommerzialisierung des Landsat-Programms und der bisher sehr erfolgreiche freie Zugang zu den Daten im Widerspruch stehen.

Im Zuge der gesamten Veranstaltung wurden die durch den Titel gesetzten Schwerpunkte Unmanned Aircraft Systems (UAS) und das Landsat-Programm deutlich sichtbar: Bei den UAS Beiträgen wurden die Themen Kamera-Kalibrierung und Auswerteverfahren von schräg aufgenommenen Luftbildern öfters adressiert. Schwerpunkte lagen auch in der Erschließung von Anwendungsgebieten, die sich aus derart hochaufgelösten Bilddaten ergeben, und der Verbesserung der Genauigkeiten der abgeleiteten Produkte. Die eingeladenen Vorträge fokussierten beispielsweise auf die Erfassung von Wetterparametern mit Hilfe von UAS in der Nähe von Tornados oder anderen Unwettern. Die Beiträge zu Landsat

sind vor allem durch die Landsat 8 Mission seit dem Jahr 2013 geprägt. Diskutiert wurde in diesem Zusammenhang auch eine Integration von Landsat und Sentinel 2, um die Zeitreihen gegenseitig zu vervollständigen und um die Wiederholrate zu steigern. Ein aktuell auffälliges Thema bei den Satellitendaten ist der SkySat-1 Satellit der Firma Skybox Images, der seit 2013 hochauflösende Bilder und erstmals sogar ein HD Video aus dem All mit ca. 1 Meter Bodenauflösung liefert. Hierzu wurden Untersuchungen zu den geometrischen und radiometrischen Eigenschaften der Daten sowie die Möglichkeiten zur DSM Generierung gezeigt.

Am letzten Tag der Veranstaltung stellte in einer weiteren Keynote REBBECA MOORE von Google die Prozessierungs- und Datenhaltungsumgebung von Google für Satellitendaten vor. Nutzer können hier Zugriff auf die kompletten Landsat-Zeitreihen erhalten und können Weiterverarbeitungen dieser Bilddaten mit selbst geschriebenen Programmen durchführen. Sie zeigte Beispiele, wie sie selbst anhand der Bilddaten die flächenhafte

Abholzung von Redwoods in Kalifornien stoppen konnte.

Ein weiteres Highlight der Veranstaltung war die Vergabe des Pecora Preises. WILLIAM T. PECORA war Direktor des USGS (United States Geological Survey) von 1965 bis 1971, und ihm zu Ehren wird jährlich das Pecora Memorial Remote Sensing Symposium abgehalten. Der nach ihm benannte Preis ging dieses Jahr an das Landsat 8 Team und an CHRISTOPHER JUSTICE von der Universität in Maryland. Das Pecora Memorial Symposium wurde in den 1970er Jahren von der USGS und NASA als Austauschforum für Fernerkundung gegründet.

Weiterhin wurden auf dem gemeinsamen Symposium insgesamt drei ISPRS Benchmark-Datensätze vorgestellt, einer für DEM Prozessierungsalgorithmen und der Ableitung von Qualitätsparametern (Arbeitsgruppen WG I/4), einer für dichtes Bild-Matching in Kooperation mit dem EuroSDR und – neu hinzugekommen – einer für Multi-Plattform Sensoren (Arbeitsgruppe ICWG I/Vb). Der zuletzt genannte Benchmark-Datensatz umfasst



Abb. 1: Auszeichnung des Landsat 8 Teams mit dem Pecora Preis.

schräg aufgenommene Luftbilder, mit UAS erfasste Bilder, terrestrisch erfasste Bilder und Laserscanner-Daten, luftgestützte Laserscanner-Daten sowie hochgenaue Passpunkte in der Umgebung von Dortmund mit dem Ziel der DSM Generierung.

Den Organisatoren sei schließlich für die sehr gute Vorbereitung und Durchführung des intensiven und hochinteressanten Symposiums gedankt. Die publizierten Beiträge sind in den bekannten Veröffentlichungsorganen der ISPRS online abrufbar.

FRANZ KURZ, Oberpfaffenhofen

### Nachruf auf GERHARD NEUKUM (1944 – 2014)



Am 21.9.2014 verstarb im Alter von 70 Jahren Prof. Dr. rer. nat. habil. GERHARD NEUKUM, weltweit anerkannter Planetenforscher und treibende Kraft hinter der ersten europäischen Planetenmission Mars Express, die mit Hilfe der von ihm und seinem Team am Deutschen Zentrum für Luft- und Raumfahrt (DLR) entwickelten HRSC (High Resolution Stereo Camera) seit über 10 Jahren hoch aufgelöste digitale Bilder unseres Nachbarplaneten aufnimmt. NEUKUM hat sich aber nicht nur für die Mission selber stark gemacht, sondern sich auch von vornherein konsequent darum gekümmert, dass die Bilder zu Digitalen Geländemodellen und Orthophotomosaiken und damit zu für die Planetologie verwertbaren Ergebnissen weiterverarbeitet werden konnten. Auf dem Weg dorthin hat er durch die Entwicklung der HRSC den Bereich der photogrammetrischen Luftbildkameras revolutioniert, indem er nachgewiesen hat, dass der Einsatz von Mehrzeilenkameras aus Luft und Weltraum operationell möglich ist. Mit dieser Leistung hat NEUKUM seine glänzende Karriere sowohl in der Planetenforschung als auch in der Photogrammetrie gekrönt.

NEUKUM wurde am 23.2.1944 in Johnsdorf im Sudetenland geboren. Nach dem Studium der Physik promovierte er 1974 über Mondgestein, das von den Apolloastronauten zur Erde zurück gebracht worden war. 1983 habilitierte er sich an der Ludwig Maximilian Universität in München mit einem Thema aus der Planetologie. Seit 1989 war er dort als apl. Professor für Geophysik und Planetologie tätig. 1997 wurde NEUKUM als Professor an das Institut für Geologische Wissenschaften der Freien Universität Berlin berufen, an dem er bis zu seiner Emeritierung 2013 tätig war.

Bereits kurz nach seiner Promotion ging NEUKUM zum DLR nach Oberpfaffenhofen und leitete dort von 1981 – 1991 die Abteilung für Planetare Erkundung am Institut für Optoelektronik. 1993 – 2002 war er Direktor des heutigen DLR Instituts für Planetenforschung in Berlin-Adlershof.

Mit seinen bahnbrechenden Arbeiten zur Altersbestimmung planetarer Oberflächen durch Bestimmung der Häufigkeitsverteilungen von Einschlagskratern wurde NEUKUM zum Pionier der deutschen Planetenforschung. Die von ihm entwickelten Methoden werden noch heute weltweit mit großem Erfolg eingesetzt, die Ergebnisse tragen wesentlich zu unserem Verständnis der Entwicklung fester Körper des Sonnensystems bei. Neben den Arbeiten zu Mars Express hat NEUKUM an einer Reihe weiterer Weltraummissionen an entscheidender Stelle mitgewirkt, genannt seien hier Galileo, Cassini, Rosetta und Dawn.

Die deutsche Photogrammetrie und Fernerkundung verliert mit GERHARD NEUKUM einen herausragenden Wissenschaftler, der immer von den sich mit photogrammetrischen Mitteln bietenden Möglichkeiten überzeugt war,

Planetenoberflächen vollständig, detailreich, hoch genau, und zuverlässig kartieren zu können. Mit der ihm eigenen Entschiedenheit und einem bemerkenswertem Blick für das Wesentliche hat er sich stets für Photogrammetrie und Fernerkundung eingesetzt und die Spezialisten auf dem Gebiet vehement unterstützt – sein Enthusiasmus, sein Charisma und sein Durchsetzungswille sind legendär und werden

es bleiben. Die photogrammetrische Gemeinschaft ist ihm dafür zu größtem Dank verpflichtet und wird ihm stets ein ehrendes Andenken bewahren. Wir trauern zusammen mit seiner Frau und seiner Familie um einen großen Wissenschaftler und Menschen.

CHRISTIAN HEIPKE, Hannover  
und RALF JAUMANN, Berlin

## Veranstaltungskalender

### 2015

23.–27. März: **ESA FRINGE Workshop in Frascati**, Italien. [seom.esa.int/fringe2015](http://seom.esa.int/fringe2015)

25.–27. März: **PIA15 + HRIGI: Joint Conference of Photogrammetric Image Analysis and High Resolution Earth Imaging for Geospatial Information 2015** in München. [pf.bgu.tum.de/isprs/pia15/index.html](http://pf.bgu.tum.de/isprs/pia15/index.html)

30. März – 1. April: **JURSE – IEEE Joint Urban Remote Sensing Event 2015** in Lausanne, Schweiz. [jurse2015.org](http://jurse2015.org)

11.–15. Mai: **ISRSE36 – International Symposium on Remote Sensing of the Earth in Berlin**. [isrse36.org](http://isrse36.org)

7.–12. Juni: **CVPR 2015 – Conference on Computer Vision and Pattern Recognition 2015** in Boston, USA. [pamitc.org/cvpr15/](http://pamitc.org/cvpr15/)

11. Juni: **ISPRS-CVPR joint workshops: Looking from above: when Earth observation meets vision (EarthVision) und Multi-Sensor Fusion for Outdoor Dynamic Scene Understanding** in Boston, USA. [pamitc.org/cvpr15/](http://pamitc.org/cvpr15/)

5.–11. Juli: **Innsbruck Summer School on Alpine Research 2015: Close Range Sensing Techniques in Alpine Terrain** in Obergurgl, Österreich. [uibk.ac.at/geographie/summerschool](http://uibk.ac.at/geographie/summerschool)

26.–31. Juli: **IGARSS 2015 – International Geoscience and Remote Sensing Symposium 2015** in Mailand, Italien. [igarss2015.org](http://igarss2015.org)

23.–28. August: **ICC – International Cartographic Conference** in Rio de Janeiro, Brasilien. [icc2015.org](http://icc2015.org)

30. August – 2. September: **UAV-g: Unmanned Aerial Vehicles in Geomatics** in Toronto, Kanada. [uav-g2015.org](http://uav-g2015.org)

31. August – 5. September: **CIPA 2015: 25<sup>th</sup> CIPA Heritage Documentation Symposium** in Taipeh, Taiwan. [cipa2015.org](http://cipa2015.org)

6.–11. September: **Photogrammetrische Woche 2015** in Stuttgart. [ifp.uni-stuttgart.de/phowo](http://ifp.uni-stuttgart.de/phowo)

15.–17. September: **INTERGEO** in Stuttgart. [intergeo.de](http://intergeo.de)

21.–24. September: **SPIE Remote Sensing 2015** in Toulouse, Frankreich. [spie.org/remote-sensing-europe.xml](http://spie.org/remote-sensing-europe.xml)

28. September – 3. Oktober: **ISPRS Geospatial Week 2015** in La Grande Motte, Frankreich. [isprs-geospatialweek2015.org](http://isprs-geospatialweek2015.org)

6.–9. Oktober: **GCPR (DAGM): German Conference on Pattern Recognition** in Aachen.

7.–13. Dezember: **ICCV 2015 – International Conference for Computer Vision 2015** in **Santiago, Chile**.

9.–11. Dezember: **MMT 2015: 9<sup>th</sup> International Symposium on Mobile Mapping Technology** in **Sydney, Australien**. [mmt2015.org](http://mmt2015.org)

10.–16. Oktober: **ECCV 2016 – European Conference on Computer Vision 2016** in **Amsterdam, Niederlande**. [eccv2016.org](http://eccv2016.org)

8.–11. November: **ICPR 2016 – International Conference on Pattern Recognition 2016** in **Cancun, Mexiko**.

## 2016

3.–4. Februar: **Oldenburger 3D Tage in Oldenburg**. [jade-hs.de/fachbereiche/bauwesen-und-geoinformation/geoinformation/oldenburger-3d-tage](http://jade-hs.de/fachbereiche/bauwesen-und-geoinformation/geoinformation/oldenburger-3d-tage)

Weitere Konferenzen und Workshops finden sich beispielsweise unter:  
[isprs.org/calendar/Default.aspx](http://isprs.org/calendar/Default.aspx)  
[conferences.visionbib.com](http://conferences.visionbib.com)

## Korporative Mitglieder

### Firmen

AEROWEST GmbH  
 AICON 3D Systems GmbH  
 aphos Leipzig AG  
 ASTEC GEODATA GmbH  
 Bernhard Harzer Verlag GmbH  
 Black Bridge AG  
 Blom Deutschland GmbH  
 Brockmann Consult GmbH  
 bsf swissphoto GmbH  
 Büro Immekus  
 DB Netz AG  
 DELPHI IMM GmbH  
 Deutsches Bergbau-Museum  
 EFTAS Fernerkundung Technologietransfer GmbH  
 ESG Elektroniksystem- und Logistik-GmbH  
 Esri Deutschland GmbH  
 EUROPEAN SPACE IMAGING  
 Eurosense GmbH  
 Exelis Visual Information Solutions GmbH  
 fokus GmbH  
 GAF GmbH  
 GeoCart Herten GmbH  
 Geoinform. & Photogr. Engin. Dr. Kruck & Co. GbR  
 geoplana Ingenieurgesellschaft mbH  
 GEOSYSTEMS GmbH  
 GGS – Büro für Geotechnik, Geoinformatik, Service  
 Hansa Luftbild AG  
 Herbert Wichmann, VDE Verlag GmbH  
 IAGB mbH  
 IGI – Ingenieur-Gesellschaft für Interfaces mbH  
 ILV-Fernerkundungs GmbH  
 Infoterra GmbH  
 INVERS – Industrievermessung & Systeme  
 Leica Geosystems GmbH  
 Linsinger ZT GmbH  
 Luftbilddatenbank Dr. Carls GmbH  
 map/x/tek  
 Messbildstelle GmbH  
 Microsoft Photogrammetry  
 MILAN Geoservice GmbH  
 M.O.S.S. Computer Grafik Systeme GmbH  
 PHOENICS GmbH

PMS – Photo Mess Systeme AG  
 RIEGL Laser Measurement Systems GmbH  
 RWE Power AG, Geobasisdaten/Markscheidewesen  
 technet GmbH  
 Terra-Messflug GmbH  
 topometric GmbH  
 TRIGIS GmbH  
 Trimble Germany GmbH  
 trimetric 3D Service GmbH  
 Z/I Imaging Ltd.

### Behörden

Amt für Geoinformationswesen der Bundeswehr  
 Bayerische Landesanstalt für Wald und Forstwirtschaft  
 Bundesamt für Kartographie und Geodäsie  
 Bundesministerium für Ernährung, Landwirtschaft und Verbraucherschutz  
 Hessisches LA für Bodenmanagement und Geoinformation  
 Innenministerium NRW, Gruppe Vermessungswesen  
 Institut für Umwelt- und Zukunftsforschung  
 LA für Geoinformation und Landentwicklung, BW  
 LA für Vermessung und Geoinformation, Bayern  
 LA für Vermessung und Geoinformation, Schleswig-Holstein  
 LB Geoinformation und Vermessung, Hamburg  
 LB für Küstenschutz, Nationalpark und Meereschutz, SH  
 Landeshauptstadt Düsseldorf, Vermessungs- und Liegenschaftsamt  
 Landesvermessung und Geobasisinformation Niedersachsen  
 Märkischer Kreis, Vermessungs- und Katasteramt  
 Regierungspräsident Tübingen, Abt. 8 Forstdirektion  
 Regionalverband Ruhr  
 Staatsbetrieb Sachsenforst  
 Stadt Köln, Amt für Liegenschaften, Vermessung und Kataster

Stadt Wuppertal, Vermessung, Katasteramt und Geodaten

Thüringer LA für Vermessung und Geoinformation

### Hochschulen

BTU Cottbus, Lehrstuhl für Vermessungskunde

FH Frankfurt a.M., FB 1, Studiengang Geoinformation

FH Mainz, Institut für Raumbezogene Informations- und Messtechnik

HCU HafenCity Universität Hamburg, Geomatik

HfT Stuttgart, Vermessung und Geoinformatik

HS Bochum, FB Vermessung und Geoinformatik

HS Karlsruhe, Fakultät für Geomatik

HTW Dresden, FB Vermessungswesen/Kartographie

Jade Hochschule, Institut für Angewandte Photogrammetrie und Geoinformatik

LUH Hannover, Institut für Kartographie und Geoinformatik

LUH Hannover, Institut für Photogrammetrie und Geoinformation

MLU Halle, FG Geofernerkundung

Ruhr-Uni Bochum, Geographisches Institut

RWTH Aachen, Geodätisches Institut

TU Bergakademie Freiberg, Institut für Markscheidewesen und Geodäsie

TU Berlin, Computer Vision & Remote Sensing

TU Berlin, Institut für Geodäsie und Geoinformationstechnik

TU Braunschweig, Institut für Geodäsie und Photogr.

TU Clausthal, Institut für Geotechnik und Markscheidewesen

TU Darmstadt, Institut für Geodäsie, FG Fernerkundung und Bildanalyse

TU Dresden, Institut für Photogrammetrie und Fernerkundung

TU München, FG Photogrammetrie und Fernerkundung

TU Wien, FG Photogrammetrie und Fernerkundung

Uni Bonn, Institut für Photogrammetrie

Uni Göttingen, Abt. Waldinventur und Fernerkundung

Uni Heidelberg, IWR Interdisziplinäres Zentrum für Wissenschaftliches Rechnen

Uni Kassel, FG Grünlandwissenschaften und Rohstoffe

Uni Kiel, Geographisches Institut

Uni Stuttgart, Institut für Photogrammetrie

Uni Trier, Institut für Umweltfernerkundung und Geoinformatik

Uni Würzburg, Geographisches Institut

Uni zu Köln, Geographisches Institut